Electrochemical Energy Reviews (2021) 4:269–335
https://doi.org/10.1007/s41918-021-00094-7

REVIEW ARTICLE

3D Hierarchical Carbon-Rich Micro-/Nanomaterials for Energy Storage and Catalysis

Zhixiao Xu[1] · Wenjing Deng[1] · Xiaolei Wang[1]

Received: 12 September 2020 / Revised: 12 October 2020 / Accepted: 4 January 2021 / Published online: 13 March 2021

Abstract

Increasing concerns over climate change and energy shortage have driven the development of clean energy devices such as batteries, supercapacitors, fuel cells and solar water splitting in the past decades. And among potential device materials, 3D hierarchical carbon-rich micro-/nanomaterials (3D HCMNs) have come under intense scrutiny because they can prevent the stacking and bundling of low-dimensional building blocks to not only shorten diffusion distances for matter and charge to achieve high-energy-high-power storage but also greatly expose active sites to achieve highly active, durable and efficient catalysis. Based on this, this review will summarize the synthetic strategies and formation mechanisms of 3D HCMNs, including 3D nanocarbons, polymers, COFs/MOFs, templated carbons and derived carbon-based hybrids with a focus on 3D superstructures such as urchins, flowers, hierarchical tubular structures as well as nanoarrays including nanotube, nanofiber and nanosheet arrays. This review will also discuss the application of 3D HCMNs in energy storage and catalysis systems, including batteries, supercapacitors, electrocatalysis and photo(electro)catalysis. Overall, this review will provide a comprehensive overview of the recent progress of 3D HCMNs in terms of preparation strategies, formation mechanisms, structural diversities and electrochemical applications to provide a guideline for the rational design and structure–function exploration of 3D hierarchical nanomaterials from different sources beyond carbon-based species.

Keywords Hierarchical structure · 3D carbon-rich materials · 3D polymer · 3D COF/MOF · Batteries and supercapacitors · Electrocatalysis and photo(electro)catalysis

1 Introduction

Ever-increasing energy demand and drastic climate change call for the replacement of fossil fuels with renewable and green power sources such as rechargeable batteries, supercapacitors, fuel cells and hydrogen energy [1]. The successful application of these electrochemical energy devices depends on the development of cost-effective and highly electroactive materials with unique structural features [2]. In general, materials can be classified into zero-dimensional (0D) quantum dots/nanoparticles, one-dimensional (1D) nanowires/nanorods/nanotubes, two-dimensional (2D) nanosheets/quantum wells and three-dimensional (3D) frameworks in which due to the confinement of electrons inside defined structures, different dimensional structures can exhibit different electrochemical performance in terms of different structural and surface characteristics as well as mass/charge transport pathways [2]. And among different dimensional structures, 3D hierarchical structures constructed by low-dimensional building blocks including 0D, 1D and 2D structures can not only inherit the intrinsic properties of the building elements, but manifest superior performance beyond these basic units, rendering them ideal structures for material fabrication. As a result, numerous 3D materials [3–6] including nanocarbons, Mxenes and transition metal dichalcogenides have been successfully fabricated and investigated for a variety of applications, especially in the fields of electrochemical energy storage and catalysis, illustrating the great potential of these 3D materials.

Carbon as an essential element of life exists in molecular, polymeric and bio-macromolecular forms. And with outstanding physical and chemical properties, carbon-based products such as fullerene, carbon nanotube, graphene and diamond are regarded as next-generation

✉ Xiaolei Wang
xiaolei.wang@ualberta.ca

[1] Department of Chemical and Materials Engineering, University of Alberta, Edmonton, AB T6G 1H9, Canada

supra-materials with tremendous application potential in fields such as energy, electronics, environment and aeronautics [4]. However, the aggregation of nanocarbon materials due to strong intermolecular forces suppresses performance from approaching theoretical values and hinders further application. The construction of 3D carbon frameworks can prevent the stacking and bundling of corresponding low-dimension building blocks (e.g., CNTs and graphene) to shorten diffusion distances for matter and charge and greatly expose active sites to achieve not only rapid charging/discharging for energy storage but also superb activity for catalysis. And despite past progress, comprehensive overviews of 3D carbon-rich hierarchical micro/nanostructures derived from different sources remain lacking. In addition, although 3D porous carbon networks such as aerogels and foams have garnered much attention due to excellent property and broad applications, they will not be the focus of this review (see other reviews [4, 5, 7]).

The focus of this review will be on the recent progress in the design, synthesis and application of 3D hierarchical carbon-rich micro/nanomaterials (3D HCMNs) with well-defined microscale (flower-like, hierarchical tubular superstructures) or macroscale (aligned arrays) structures for energy storage and catalysis (Fig. 1). This review will first briefly discuss the advantageous structural features of hierarchical carbon-enriched materials for electrochemical energy applications in the Sect. 2. Following this, a detailed overview will be provided in terms of synthetic methods and formation mechanisms for 3D nanocarbons (fullerene, carbon nanotubes, graphene, graphdiyne), 3D polymers (polyaniline, polypyrrole, polyimide, polydopamine, graphitic carbon nitride, polyazomethine), 3D covalent/metal organic frameworks (COFs/MOFs), 3D templated carbons and derived carbon-based composites in Sects. 3–6, e.g., "COF and MOF-derived 3D HCMNs" and "6. Templated carbon-based 3D HCMNs". This combined overview of carbon-rich materials from different sources can not only inspire the synthesis of novel 3D structures, but also lead to the discovery of universal guidelines for the construction of 3D structures and provide guidance for the future preparation of carbon-based materials. Subsequently, the electrochemical applications of 3D HCMNs for energy storage and catalysis will be summarized in Sects. 7 and 8 and will include lithium-ion batteries, lithium metal-based batteries, beyond lithium-based batteries (e.g., sodium/potassium/zinc ion batteries), supercapacitors, oxygen reduction reactions, oxygen evolution reactions, hydrogen evolution reactions, nitrogen reduction reactions and photo(electro) catalysis. Finally, this review will conclude with perspectives on major challenges and opportunities in terms of the synthesis, characterization and application of 3D HCMNs in energy storage and catalysis.

2 Advantages of 3D Hierarchical Structures

In energy storage devices, 3D hierarchical structures can guarantee efficient charge transport throughout thick electrodes due to shortened mass and charge transfer pathways to maximize active material utilization irrespective of electrode geometric structure and achieve fast-rate energy storage along with large capacity [8, 9]. 3D hierarchical structures can also provide adequate spacing to buffer volume expansion and enhance long-term cycling stability. In addition, 3D hierarchical carbon materials are promising matrixes for coupling with active materials due to low densities, large surface areas, superb electrical/thermal conductivities and excellent electrochemical stability. Hierarchical nanoarrays on substrates can also be directly employed as self-supporting electrodes without the need for binders or additional slurry casting during electrode fabrication to render seamless contact between active materials and current collectors with minimal internal resistance [8, 10].

As for electrocatalysis, 3D hierarchical structures with large surface areas possess highly exposed active sites as well as reduced charge transfer resistance through the formation of seamless contact with substrates, allowing for enhanced electrolyte penetration, accelerated bubble release rates and suppressed material aggregation. Overall, the most active non-precious water splitting catalysts are based on hierarchical structures [11, 12]. 3D hierarchical structures can also enhance performance in photocatalysis through enhanced light harvesting with minimized optical reflection, improved charge carrier collection through catalyst thickness reduction, increased charge transport through enlarged electrolyte-accessible surface areas, facilitated heterojunction design through the introduction of secondary semiconductors, sufficient spacing to achieve high catalyst loading and finely tuned conduction and valence bands by downsizing building units to nanoscale levels due to quantum size effects [13, 14].

3 Nanocarbon-Based 3D HCMNs

As typical sp^2 nanocarbons, fullerenes, carbon nanotubes (CNTs) and graphene have been the focus of research for decades owing to unprecedented physical and chemical properties and potential application in various fields [4]. In addition, graphdiyne as a novel graphene allotrope with a single layer of alternating sp and sp^2 hybridized carbon atoms is gaining increasing attention in the family of nanocarbons [15]. Moreover, superstructured assemblies of these nanocarbons can produce a family of 1D, 2D and 3D products including fibers, membranes, foams and aerogels [4]. In this review, the focus will be placed on the synthesis and

formation mechanisms of 3D microscopic superstructures and macroscopic nanoarrays from these nanocarbons.

3.1 Fullerene

Fullerene, also known as C_{60} containing 60 carbon atoms, is an icosahedral cage-like molecule with 20 hexagonal and 12 pentagonal faces (Fig. 1a) in which the 60 carbon atoms are conjugated through single and double bonds repeating alternatingly with poor electron delocalization [16]. The construction of complex 3D fullerene-based assemblies can be easily achieved by adopting C_{60} as a building unit due to its poor solubility in organic solvent and easy aggregation with random π–π interactions in which the self-assembly of C_{60} at solvent/non-solvent interface and the introduction of hydrophobic(philic) functional groups have resulted in many molecular-ordered superstructures [17]. As a result, researchers have obtained structurally elegant and functionally promising fullerene assemblies through these complex π–π interactions among fullerene moieties [18].

The morphology of 3D fullerene assemblies can be affected by multiple factors including solvent and temperature. For example, Nakanishi et al. [19] dispersed a C_{60} derivative (Fig. 2a) into a solvent followed by cooling from 60 to 20 °C and aging treatment to precipitate assemblies out of the solution. Fullerene assemblies with varying morphology could be obtained in different solvents. Nanofibers, nanodisks and conical superstructures were generated in 1-propanol, 1,4-dioxane and tetrahydrofuran/H_2O mixed solvent, respectively, in which formed nanodisks 0.2–1.5 μm in diameter and 4.4 nm in thickness (Fig. 2b, c) can subsequently be transformed into 3D flower-like superstructures 3–10 μm in lateral size after cooling to 5 °C (Fig. 2d). Here, the formation process of the assembled flowers involved the initial formation of 2D nanodisks with slightly rolled edges followed by continuous bending into conical shapes and further crumpling and branching into the final flower shape (Fig. 2e), demonstrating that the temperature-dependent morphological transformation was a result of the inherently unstable 2D nanodisks and its energetically stabler bended state in comparison with the stretched state. And as a result of this solution-based self-assembly approach, a series of fullerene-derived flower-shaped assemblies have been developed in subsequent years [16, 17, 20, 21].

Aside from temperature and solvent effects, functional groups grafted onto fullerene can also influence the morphology of resulting assemblies. For example, Zhang et al. [22] synthesized a series of small alkyl (methyl, ethyl, propyl, butyl) benzoate ester group-substituted fullerene derivatives to investigate their self-assembly behavior in which all samples possessed a flower-like supramolecular structure but with varying surface morphology and reported that increasing alkyl lengths led to decreased flake amounts

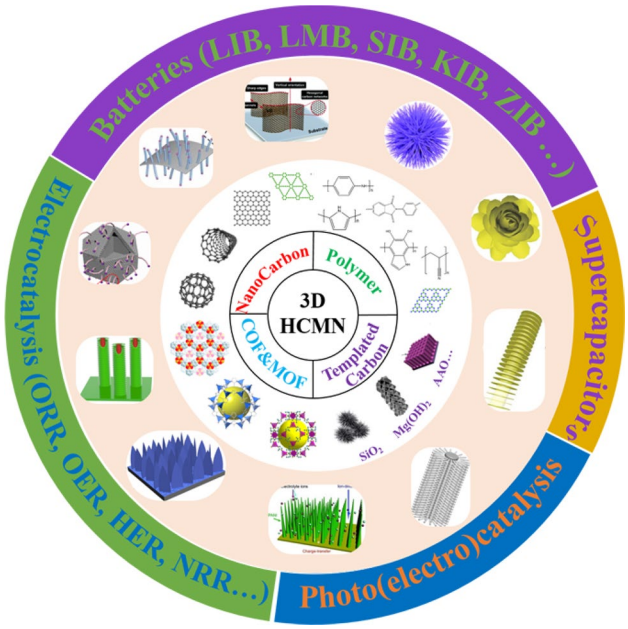

Fig. 1 Schematic illustration of 3D HCMNs, including nanocarbons, polymers, COFs/MOFs and templated carbons with various superstructures such as urchins, flowers and hierarchical tubes as well as nanoarrays on different microscale/macroscale substrates for application in electrochemical energy storage devices (batteries and supercapacitors) and catalysis systems (ORR, OER, HER, NRR). Reprinted with permission from Ref. [40, 82, 107, 181, 308]. Copyright © John Wiley and Sons. Reprinted with permission from Ref. [114, 183]. Copyright © 2019, Elsevier. Reprinted with permission from Ref. [198, 202]. Copyright © Royal Society of Chemistry

being assembled into the resulting flower structure, which these researchers attributed to the delicate balance between π–π interactions and van der Waals forces. Takeuchi et al. [23] further studied a flower-like supramolecular structure obtained through the self-assembly of a C_{60} derivative bearing a pyridine substituent and reported that the simple adjustment of the pyridine nitrogen position can result in the fine-tuning of the morphology from flower-like to spheres of plates and rods in which charge transfer interactions between C_{60} and pyridine nitrogen atoms in the solution can support the flower-like structure with lamellar conformation on the nanometer scale.

In addition to self-assembly, 3D fullerene can further be obtained through template-assisted synthesis. For example, Kim et al. [24] used the anodic alumina oxide (AAO) as a template to prepare perpendicularly aligned fullerene microtube arrays with a hexagonal cross section and high orientation along the crystallographic direction (Fig. 2f) in which the microtubes possessed a 10–30 μm outer diameter and 1–3 μm thick walls (Fig. 2g) and reported that the diameter and density of the fullerene microtubes can be finely tuned by adjusting growth parameters including solvent addition rates and solution quantity.

3.2 CNT

Since discovery in 1991 [25], CNTs have received broad research interests due to excellent physical and chemical properties as prospective materials for the future. Based on the number of walls, CNTs can further be divided into single-walled CNTs (SWCNTs) and multi-walled CNTs (MWCNTs), and with high tensile strength, rapid carrier mobility and large specific surface area, CNTs have been extensively applied in electronics and energy device applications [2]. Despite this, the actual performance of CNTs is far from theoretical values [26] in which performance gaps are partially caused by immature synthetic methods and severe bundling due to strong π–π interactions. The construction of 3D CNTs can alleviate this to some extent however, and based on this, this section will cover the preparation processes of macroscopic CNT arrays and microscale hierarchical CNT superstructures.

Vertical aligned CNT arrays (VACNTs), or CNT forests, are ideal structures to maximize the utilization of individual CNTs due to a fully exposed surface area and have been intensively investigated for energy, catalysis and electronics applications [26]. In terms of synthesis, chemical vapor deposition (CVD) is the most effective method for the vertical growth of CNT arrays. In this process, catalysts are first deposited onto a substrate, activated by chemical etching or thermal annealing and placed into a furnace for CNT growth in which after heating the furnace to desired temperatures (e.g., 600–1200 °C), mixtures of CNT precursor gas and processing gas (nitrogen, argon, hydrogen) are introduced to achieve CNT growth on catalyst surfaces, allowing catalyst particles to remain at the bottom or top of the growing CNTs [27]. Here, commonly used catalysts are based on Fe, Co and Ni in the vertical growth of CNTs due to high carbon solubility and diffusion coefficients. However, other catalysts based on Mn, Cu, W, Mg, Al, Na, Pd and Pt have also been applied [28]. Regardless, corresponding catalyst size plays a decisive role in the diameter of resulting CNTs in which catalysts smaller than < 5 nm mainly yield SWCNTs, catalysts larger than 10 nm mostly generate MWCNTs and catalysts between 5 and 10 nm in size can generate both SWCNTs and MWCNTs. In terms of carbon sources for CNT growth, any carbon-containing materials in gas, liquid or solid states can be used, including hydrocarbons (methane, ethylene, ethanol, benzene, etc.), polymers and biomaterials (camphor, coconut oil, etc.) [28]. However, the molecular structure of the carbon source has significant influence on CNT morphology in which linear hydrocarbons such as methane can generate CNTs with straight hollow structures whereas cyclic hydrocarbons such as benzene likely yield curved CNTs with a bamboo-like structure. As for substrates, materials such as silicon, silicon carbide, silica, graphite, quartz, alumina, magnesium oxide and zeolite are all viable substrates for CNT growth with the most commonly used being silica, zeolite and alumina. Similarly, the surface topology and texture of substrates can further impact the yield and quality of resulting CNT arrays. CVD parameters such as flow rate, reaction temperature and time can also significantly impact the growth rate, length and density of final VACNT arrays.

Overall, the scalable and high-yield preparation of large-area, highly dense and super-long VACNT arrays with controlled CNT diameters, chirality and purity are the ultimate goal for the CVD growth of VACNTs. For instance, Hata et al. [29] used water-assisted ethylene CVD to synthesize highly dense, vertically aligned and impurity-free SWCNT forests on a Si substrate with a height of 2.5 mm and a carbon purity above 99.98% and reported that water was capable of enhancing the activity and lifetime of catalysts that were crucial for the growth of long and pure SWCNT arrays. These arrays can further be separated from substrates and catalysts to enable patterned and highly organized CNT structures. Shanov et al. [30] also applied a water-assisted CVD method to achieve record-long (21.7 mm) VACNT arrays through careful catalyst formulation (Fe–Gd), substrate design and CVD parameter adjustment to maximize catalyst activity time, allowing for a catalyst lifetime of 790 min as well as CNTs with double walls that were uniformly distributed along the growth direction. In another example, Dai et al. [31] obtained metal-free nitrogen-doped VACNT arrays through CVD using iron(II) phthalocyanine, a metal heterocyclic molecule, as the precursor followed by electrochemical purification (Fig. 3a-c) in which the resulting CNTs ~ 8 μm long and ~ 25 nm in outer diameter presented a bamboo-like structure similar to previously reported CNTs (Fig. 3b) and reported that the as-made VACNT film can easily be transferred onto desired substrates for different applications (Fig. 3c). In contrast to thermal CVD involving high reaction temperatures, plasma-enhanced CVD (PECVD) enables low-temperature growth of VACNTs. For example, via PECVD, Wang et al. [32] synthesized vertically aligned MWCNTs on a Si substrate at 180 °C with sputtered FeNi thin films as the catalyst and methane as the carbon source in which the growth mechanism involved the vapor–liquid–solid mechanism.

Despite being controversial, the formation of VACNTs is generally believed to follow the vapor–liquid–solid mechanism, which involves the decomposition of carbon precursor gas contacting with hot catalyst particles to carbon, followed by continuous dissolution of carbon by metal catalysts until the formation of a saturated solid solution in which the further deposition of carbon onto metal catalysts will form carbon nanoparticles that can act as nucleation sites for the subsequent growth of CNTs [33]. Here, metal catalysts remain at the tip or bottom of CNTs depending on the interaction between the catalyst and the underlying substrate in which

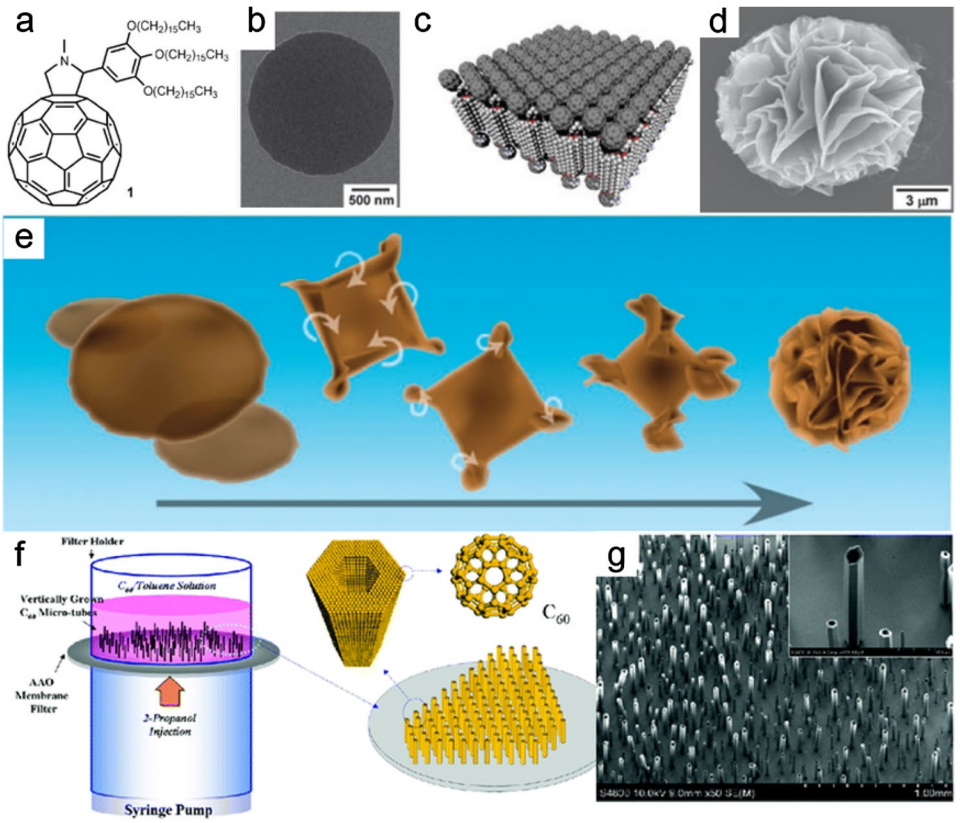

Fig. 2 Fullerene-based 3D HCMNs. Flower-shaped supramolecular assemblies of fullerene derivatives. **a** Molecular structure of a fullerene derivative. **b** SEM image of a disk-shaped ensemble. **c** Proposed molecular arrangement in the disk-shaped ensemble. **d** SEM image of a flower-shaped supramolecular architecture. **e** Schematic diagram for the formation of the supramolecular assembly. Reprinted with permission from Ref. [19]. Copyright © 2007, John Wiley and Sons. Vertical C_{60} microtube arrays. **f** Schematic illustration of the fabrication of vertically aligned crystalline C_{60} microtube arrays. **g** SEM images of the vertically grown C_{60} microtube arrays. Reprinted with permission from Ref. [24]. Copyright © 2008, American Chemical Society

weak interactions will lead to the tip growth mechanism and result in the presence of metals at the tip, whereas strong interactions will lead to the root/bottom growth mechanism.

Arc discharge is another method to produce VACNTs that involves the application of high current between graphitic cathodes and carbon anodes millimeters apart immersed in gas or liquid atmospheres to generate carbon products onto chamber walls or cathode substrates [34]. In fact, the first CNTs discovered by Iijima et al. in 1991 were obtained based on this method. As an example, Cai et al. [35] achieved the catalyst-free synthesis of VACNTs through hydrogen arc discharge using graphite powder as the carbon source in which the resulting CNTs possessed a bamboo structure with lengths of ~ 30 μm and diameters of 40–60 nm. Here, the activation of hydrogen radicals, construction of anode with enlarged sizes and the vertical electrical field on the anode surface are regarded as critical factors for the growth of VACNTs.

Besides the vertical growth of CNT arrays on planar substrates, hierarchical CNT arrays have also been grown on curved macro-sized or micro-sized substrates through predeposited or in situ generated catalyst-assisted approaches. For example, Hou et al. [36] were able to prepare hierarchical CNT arrays on carbon nanofibers through the carbonization of electrospun polymer/metal nanofibers followed by the CVD growth of CNTs with hexane as the carbon source in which Fe nanoparticles were in situ generated on the surface of the polymer-derived carbon nanofibers during pyrolysis that functioned as a catalyst for the subsequent growth of the CNT arrays. Zeng et al. [37] also reported a similar strategy for the CVD synthesis of hierarchical CNT arrays onto commercial carbon cloth (CC) with ethanol as the carbon source and Ni as the catalyst.

Recently, hierarchical CNT arrays have also been prepared through the direct carbonization of MOFs. For example, Lou et al. [38] synthesized hollow structured hierarchical CNT frameworks by pyrolysis of ZIF-67 in the H_2 atmosphere, in which H_2 was found to be crucial for the generation of hierarchical CNTs. Amazingly, ZIF-67 as the single precursor was able to provide tri-sources including carbon, catalyst and substrate for CNT growth. In the presence of H_2, Co nanoparticles can be in situ generated during thermal heating, which further catalyzes the growth of CNT arrays on the surface of carbon polyhedron, giving rise to hierarchical CNT frameworks. The interior hollow structure is a result of the fast consumption of inner carbon for growing outer CNT arrays. And as a result, a hierarchical CNT framework synthesized at 700 °C possessed a hierarchical CNT shell thickness of ~ 200 nm, a CNT length of several hundred nanometers, a high surface area of ~ 513 $m^2 g^{-1}$ and a pore volume of 1.16 $cm^3 g^{-1}$ (Fig. 3d–f). These researchers further reported that the length and density of the CNT

arrays can be controlled by simply adjusting pyrolysis temperatures in which at a lower temperature of 600 °C, the surface of the CNT framework displayed many short CNT clusters whereas at a higher temperature of 900 °C, longer CNT arrays with higher densities were achieved. Mai et al. [39] further modified this strategy for the general synthesis of hollow structured hierarchical CNT frameworks from various Fe-, Co-, Ni-based MOF precursors at a temperature as low as 430 °C under H_2-free Ar atmosphere but with long heating time in which low-temperature pyrolysis can ensure small-sized metal catalysts with higher activity for CNT growth. Regardlessly, residual metal nanoparticles are found at the tips of the CNTs in both examples, implying a tip growth mechanism (Fig. 3g). Fang et al. [40] also extended the MOF-derived CNT strategy to obtain 3D CNT/graphene hybrids embedded with single, binary or even ternary metal nanoparticles in which the growth of core–shell MOFs with Zn-MOF as the core and (Fe, Co, Ni, or Cu)-based MOFs as the shell onto graphene oxide can guarantee the homogeneous distribution of Fe, Co, Ni or Cu species within the MOFs, which is crucial for the generation of uniform CNT arrays on graphene. Aside from CNT growth, the carbonization of MOF also enables conformal heteroatom doping into CNT-based frameworks.

Microwave radiation is another approach to make hierarchical CNTs. For instance, Lee et al. [41] reported that the microwave radiation treatment of a mixture containing ferrocene, graphene oxide and azodicarbonamide (ADC) can give rise to hierarchical iron–CNT graphene hybrids constructed from 0D nanoparticles, 1D CNTs and 2D graphene (Fig. 3h) [41]. Under microwave irradiation, graphene oxide can expand to graphene nanoworms first through microwave heating and subsequently through gaseous products generated from the decomposition of ADC. Meanwhile, ferrocene decomposes into iron nanoparticles anchored onto graphene as the catalyst and to hydrocarbons as the carbon precursor for subsequent CNT growth on the graphene surface. And under secondary microwave irradiation, smaller carbon nanotubes with branched structures can be grown on the as-prepared graphene–CNT hybrids, which will lead to the formation of hierarchical CNT/graphene hybrids. More examples of 3D CNT/graphene hybrids will be described in the graphene section of this review.

Impressively, low-temperature hydrothermal reactions can also generate branched CNT superstructures. For example, Adenrian et al. [42] hydrothermally treated a mixture of carbon tetrachloride, ferrocene and Ni at 180 °C to obtain a product with urchin-shaped amorphous CNT superstructures 180–300 nm in diameter and ~ 25 nm in wall thickness in which the proposed formation mechanism involved the reduction of ferrocene under hydrothermal treatment to Fe nanoparticles that can act as catalysts to trigger the growth of carbon tetrachloride-derived CNTs onto microscale Ni substrates. As a result, the as-made 3D CNTs

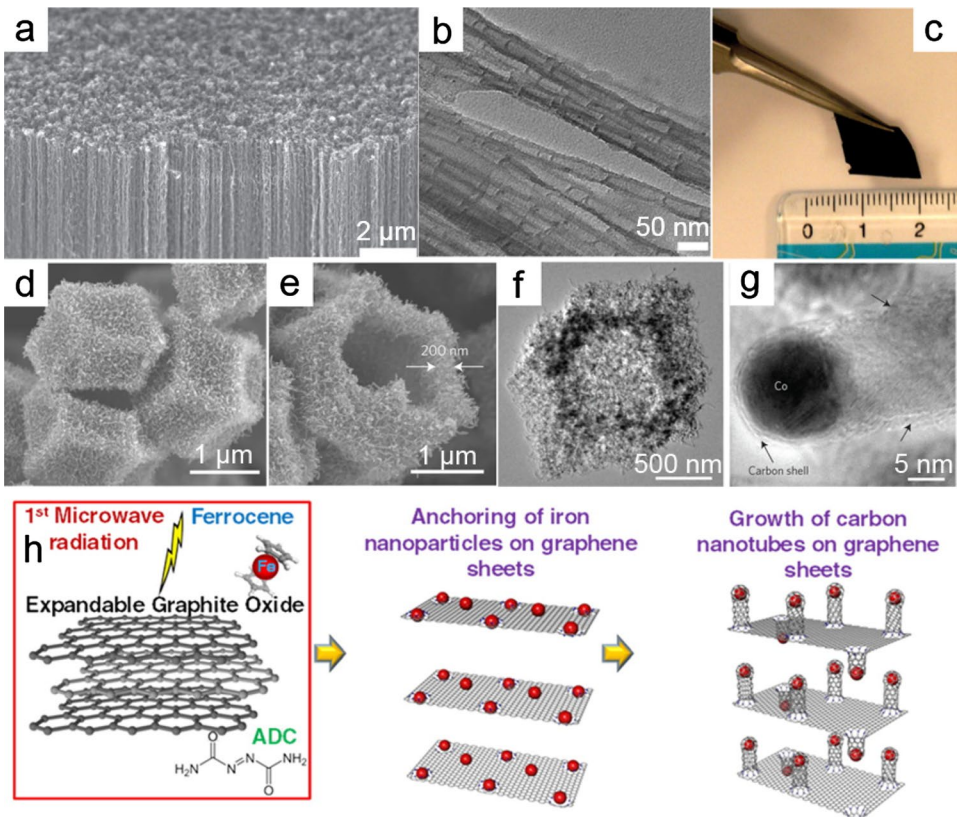

Fig. 3 CNT-based 3D HCMNs. N-doped CNT arrays. **a** SEM image of vertically aligned N-containing CNTs (VA-NCNTs). **b** TEM image of electrochemically purified VA-NCNTs. **c** Digital photograph of the VA-NCNT array transferred to a flexible film. Reprinted with permission from Ref. [31]. Copyright © 2009, American Association for the Advancement of Science. N-doped carbon nanotube frameworks (NCNTFs). **d, e** FESEM, **f** TEM and **g** HRTEM images of NCNTFs showing numerous CNTs on the surface. Reprinted with permission from Ref. [38]. Copyright © 2016, Springer Nature. **h** Synthesis of a 3D graphene–nanotube–iron (G-CNT-Fe) superstructure via microwave radiation-induced CNT growth. Reprinted with permission from Ref. [41]. Copyright © 2013, American Chemical Society

possessed a surface area of 470 $m^2\ g^{-1}$ and a pore volume of 0.39 $cm^3\ g^{-1}$ that increased to 1479–3802 $m^2\ g^{-1}$ and 0.83–2.98 $cm^3\ g^{-1}$ after chemical activation.

Carbon nanofibers (CNFs) [43], as another 1D carbon nanomaterial, have received tremendous research interest as well, and corresponding 3D CNF arrays can be prepared through methods such as CVD and template-assisted methods similar to that of CNTs. In addition, both CNTs and CNFs can act as substrates for the growth of materials to synthesize 3D carbon-based composites [44, 45].

3.3 Graphene

Graphene, the winning subject of the 2010 Nobel prize, possesses one-atom-thick sp^2 carbon lattices and can exhibit superb mechanical, thermal, chemical and electrical properties [4]. As such, graphene is considered to be the wonder material of the twenty-first century. Due to strong π–π interactions however, the superior advantages of graphene are inhibited by the aggregation (restacking) of nanosheets, and therefore, the construction of 3D graphene is necessary to fully expose 2D surfaces [4]. In this section, the fabrication of graphene superstructures with flower and honeycomb structures as well as vertically oriented graphene nanoarrays is summarized.

Unlike 2D flat graphene sheets, 3D flower-like graphene microspheres possess highly accessible surface areas even under tight packing. Based on this, Huang et al. [46] proposed the construction of flower-like graphene balls by spray drying in which the graphene oxide (GO) dispersion as a feedstock was atomized into aerosol droplets and subjected to rapid liquid evaporation in a furnace to transform the GO sheets into flower-like crumpled balls due to capillary compression, resulting in crumpled GO balls that are highly stabilized due to π–π stacked ripples and plastic deformation and aggregation resistant in either solution or solid state. Via this method, graphene-based hybrids such as graphene/Si hybrids with crumpled graphene shells wrapped around the other components can also be facilely prepared through the simple introduction of additional components to graphene oxide in aerosol droplets [47]. Gao et al. [48] further prepared flower-shaped GO (fGO) powder with a highly porous structure through low-temperature spray drying and demonstrated that fGO was more easily processed and scalable as compared with other graphene materials such as aerogels and foams. What is more, the fGO powder can be redissolved in water at the molecular level at high concentrations to enable large-scale transportation, storage and application. In another study, Park et al. [49] developed another spray-assisted self-assembly strategy to prepare 3D hierarchical graphene microspheres using high-temperature organic solvents similar to deep-frying in which the resulting graphene spheres possessed a flower shape (Fig. 4a, b). This method can also efficiently produce 3D graphene-based hybrids, allowing Si nanoparticles to be trapped by graphene nanosheets during the assembly. Template-assisted method is another approach to prepare hierarchical graphene balls. For example, Lee et al. [50] encapsulated iron oxide nanocubes as the template with GO and carried out the simultaneous etching and reduction of GO-coated iron oxide particles to enable the gradual removal of the template to form a thorny morphology as well as the reduction of the GO to rGO layers with a hydrophobic surface to maintain the graphene layer during template removal. As a result, hierarchical crumpled graphene balls with reduced diameters were obtained that possessed high surface areas and water dispersion stability.

A dynamic interfacial self-assembly strategy was reported to prepare 3D honeycomb-shaped graphene assemblies with polygonal nanopores (~ 40 nm) interconnected by silicon-oxygen chemical bonds (Fig. 4c–g) [51]. Inside a quartz tube (SiO_2) was added sodium metal (ca. 0.97 g cm^{-3}) to a mixture of GO aqueous solution (ca. 1.0 g cm^{-3}) and orthoxylene solvent (ca. 0.88 g cm^{-3}). Due to density differences, the sodium balls can remain in the middle of the mixture and react with water to form a strong alkaline solution that can corrode the inner walls of the quartz tube to generate Na_4SiO_4 (Fig. 4c). This silicate can subsequently react with GO to facilitate graphene self-assembly at the oil/water interface to obtain a highly ordered 3D porous structure due to the Si–O–C linking directional orientation related to the silicate tetrahedral configuration as well as hydrogen bubbles that can serve as a pore-forming template. And because this interfacial self-assembly process is dynamic in which the sodium balls will move up and down repeatedly due to in situ generated hydrogen bubbles and gravity, 3D graphene assemblies will be produced continuously until the complete consumption of sodium. In corresponding SEM images (Fig. 4e, g), the obtained 3D graphene assembly was found to possess a thickness of ~ 200 nm and vertical graphene nanowalls with a wall thickness of ~ 19 nm, which forms polygonal nanopores with mechanical stability and deformability along with a hardness of 13.09 GPa, a Young's modulus of 162.96 GPa, an elastic recovery of 75.27% as well as excellent thermal stability that were considerably better than previously reported graphene assemblies and carbon aerogels.

Compared with microscale hierarchical graphene, macroscale vertically oriented graphene arrays (VGAs), also referred to as graphene nanowalls, have received extensive attention due to unique morphological and structural features and exciting properties [52]. In terms of synthesis, arc discharge and PECVD are two common method used to prepare VGAs in which gas, liquid or solid precursors can be used in the PECVD growth of VGAs on various substrates and

plasma can be adjusted to achieve the efficient, low-temperature and catalyst-free preparation of VGAs with desirable morphology. The PECVD approach enables growth of VGA on literally arbitrary substrates [53]. For example, Wang et al. [54] grew VGAs on a planar n-type Si wafer using radio frequency PECVD with a methane-hydrogen mixture gas as the feedstock. Ren et al. [55] also obtained high quality and pure VGAs with ultrathin graphene edges and narrow height distributions on nickel foam involving the removal of nickel foam surface oxides and the growth of VGAs through microwave PECVD using CH_4/H_2 gas as the carbon precursor, resulting in the vertical growth of graphene a few micrometers in height on both the inner and outer surfaces around the Ni foam (Fig. 4h). Alternatively, VGAs can be uniformly grown on cylindrical substrates such as metal wires in both circumferential and axial directions through atmospheric pressure glow discharge in mixture gases of CH_4, H_2O and Ar [56]. VGAs can further be grown on micro- and even nanoscale substrates. For example, Chang et al. [57] coated CC with VGAs through radio frequency magnetron sputtering in an $Ar–H_2$ gas mixture in which the thickness and lateral size of the graphene nanosheets were ~ 5 to 10 nm and 300 nm, respectively. VGA flakes can also seamlessly integrate with CNTs through the formation of sp^2 covalent bonds [58].

Despite tremendous efforts, the formation mechanisms of VGAs remain unclear. However, the probable mechanism of VGA formation involves three steps (Fig. 4i–k) [59, 60] in which the first step involves the formation of random cracks and dangling bonds as a buffer layer on targeted substrates that can later function as nucleation sites for graphene growth, whereas the second step involves the vertical growth of graphene followed by the incorporation of carbon atoms onto the as-formed graphene edges under mechanical stress and local electric fields. As for the third step, this involves the termination of VGA growth due to competition between carbon deposition and etching effects in plasma. Overall, VGA formation is a result of local electric fields, internal mechanical forces and anisotropic growth.

Based on theoretical studies, the combination of CNTs and graphene into 3D superstructures with seamless connections can impart desirable properties that outperform the simple mixing of 1D CNTs with 2D graphene. Based on this, Wei et al. [61] prepared 3D carbon sandwich structures with vertical CNT pillars bridging graphene layers using CVD and Du et al. [62] using a similar method prepared 3D pillared CNT-graphene superstructures through the intercalated growth of VACNTs with tunable lengths into expanded pyrolytic graphite. Chen et al. [63] further prepared a unique hierarchical nanohybrid involving porous CNT network decorated crumpled graphene balls through the deposition of metal nanocatalysts onto graphene balls and subsequent catalytic growth of CNT, whereas Tour et al. [64] achieved the seamless bonding of graphene with SWCNT through the careful design of the CVD process in which the resulting hybrid with ohmic contact between the VA-SWCNT and the graphene possessed high surface areas larger than $2000\,m^2\,g^{-1}$ and aberration-corrected STEM revealed the covalent transformation of sp^2 carbon between the graphene and the vertical SWCNT at the atomic level.

3D macroscopic CNT/graphene can also be obtained by using PECVD. For example, using this method, Kim et al. [65] prepared a CNT–graphene hybrid film with vertically oriented and patterned CNT arrays grown on graphene in which a uniform GO film was first coated onto a Si wafer through spin coating followed by the deposition of patterned iron nanoparticles via block copolymer nano-templates. In another example, Xue et al. [66] prepared 3D graphene–CNT hollow fibers with radially aligned CNTs seamlessly connected with a cylindrical graphene layer by combining CVD with AAO wire templates in which the length of the CNTs and the diameter of the graphene hollow fibers can be finely tuned by varying the diameter and anodization time of the AAO wire.

3.4 Graphdiyne

Graphdiyne (GDY) as an emerging 2D nanocarbon with atom-thick layers of sp and sp^2 co-hybridized carbon networks has been receiving increasing attention in the fields of chemistry and materials science due to unique chemical and physical properties with appealing prospects in many applications, particularly in the fields of energy and catalysis [67]. Since its first successful synthesis in 2010, various synthetic methods have been developed to prepare GDY with various morphology such as nanotubes [68], nanowires [69], nanofilms [70], nanocoatings [71] and stripe arrays [72]. This section will summarize the progress of 3D GDY synthesis, particularly GDY nanoarrays on substrates and freestanding GDY superstructures.

3D GDY nanotube arrays were first reported by Zhu et al. [68] in 2011 through the cross-coupling reaction of hexaethynylbenzene (HEB) in the presence of pyridine, an AAO template and a Cu foil catalyst. Al–O bonds in the AAO template can interact with acetylenic hydrogen in the HEB through hydrogen bonding to allow for the formation of HEB films to induce subsequent Cu-catalyzed cross-coupling reactions. These reactions will continue until catalytic centers are quenched to form nanotube arrays inside the AAO template wall, resulting in the as-prepared nanotubes possessing a smooth surface with a diameter of ~ 200 nm and a wall thickness of ~ 40 nm that is reduced to ~ 15 nm after annealing. Liu et al. [73] further used a wet chemical approach in 2015 to synthesize GDY nanowalls on Cu surfaces through a modified Glaser–Hay coupling reaction in which HEB served as a monomer and Cu as a substrate

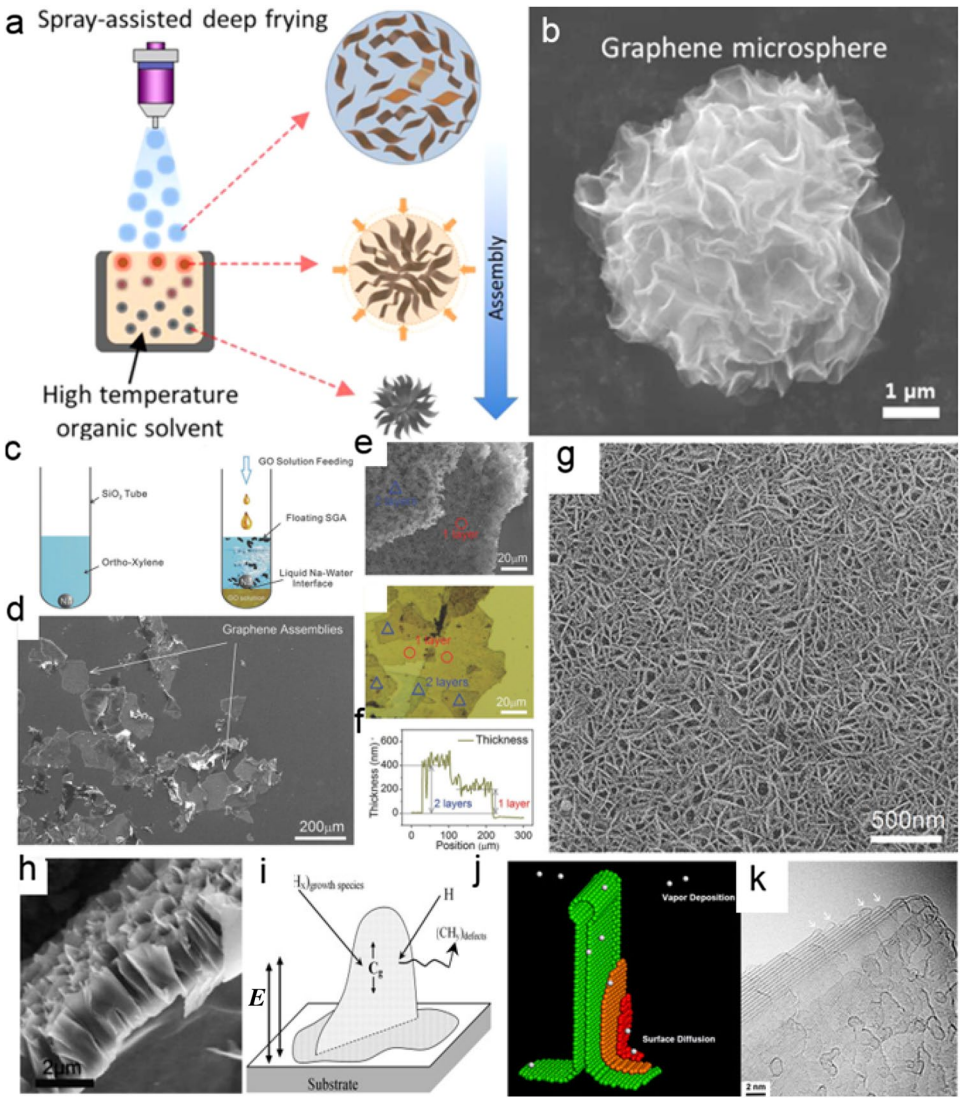

Fig. 4 Graphene-based 3D HCMNs. Crumpled graphene flower preparation. **a** Schematic of the synthesis of graphene flower through spray-assisted deep-frying. **b** SEM image of the graphene sphere with the flower shape. Reprinted with permission from Ref. [49]. Copyright © 2014, American Chemical Society. **c-g** Silicate-bridged graphene assemblies (SGAs). **c** Synthetic process of SGAs. **d-g** SEM images, optical microscope image and height profile of SGAs. Reprinted with permission from Ref. [51]. Copyright © 2018, John Wiley and Sons. **h** VGAs on Ni foam. Ref. [55]. Copyright © 2016, Elsevier. **i-k** Mechanism for the vertical growth of graphene nanosheets. **i** A vertical graphene model. Reprinted with permission from Ref. [59]. Copyright © 2007, Elsevier. **j** Continuum model based on surface diffusion and moving boundary. **k** TEM image showing the boundary of the vertical grown graphene. Reprinted with permission from Ref. [60]. Copyright © 2014, American Chemical Society

(Fig. 5a). Here, these researchers controlled the amount of organic alkali and monomer added to allow for the dissolution of certain amounts of Cu into Cu ions in the solution to serve as catalytic sites. Due to the fast kinetics of the Glaser–Hay coupling reaction, GDY grew perpendicularly at catalytic sites and subsequently formed uniform nanowalls on the Cu substrate upon further reaction, allowing for continuously and uniformly distributed vertical GDY nanowalls on the substrate with large pores between nanosheets with a diameter of submicrometers, a height of hundreds of nanometers and a nanosheet thickness of several nanometers (Fig. 5b–d). In 2016, the same group employed the similar strategy to grow 3D ordered vertical honeycomb-shaped GDY on Cu foam in which Cu foam can act as both a reaction catalyst and a robust substrate to support the 3D GDY structure. And as a result of the presence of multilevel pores in the 3D macroporous foam and the meso-/microporous GDY honeycomb structure, the resulting hybrid foam demonstrated high surface areas and enhanced roughness. In 2017, Zhang et al. [74] subsequently extended this method to grow 2D GDY arrays on Cu foam-supported 1D $Cu(OH)_2$ arrays and obtained hybrid hierarchical arrays with promising characteristics.

Overall, these results seem to suggest that GDY can only be synthesized on Cu substrates, which will significantly limit application if true. To tackle this issue, Zhang et al. [75] developed a Cu envelope catalyst strategy to fabricate GDY on arbitrary substrates (Fig. 5e). Adding GDY monomers into alkaline solution in the presence of Cu envelope-encapsulated substrates can transform Cu into Cu–pyridine complexes that can function as free-moving catalysts for acetylenic coupled reactions and the in situ growth of GDY on the substrates. In addition, the envelope from the folded Cu foil can function as not only the catalyst reservoir but also the container for the substrates. Accordingly, vertical growth of GDY nanosheet arrays was achieved on 1D (Si

nanowires, Fig. 5f), 2D (Au foil, Fig. 5g, quartz, and W foil) and 3D substrates (graphene foam and stainless steel mesh, Fig. 5h). Figure 5i is a TEM image of GDY nanowall peeled from Au foil showing the hierarchical porous network, and the tilted SEM image (inset of Fig. 5i) suggested a wall thickness of ~ 180 nm.

Beyond macroscale substrates, microscale templates can also be grown with hierarchical GDY. For instance, Liu et al. [76] obtained a freestanding 3D GDY structure using Cu nanoparticles as the catalyst and diatomite as the substrate in which a simple metallic replacement reaction was used to absorb Cu nanoparticles onto diatomite to give rise to Cu/diatomite composites, followed by the growth of 3D GDY on the diatomite surface and the removal of the Cu nanoparticles and diatomites through etching. And because Cu nanoparticles possess higher surface areas and are cheaper as compared with macroscopic Cu substrates, corresponding applications are more promising in the massive production of 3D GDY-based hierarchical structures.

Aside from the construction of individual 3D GDY structures, 3D GDY can also be easily coupled with other nanomaterials such as CdSe quantum dots [77], $BiVO_4$ nanorods [75], Co nanoparticles [78] and NiFe LDHs [79] to make 3D GDY-based nanohybrids for different applications.

4 Polymer-Derived 3D HCMNs

Over the last century, polymers with various structures, rich functional groups and broad range of properties have been widely applied in day-to-day life [80]. Polymer nanomaterials with different structures ranging from 0D to 3D have further been reported in past decades [81]. Due to novel opportunities presented by 3D structures, the development of 3D polymers to enhance various applications is also extremely promising in which the self-assembly capability and tunability of polymers at different levels from atoms to molecules to polymerizations can enable the construction of 3D polymers [81]. Polymer crystals such as spherulites and shish-kebab crystals are also typical 3D superstructures. Moreover, thermally stable 3D polymers can easily be converted into 3D carbon materials with well-preserved hierarchical structures, high electrical conductivities and tunable heteroatom dopants, showing potential in energy storage and conversion devices. Based on this great potential, the progress on the synthesis and application of 3D hierarchical polymer-derived micro-/nanomaterials needs to be summarized but remains lacking. To address this, this review will comprehensively present the synthetic approaches and formation mechanisms of 3D polymers including conducting polymers, polyimides, polydopamines, graphitic carbon nitrides, polyazomethines and other polymers in the following sections.

4.1 Conducting Polymers

Over the past decades, conducting polymers have garnered tremendous research interest due to unique electrical conductivities, redox activities and potential application in multidisciplinary areas such as electronics, electrochemical, electro-luminescence and sensor [82]. Among various conducting polymers, polypyrrole (PPy), polyaniline (PANI) and derivatives have been extensively studied [82]. To produce conducting polymers with 3D hierarchical structures such as urchins, flowers and ordered nanoarrays, different approaches have been demonstrated, including chemical polymerization, electrochemical polymerization and templated synthesis.

The template method has been widely used to synthesize 3D hierarchical conducting polymers with common templates being AAO films and hierarchical metal oxides [83]. For example, Cao et al. [84] combined AAO-templated synthesis with electrodeposition to obtain PANI nanowire or nanotube arrays and reported that deposition time, monomer concentration, electrochemical voltage and electrolyte concentration can all impact final PANI morphology. Particularly, a higher acidic concentration can transform solid PANI nanowires into hollow PANI nanotubes. Here, the formation of varying morphology can be explained by using different nucleation and growth models interpreted from current transient data. Using similar approaches, Fang et al. [85] used ammonium vanadate nanowire arrays as a sacrificial template to electrodeposit PPy nanotube arrays onto carbonized cotton textile whereas Pan et al. [86] used urchin-shaped MnO_2 as a sacrificial template to fabricate hierarchical tubular PANI (Fig. 6a,b) and reported that the formation mechanism involved the simultaneous reduction of MnO_2 to soluble Mn^{2+} ions and the oxidative polymerization of PANI onto the MnO_2 template surface, which can be used to achieve a series of PANI micro/nanostructures by simply varying the MnO_2 structure.

Besides templated synthesis, 3D conducting polymers can also be prepared by electrochemical polymerization. For example, Liang et al. [87] conducted stepwise electrochemical polymerization to achieve the large-area growth of PANI nanowire arrays on various substrates including Pt, Si, Au, C and SiO_2 with the as-prepared PANI nanowires possessing diameters < 100 nm and lengths of ~ 0.8 μm in which the polymerization process involved the initial use of a large current (0.08 mA cm^{-2}) followed by the use of a reduced current at 0.04 mA cm^{-2} for 3 h and another 3 h at a lower current of 0.02 mA cm^{-2}. And based on observations that

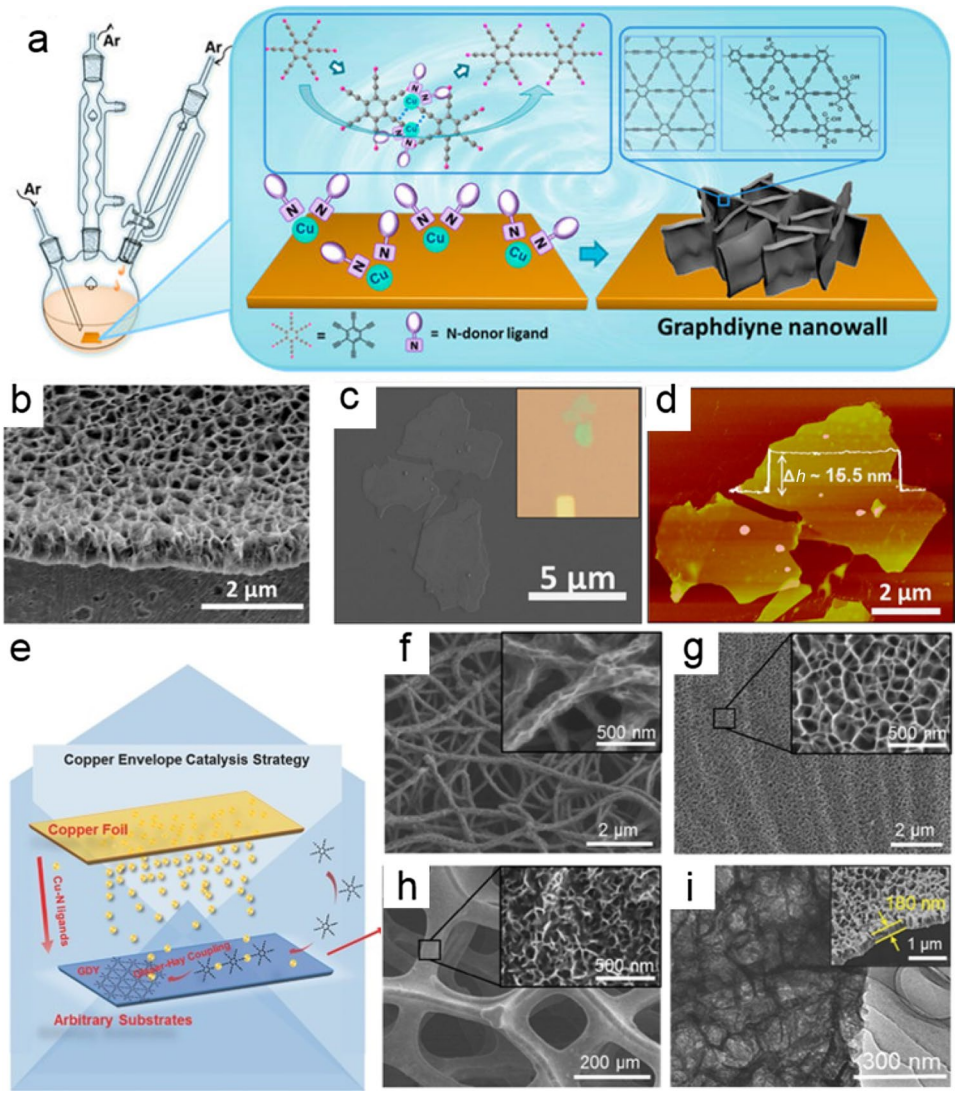

Fig. 5 Graphdiyne-based 3D HCMNs. GDY nanowall grown on Cu foil. **a** Scheme showing the fabrication of GDY nanowalls. **b** SEM image of GDY nanowalls on Cu substrate. **c** SEM image, the OM image (inset of **c**) and **d** AFM image of GDY nanosheets exfoliated from nanowalls. Reprinted with permission from Ref. [73]. Copyright © 2015, American Chemical Society. GDY nanowalls on arbitrary substrates. **e** Cu envelope synthesis of GDY nanowalls. SEM images of GDY nanowall-coated substrates: **f** 1D silicon nanowires, **g** 2D Au foil, **h** 3D Ni foam. **i** TEM image showing peeled GDY nanowalls with a continuous porous network. Reprinted with permission from Ref. [75]. Copyright © 2016, John Wiley and Sons

homogenous and aligned nanowires can only form if a gradually decreasing current density is applied, these researchers proposed a formation mechanism: high current densities can facilitate the nucleation of PANI on substrates whereas low current densities favored polymer growth accompanied by nucleation. Wang et al. [88] subsequently developed a one-step process to grow PANI arrays. Contrary to the previous study, they found that a low current density of 0.01 mA cm^{-2} can also trigger polymer nucleation that enables the growth of PANI on nuclei protuberances to form nanowire arrays under extended time periods, possibly due to edge effects with high electric fields, thus providing an electrochemical strategy that can be applied to all electrically conductive substrates and conducting polymers. For example, Li et al. [89] electrochemically polymerized PPy in an oil/water biphasic electrolyte into large-area aligned nanowire arrays with average diameters of ~ 90 nm and controlled lengths in the range of 1–4 μm. Huang et al. [90] further reported that the modification of electrolyte solution and electrodeposition parameters can achieve the electrochemical growth of PPy in homogenous solutions. Apart from aligned arrays, electrochemical polymerization can also generate microscale superstructures of conducting polymers. For example, Niu et al. [91] were able to synthesize self-doped PANI micro-flowers with uniform size distribution through the electrodeposition of o-aminobenzenesulfonic acid and aniline.

Dilute chemical polymerization is another powerful approach to obtain conducting polymer arrays, particularly PANI nanofiber arrays on both conductive and non-conductive substrates [92]. The formation mechanism of the aligned PANI nanofibers involves the preferential nucleation of dilute polymer precursors (e.g., aniline at low concentrations) on substrates (e.g., GO, Fig. 6c) to minimize interfacial energy, following heterogeneous nucleation, and subsequently further polymerization and growth of PANI occur on these

formed nucleation sites. Meanwhile, polymerization can also occur in bulk solution to form self-assembled PANI large nanofibers due to homogeneous nucleation. The competition between homogenous and heterogenous nucleation depends on polymer concentration, meaning that the careful selection of substrates, polymer concentrations and polymerization times is key to the controllable synthesis of conducting polymer arrays. Because of this, this method can generally be applied to any substrates that are stable in acidic media, including microscale substrates such as GOs and SWCNTs as well as macroscopic substrates such as CNT yarns, graphene films, polymer films, patterned substrates and carbon aerogels [93–100]. As an example, Wei et al. [94] adopted dilute polymerization to achieve the vertical growth of PANI nanofibers on both sides of GO (Fig. 6d, e) in which GO acting as heterogeneous nucleation sites for PANI growth in dilute monomer solution is critical for the formation of hierarchical PANI/GO hybrids. This dilute polymerization method in the absence of substrates can further generate PANI multidimensional structures from nanoplates to micro-flowers [101] in which nanoplates can be prepared at low molar ratios of oxidant to monomer whereas higher molar ratios will result in flower-like superstructures. The influences of monomer concentration on PANI structure and time-dependent formation processes have also been explored.

Alternatively, Yang et al. [102] adopted an evaporation-induced self-assembly strategy to grow PPy nanowall arrays on substrates to give arrays of interconnected vertically aligned PPy nanosheets to form nanowalls on Ni foam with a nanosheet thickness of ~ 14 nm and a nanowall height of ~ (294 ± 34) nm (Fig. 6f, g). The possible formation mechanism (Fig. 6f) involves the initial formation of a "sea-island" film on hydrophobic Ni foam with pyrrole as the sea and water as the island as a result of the different solubilities of pyrrole in ethanol and water as well as the different evaporation rates of the two solvents. The subsequent oxidative polymerization of pyrrole is confined to the "sea" structures separated by "islands" to lead to PPy growth along the direction normal to the substrate. This proposed mechanism was further validated through control experiments in which the polymerization of PPy in the absence of the Ni foam substrate or the evaporation process only produced PPy nanoparticles.

4.2 Polyimide

Polyimides (PIs), defined as polymers that possess imide groups "–CO–NH–CO–" in the main chain, are commonly used in high-performance engineering plastics and mainly exist in the forms of membranes, fibers and adhesives. PIs enjoy application in a variety of fields ranging from microelectronics to aerospace [103] as a result of high mechanical strength and excellent chemical and thermal stability that can further be modulated by varying corresponding molecular structures and processing techniques [104]. Here, typical PI synthesis involves polycondensation reactions between dianhydride and diamine in solvent followed by subsequent thermal or chemical imidization. And due to its outstanding thermoresistant properties, PI can further be used as precursors for carbon and graphite fabrication, including carbon/graphite membranes, fibers and foams [105] as well as graphene through simple laser treatments [106].

Currently, several methods can be used to synthesize 3D PI-based hierarchical micro/nanomaterials, including solvothermal polymerization and surface-assisted dilute polymerization in which solvothermal polymerization involves the mixing of dianhydride and diamine in aprotic solvent to form a polyamic acid solution followed by polycondensation reactions in a Teflon-lined autoclave under high temperature and pressure to simultaneously achieve polymerization and self-assembly, resulting in aggregates of 3D PIs with hierarchical structures. For example, Feng et al. [107] were able to fabricate both PI and carbon superstructures through solvothermal polymerization and subsequent thermal treatment (Fig. 7a). The formation of PI superstructures (e.g., flower) with tunable building units (e.g., petals) is analogous to spherulite formation with both following a hierarchical self-assembly mechanism. PI solvothermal polymerization also exhibits an unusual concentration-dependent morphological evolution process in which by adjusting polymerization conditions, PI self-assembly behavior can readily be controlled to result in novel superstructures such as flower-, disk- and lantern-like structures. And thanks to high thermal stability, these PI superstructures can be well preserved in derived carbon superstructures following pyrolysis and activation. Feng et al. [107] also reported that hierarchical structures can influence surface areas in resulting N-doped porous carbon superstructures in which among all hierarchical structures, the packing of nanosheets into flowers can maximize the exposure of surfaces (Fig. 7b) to generate optimal surface areas up to 1375 $m^2 g^{-1}$. This strategy was also applied to various molecular building blocks to synthesize a series of 3D PI and carbon superstructures, including rose-shaped, gear-like, spherulite-like and cornflower-shaped carbon structures [108–113].

As for surface-assisted dilute polymerization, it involves the introduction of a substrate to a dilute polymer precursor solution to allow for the preferentially heterogeneous rather than homogeneous nucleation and growth of polymers onto the substrate surface during polymerization to result in the formation of 3D hierarchical PI arrays on the substrate. Following polymer nucleation, further polymerization and growth of PI into ordered superstructures occur to minimize total surface energy, which is akin to that of conductive polymers. In a representative example, Wu et al. [114] used MoO_3 nanorods as a structure-guiding template in the

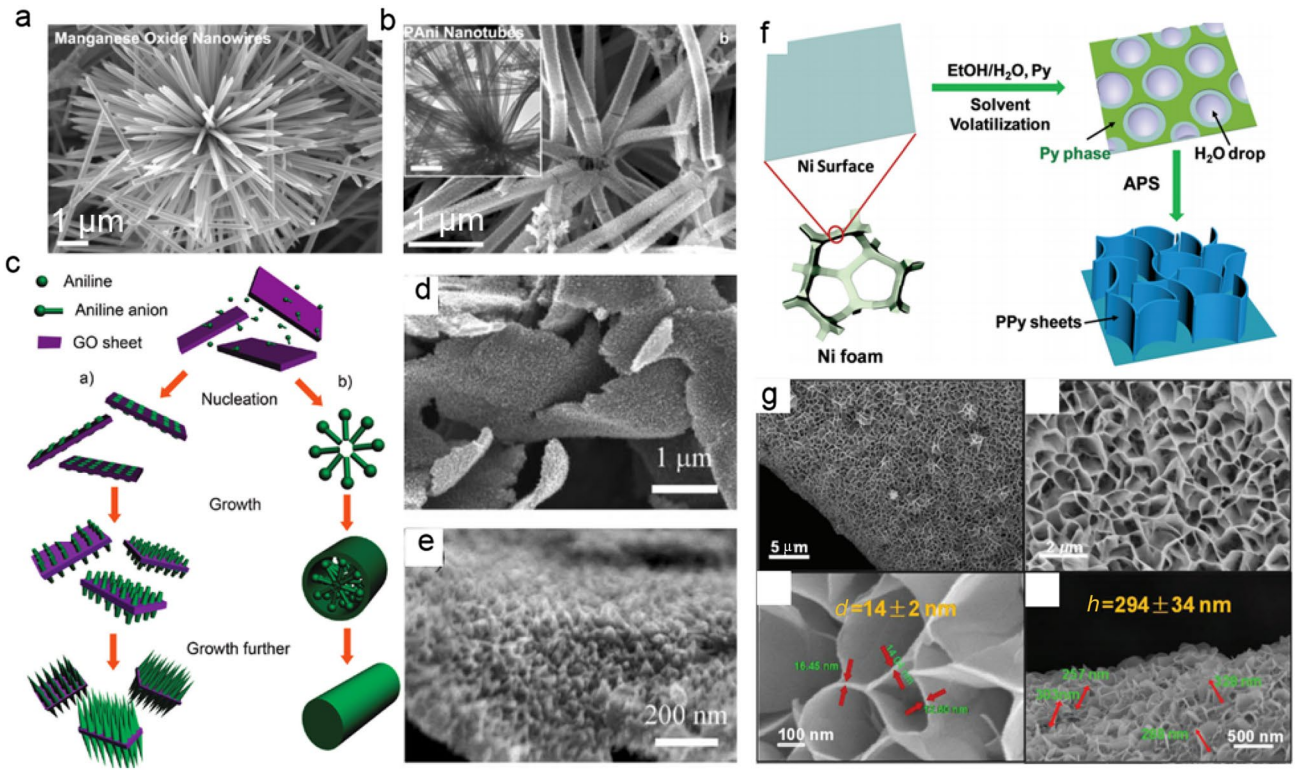

Fig. 6 Conducting polymer-derived 3D HCMNs. **a** SEM images of urchin-shaped MnO_2 and corresponding **b** hierarchical tubular PANI structure. Reprinted with permission from Ref. [86]. Copyright © 2007, John Wiley and Sons. PANI nanowire arrays on graphene oxide sheets. **c** Schematic representation of the nucleation and growth of PANI nanowires with or without substrates. **d, e** SEM images of hierarchical PANI/GO nanohybrids. Reprinted with permission from Ref. [94]. Copyright © 2010, American Chemical Society. Vertical PPy nanosheets on Ni foam. **f** Scheme showing the template-free synthetic procedure. **g** SEM images of vertical PPy nanosheets. Reprinted with permission from Ref. [102]. Copyright © 2016, Royal Society of Chemistry

synthesis of PI and carbon tube-sheet superstructures (PTSS and CTSS) to result in the formation of vertically oriented PI nanosheet arrays periodically patterned on MoO_3 nanorods in a high-temperature solution under stirring (Fig. 7c–e) and reported that subsequent template removal and carbonization can covert PTSS to CTSS with preserved morphology (Fig. 7f). A heterogeneous nucleation and template-directed assembly mechanism was proposed for the formation of this unique 3D structure. Researchers have further reported that PI arrays can be grown on other substrates such as CNTs and graphene to form shish-kebab CNT/PI nanohybrids [115] and vertical PI nanowalls on GO [116] respectively. Moreover, PI arrays can be coated onto macroscopic substrates including CNT fibers, polymer fibers, CNT films, CC and graphene aerogels for different applications [117–120]. For example, Wei et al. [121] successfully grew vertically oriented and periodically patterned PI nanoflake arrays onto an SWCNT film through the simple introduction of the SWCNT film to initiate polymer nucleation and growth during dilute polymerization (Fig. 7g). These researchers also systematically investigated polymer concentrations and reaction time to optimize corresponding morphology and electrochemical performance and reported that an optimized SWCNT/PI film was able to maintain the flexible features of the SWCNT film and showed potential for application in wearable energy devices (Fig. 7h). Drawbacks of this SWCNT/PI film, however, include the low loading of active PI and high cost of SWCNTs.

In addition to solution-based self-assembly methods, plasma and laser treatments can directly produce 3D hierarchical carbon structures or even graphene from PI materials. For example, Endo et al. [122] fabricated vertically aligned carbon nanosheets from Kapton PI film on Cu substrate using H_2/Ar plasma irradiation in which the resulting ultrathin carbon nanosheet structure was petal-like in shape with sharp edges and consisted of few-layer graphene sheets. Besides these vertical graphene sheets, a layer of flower-like carbon with a diameter of ~ 4 μm constructed from the ultrathin carbon petals was also observed in which other than morphology, both the vertical carbon sheets and the carbon flower showed similar structural features. Tour and coworkers also used laser treatment to synthesize graphene from PI films in which these researchers were able to prepare vertically oriented porous graphene fibers from the laser-treated

PI film along with various laser-induced graphene (LIG) morphology through the control of laser energy (Fig. 7i) [123]. Here, they reported that ~ 5 J cm^{-2} was the critical point for the initiation of the carbonization process regardless of laser power but that increases in radiation energy resulted in the gradual transformation of the LIG morphology from sheets to fibers and ultimately to droplets following a fluid dynamics process. Ultimately, the use of radiation energy more than 40 J cm^{-2} during laser photo-thermolysis can give rise to vertically oriented porous graphene fibers with height up to 1 mm (Fig. 7j–l).

4.3 Polydopamine

Polydopamine (PDA) was initial discovered as a multifunctional polymer coating in 2007 and has subsequently attracted significant attention [124] due to its ability to deposit onto any substrate as a result of its unique adhesive properties based on amino and catechol functional groups. In addition, PDA can coordinate with metals through strong chelation between metal ions and polymer as well as combine with heteroatom-containing functional groups through chemical modification. And in conjunction with corresponding high carbon yields and solution processing capabilities, PDA-based nanomaterials with various components and structures can be constructed for multifunctional purposes [125]. Despite these characteristics, hierarchical PDA structures have yet to be found. On the contrary, PDA-based organic–inorganic coordination polymers have been intensively studied and can be constructed into hierarchical spheres, hierarchical nanoflowers or hierarchical hollow tubes in which the morphology of these coordination polymers is strongly associated with inorganic–organic bonding strength, reactant concentration and presence of surfactants.

And of the various PDA-based coordination polymers, Mo-PDA is among the most investigated. For example, Lou et al. [126] constructed hierarchical Mo-PDA nanotubes through Mo-PDA ultrathin nanosheets obtained using MoO_4^{2-} as the Mo source and the metal site, dopamine as the organic ligand, ammonia solution as the reaction initiator and MoO_3 as the sacrificial template (Fig. 8a). Here, TEM was used to observe the time evolution process of the Mo-PDA hybrid and revealed that pristine MoO_3 nanorods possessed a smooth surface before reaction (Fig. 8b), whereas fast-forming Mo-PDA nanosheets homogeneously coated onto MoO_3 nanorods after 0.5 min (Fig. 8c). They further reported that extending the reaction to 3 min resulted in the MoO_3 nanorods being partially dissolved to form MoO_4^{2-} accompanied by the further growth of Mo-PDA nanosheets (Fig. 8d) followed by the generation of hierarchical Mo-PDA nanotubes after the complete removal of the MoO_3 nanorods at 120 min (Fig. 8e), which can subsequently be converted into carbon coupled β-Mo_2C hierarchical nanotubes by pyrolysis. Similarly, Wang et al. [127] used $NiMoO_4$ as a template to develop a hierarchical Mo-PDA superstructure in which different from previous works presenting hierarchical nanotubes, a Ni-Mo-PDA butterfly flower was obtained. Here, the microstructures of the different stages were observed and indicated the interaction between slowly released molybdate anions from $NiMoO_4$ with dopamine was the key to form nanosheet structures on the surface of the $NiMoO_4$ nanowires. As the $NiMoO_4$ nanowires gradually dissolve, the nanowires can intersperse with the nanosheets to transform into the flower-like structure.

In another example, Huang et al. [128] prepared 3D flower-like Mo-PDA through coordinative reactions between PDA and MoO_4^{2-} and reported that the presence of MoO_4^{2-} anions and the appropriate content of Mo-to-dopamine were crucial for the formation of the flower structure in which the absence of MoO_4^{2-} resulted in the formation of only PDA spheres and the formation of the flower-like superstructure only occurred at a Mo-to-dopamine molar ratio in the range of 0.25–1.5. Corresponding time-dependent formation experiments further showed that the addition of dopamine into MoO_4^{2-} solution resulted in the colorless solution instantly turning dark red, suggesting rapid chelation between Mo and dopamine in which even after 15 s of reaction, the Mo-PDA complex can already demonstrate a micro-flower shape with a diameter of ~ 700 nm, whereas the average size of the Mo-PDA micro-flower gradually increases and reaches ~ 2.8 μm after 10 min of reaction. They further reported that extended reaction time did not enlarge flower size and suggested that PDA growth behavior was affected by MoO_4^{2-} where without interference from MoO_4^{2-}, PDA will grow isotopically to yield spheres. Alternatively and similar to the functions of a surfactant molecule, MoO_4^{2-} adsorption on PDA can induce the anisotropic growth of Mo-PDA in which interactions between MoO_4^{2-} and PDA confine polymer growth to a 2D plane so that Mo-PDA evolves into nanoflakes and eventually assembles into flowers. This Mo-PDA flower can further be carburized at high temperatures (750 °C) to result in 3D carbon-supported Mo_2C with uniformly distributed ultrasmall Mo_2C nanoparticles (~ 3 nm) throughout the entire superstructure. Chen et al. [129] further reported that low-temperature carbonization (700 °C) can convert Mo-PDA flower into MoO_2 atomic clusters with sizes less than 1 nm that are homogeneously dispersed on carbon flower. Wang et al. [130] also reported that Mo-PDA hollow flowers with tailorable interior cavity sizes can be obtained by simply altering the dopamine content as a result of hydrophilic/hydrophobic interactions in water/oil systems.

In another example, Wang et al. [131, 132] explored the formation mechanisms of Mo-PDA flowers and synthesized 3D Mo-PDA flowers with tunable petal layers and

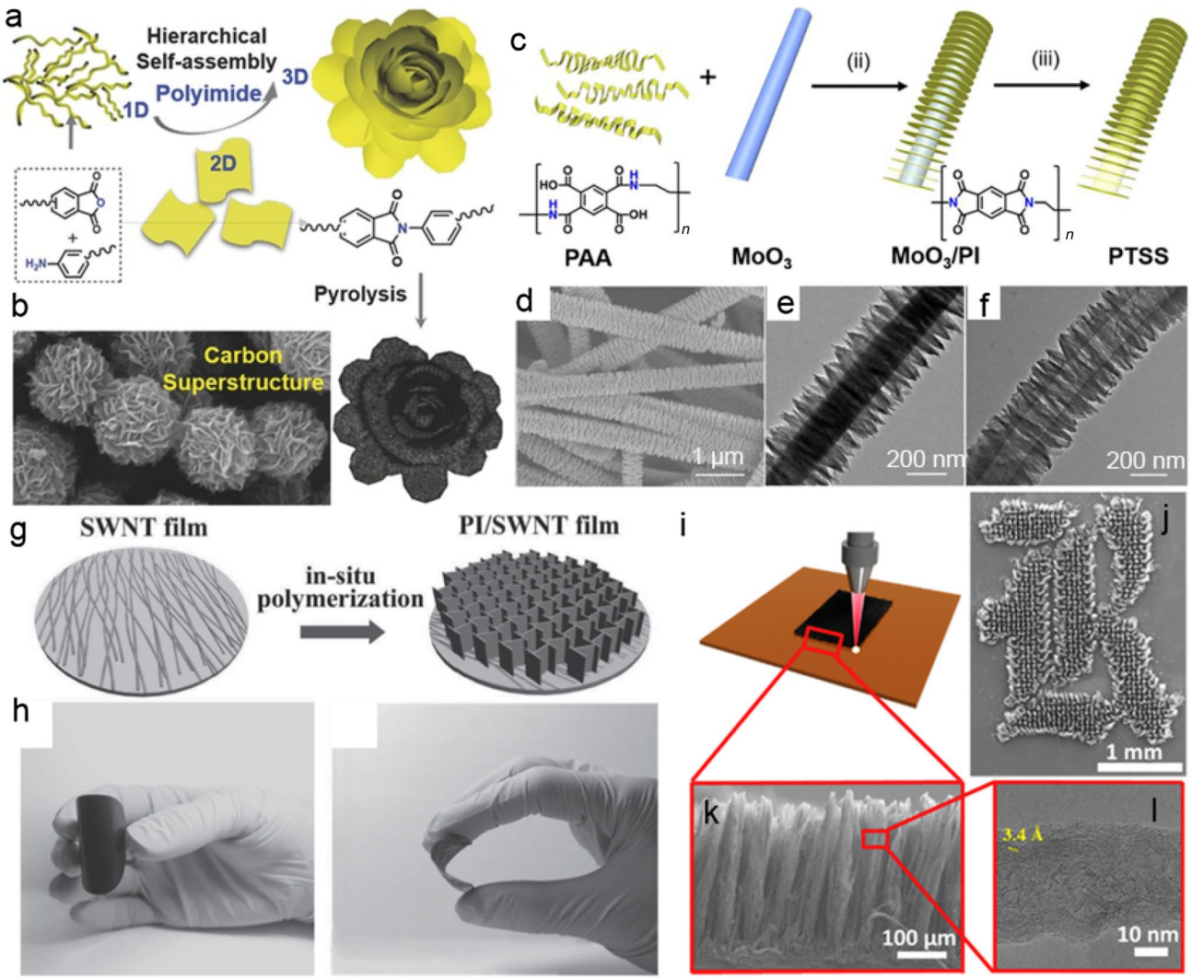

Fig. 7 Polyimide-derived 3D HCMNs. N-doped porous carbon superstructures. **a** Scheme showing the hierarchical self-assembly of PI and derived carbon superstructures. **b** SEM image of the flower-shaped carbon superstructure. Reprinted with permission from Ref. [107]. Copyright © 2016, John Wiley and Sons. Hierarchically ordered carbon tube–sheet superstructure (CTSS) derived from template-assembled PI. **c** Synthetic procedure of the CTSS. **d** SEM and **e** TEM images of a MoO_3/PI superstructure. **f** TEM image showing the hollow interior of a PI superstructure after the removal of the MoO_3 template. Reprinted with permission from Ref. [114]. Copyright © 2019, Elsevier. PI nanoflakes on the SWCNT film. **g** Preparation of a PI/SWNT composite film. **h** Photographs of the SWCNT (left) and PI/SWCNT films (right) suggesting flexible features. Reprinted with permission from Ref. [121]. Copyright © 2014, John Wiley and Sons. **i-l** Laser-induced vertical graphene nanofibers. **i** Vertical graphene nanofiber synthesis through laser treatment on a raster. **j** Low-magnified SEM image showing the "R" pattern of laser-induced graphene. **k** High-magnified SEM image displaying graphene nanofibers vertically grown on substrate. **l** Individual graphene nanofiber with an interlayer spacing of ~ 3.4 Å. Reprinted with permission from Ref. [123]. Copyright © 2017, Elsevier

2D Mo-PDA nanopetals through the introduction of stirring force and/or surfactants in previously reported synthetic conditions (Fig. 8f) [131] to report that cetyltrimethyl ammonium bromide can inhibit the interfacial assembly and stacking of petals to allow for the formation of Mo-PDA assemblies involving multilayer stacked structures, whereas the addition of sodium lauryl sulfate (SLS) as a surfactant to the system resulted in the formation of single petals. To further comprehend the formation process of Mo-PDA nanopetals and its transition from single petals to flowers, these researchers adjusted reactant concentrations and SLS amounts and found that decreasing the SLS content led to increased Mo-PDA petals being assembled into one superstructure, resulting in the proposal that the assembly of Mo-PDA petals into flowers was spontaneous due to the strong π bonding and absorption abilities of the catechol groups, and therefore, single petals can only be obtained by disturbing the assembly with the assistance of

surfactants and increased randomness. Based on all of this, these researchers concluded that the formation of Mo-PDA flowers was a result of the disordered growth of multicore structures through polymerized organic ligands to minimize energy and the tendentious symbiosis rather than the self-growth of nanopetals for structural stabilization.

Jiao et al. [133] further fabricated multilevel superstructures using W-PDA assemblies as the binder and SiO_2@C spheres as the building blocks through a cooperative assembly method (Fig. 8g–i). First, carbon-coated SiO_2 nanospheres were synthesized by co-condensation between tetraethyl orthosilicate and resorcinol–formaldehyde precursors. Following this, metal chelation reactions occurred between WO_4^{2-} and PDA in the presence of the SiO_2@C nanospheres to form layer-structured W-PDA complexes that were adsorbed onto SiO_2@C nanospheres as driven by electrostatic attraction to give rise to the initial assembly (Fig. 8g). Finally, a spherical superstructure involving W-PDA and SiO_2@C can be generated as increasing amounts of W-PDA and SiO_2@C assemblies aggregate together (Fig. 8h, i). Through subsequent pyrolysis and etching treatment, this superstructured composite can also be converted into N-doped porous carbon embedded with WM (M = O, C, P, S and Se) nanoparticles with multi-porous structures that have potential for application in energy storage and catalysis.

4.4 Other Polymers

Graphitic carbon nitride (g-C_3N_4) is a conjugated polymer composed of repeating tri-s-triazine rings in which C and N atoms are sp^2 hybridized and σ bonded to form a hexagonal ring. Since the discovery of its n-type metal-free semiconductor property with an energy gap of ~ 2.7 eV and superb photocatalytic performances for hydrogen production in 2009, g-C_3N_4 has become a hot research topic [134]. Adding to its popularity is its facile synthesis in which the simple thermal polymerization of cost-effective precursors such as urea, cyanamide, dicyandiamide, melamine or thiourea can generate g-C_3N_4 in air with high yields. Analogous to graphene, g-C_3N_4 also possesses a 2D layered structure and its products can exist in multidimensional forms ranging from 0D, 1D, 2D to 3D [15, 135].

Hierarchical mesoporous g-C_3N_4 spheres can be derived from hydrogen-bonded triazine-based molecular cooperative assemblies [136–138]. Jun et al. [136] reported that the mixing of dissolved melamine and cyanuric acid in dimethyl sulfoxide can rapidly generate solid white precipitates to give rise to melamine cyanuric acid complexes (MCA) with flower-like shapes and an average diameter of ~ 2 to 3 μm as well as a sheet thickness of ~ 30 to 50 nm, which can be successfully transformed into hierarchical hollow tri-*s*-triazine-based g-C_3N_4 spheres comprised of nanosheets through subsequent thermal polycondensation. Based on this, the same group [137] also investigated the effects of temperature, solvent and monomer on the morphology of MCA and g-C_3N_4 and reported that the transition from flower assemblies of nanosheets to urchin assemblies of nanorods can occur if precipitation temperatures increased from 30 to 150 °C. Based on hydrogen-bonded MCA complexes with rich amine and hydroxy groups that can bind to substrates, Shalom et al. [138] grew highly ordered MCA complex-derived carbon nitride nanorod arrays on various substrates including glass and fluorine-doped tin oxide (FTO) to achieve enhanced surface areas and catalytic properties. Firstly, MCA assemblies containing equal molar melamine and cyanuric acid were precipitated from water followed by the coating and sandwiching of the powdery MCA assemblies on and between desired substrates. Subsequent pyrolysis can convert the MCA powder into C_3N_4 arrays that are strongly attached to the substrates. Here, the formation of uniform and ordered C_3N_4 rod arrays can be attributed to surface-directed growth as a result of strong interactions between MCA functional groups and SiO_2/FTO substrates.

Nanoflower-like g-C_3N_4 with interconnecting nanosheets and sharp edges can also be constructed by using silica templates. For example, Zhang et al. [139] used spherical silica with well-defined vertical porous channels and a large surface area as an ideal template to adsorb cyanamide molecules and generate nanoflower-like g-C_3N_4 through thermal-induced polycondensation, resulting in g-C_3N_4 nanoflowers with large surface areas up to 160 $m^2\ g^{-1}$ that far exceeded that of bulk-g-C_3N_4 at 9 $m^2\ g^{-1}$. They also found that the synthesis of a hierarchical structure in NS-g-C_3N_4 altered corresponding optical properties to increase the bandgap from 2.67 to 2.86 eV, resulting in improved light-harvesting capabilities and enhanced charge separation, which holds great prospects in photocatalysis. To further enlarge surface areas, Zhu et al. [140] proposed a template-free approach to synthesize P-doped hollow flower-shaped g-C_3N_4 with in-plane mesopores through condensation between melamine and diphosphonic acid followed by thermal annealing in which the formation of the porous flower structure is the result of cooperative assembly between diphosphonic acid and melamine as well as the in situ generation of microemulsions that can act as pore-forming templates.

Interestingly, flower-like g-C_3N_4 can be grown onto macroscopic substrates as well. For instance, Qiao et al. [141] conduced the large-area (10 cm × 15 cm) growth of P-g-C_3N_4 nanoflowers on carbon–fiber paper (CFP, Fig. 9a–e) in which the surface of CFP was oxidized to accommodate rich oxygen-containing groups such as carboxyl groups and improve corresponding interactions with melamine. Here, hydrothermal treatment and subsequent thermal annealing were conducted to enable further acid–base interactions between ethylene diphosphonic acid and melamine in the presence

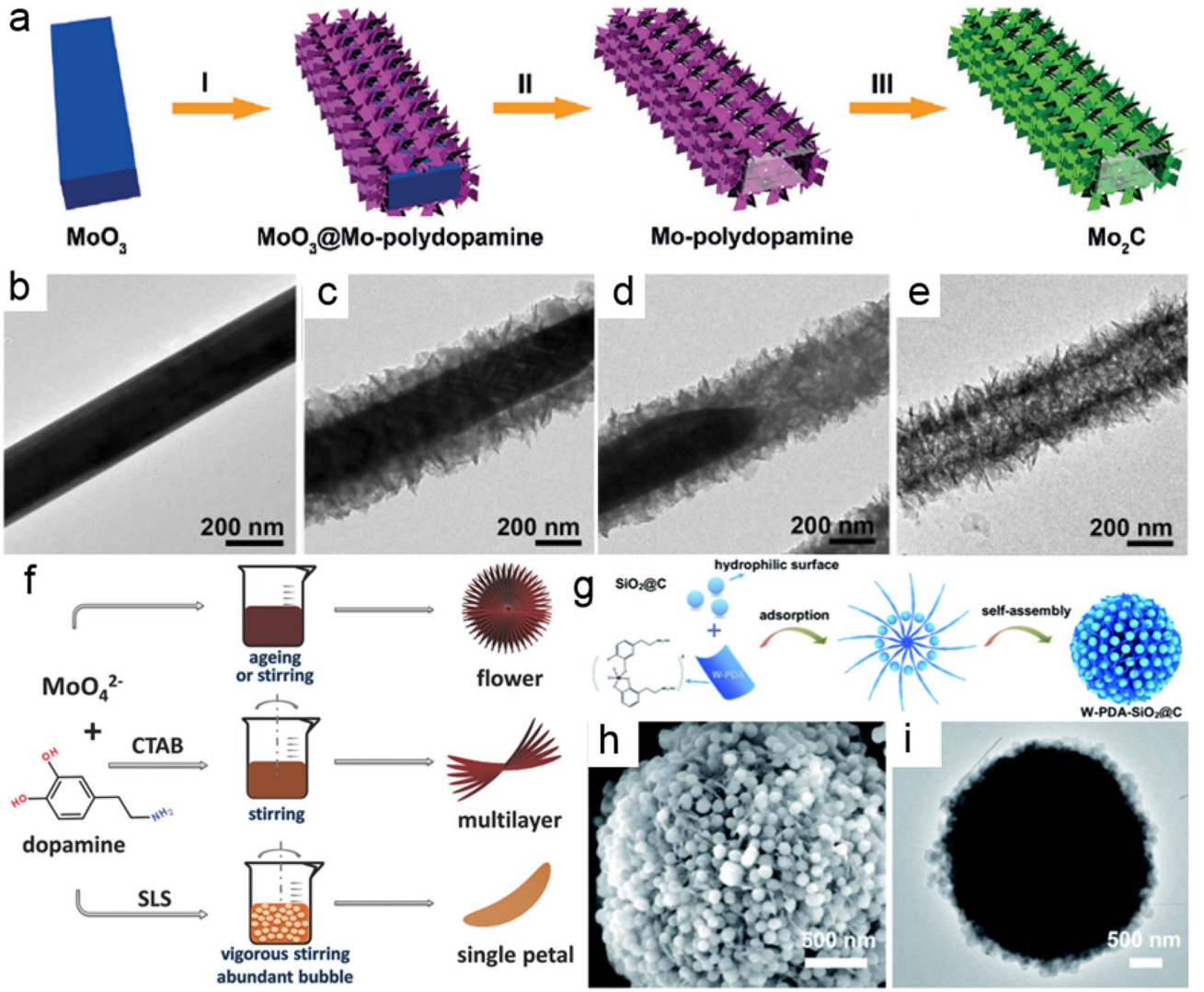

Fig. 8 Polydopamine-derived 3D HCMNs. Nanosheet-constructed hierarchical Mo-PDA hybrids and derived Mo_2C nanotubes. **a** Formation process of hierarchical Mo-PDA and Mo_2C nanotubes. Time evolution process of hierarchical Mo-PDA nanotubes. TEM images of **b** MoO_3 nanorod, **c** Mo-PDA-coated MoO_3 at 0.5 min, **d** partial dissolved MoO_3 coated with Mo-PDA at 3 min and **e** final hierarchical Mo-PDA nanotubes at 120 min. Reprinted with permission from Ref. [126]. Copyright © 2015, John Wiley and Sons. **f** Synthesis of Mo-PDA superstructures with tunable morphology including micro-flower, multilayer and single layer petals. Reprinted with permission from Ref. [131]. Copyright © 2018, John Wiley and Sons. Superstructures based on W-PDA complexes and SiO_2@C nanospheres. **g** Construction of multilevel superstructures with W-PDA complex as the binder and SiO_2@C nanospheres. **h** SEM and **i** TEM images of W-PDA-SiO_2@C showing nanosphere-constructed complex spherical superstructures. Reprinted with permission from Ref. [133]. Copyright © 2020, Royal Society of Chemistry

of CFP, which led to the adsorption of precursors and the growth of P-g-C_3N_4 nanoflowers that were strongly coupled onto the surface of CFP. SEM images revealed large-area CFP surface covered with interconnected P-g-C_3N_4 micro-flowers (size: 1–3 μm) with uniform and dense distributions (Fig. 9b-d). They also reported that the thickness of the nanosheets in the P-g-C_3N_4 micro-flowers was ~ 3 nm, which implied that the nanosheets were composed of ~ 9 atomic layers of g-C_3N_4 (Fig. 9e). Control experiments further showed the generation of bulky g-C_3N_4 particles on CFP in absence of P-based monomers, leading to their proposal that the formation of the g-C_3N_4 flowers was based on heteroatom motif-altered polymerization. In addition, Bian et al. [142] prepared carbon nitride nanotube arrays through AAO template-assisted synthesis using ethylenediamine and carbon tetrachloride as precursors accompanied by thermal treatment and template etching to result in nanotubes with an outer diameter of ~ 300 nm, a wall thickness of ~ 30 nm and an average tube length of ~ 60 μm.

3D aromatic polyazomethine (PA) can be constructed through a dynamic covalent chemistry controlled crystallization strategy [143, 144] involving the use of molecular building blocks including 1,4-terephthalaldehyde (TPA), 3,5-diamino-1,2,4-triazole (DAT) and 2-aminopyridine (AP) in which by varying the ratio of monomers in the reversible imine exchange reaction, PA microspheres with finely tunable surfaces can easily be obtained (Fig. 9f). It was found that increasing AP as a monofunctional competitor will result in the gradual transition of the surface morphology of PA spheres from smooth planes to nanoparticle-, to nanoleaf- and finally to nanofiber-like protuberances (Fig. 9g–j) and that after pyrolysis, the carbon material can retain the morphology of the polymer and result in cactus-like carbon microspheres with tunable surface roughness [144]. In another example, Chen et al. [120] proposed a general reaction induced hetero-epitaxial crystallization strategy for the construction of polymer/CNT nanohybrid shish-kebab structures in which PA and PI can be successfully patterned onto CNT surfaces and aramid fibers can present vertically oriented polymer nanosheet arrays. Higuchi et al. [145] subsequently extended this approach to achieve the epitaxial crystallization of PA into vertically standing nanowalls on the surface of highly oriented pyrolytic graphite. The formation of the vertically standing nanowalls was attributed to limited monomer supply and strong molecular π–π interaction.

Bao et al. [146] for the first time synthesized 3D polyacrylonitrile (PAN)-based polymers and derived carbon materials with highly uniform sizes and tunable superstructures including flowers, pompoms and hairy leaves by varying solvents or incorporating co-monomers during polymerization (Fig. 9k) and systematically investigated the relationship between polymer morphology and solvent characteristic through Hansen solubility parameters. Thanks to thermal stability, PANs can easily be converted into porous carbons and retain its polymer morphology after pyrolysis (Fig. 9l–n) in which the resulting carbon superstructure can exhibit high N doping (7 at%–15 at%) and controllable pores. Yan et al. [147] used a similar approach to synthesize mint leaf-like PAN through one-step precipitation polymerization and reported that after pyrolysis and activation, a 3D hierarchical carbon structure with a high surface area up to 3292.3 $m^2 g^{-1}$ can be successfully fabricated.

Cellulose stearoyl esters (CSEs) as natural polymer derivatives can be made into 3D structures as well. For example, Zhang et al. [148] were able to construct CSE flowers (diameter: 2.5–5 μm) from ordered nanopetals and reported that the formation of the flowers was influenced by the polymerization degree, molecular weight, polymer concentration and the ratio of good solvent to bad solvent. They suggested that polymer chain ordering during precipitation was the main cause for CSE flower formation in which the stacking of stearoyl side chains during crystallization formed ordered domains that can later form lamellas as a stable structure. The formed polymer nuclei can further trigger the growth of other polymer chains onto the surface to give rise to petals. Later, the same group obtained CSE flaky nanostructures through temperature-induced crystallization involving the cooling of a concentrated CSE solution to achieve either flower-like CSE particles 2–10 μm in diameter or organized CSE patterns with tunable heights on substrates including silicon wafer and glass fiber paper [149].

5 COF and MOF-Derived 3D HCMNs

5.1 COF

Covalent organic frameworks (COFs) as a class of crystalline porous polymers can enable the precise combination of molecular building blocks at the atomic level to achieve pre-designed porous frameworks [150]. And as an emerging molecular platform for the creation of organic materials, COFs hold great promise in energy, catalysis, environment, gas storage and optoelectronic applications [151]. In terms of the reticular synthesis of COFs, designable building blocks, reversible covalent chemistries and retainable geometric structures are three key aspects; however, the controlled synthesis of COF nanomaterials with desired morphology and structures remains challenging despite rapid progress in which limited numbers of well-defined COF nanomaterials have been reported with even less 3D hierarchical COFs being reported [152].

As an example, Choi et al. [153] in 2017 proposed a photochemical method to synthesize highly uniform COF-5 (UV-COF-5) with a sea urchin shape and reported that as compared with solvothermally prepared COF-5, the UV-COF-5 possessed a much higher surface area due to a hierarchical morphology the formation of which resulted from the selective growth of UV-COF-5 in the [001] crystal plane due to interlayer orbital coupling at the frontier energy region based on DFT calculations. Besides the construction of 3D COFs with enhanced surface areas, the UV-assisted synthesis was 48 times faster than conventional solvothermal methods and that this photo-assisted synthetic method with facile conditions and rapid kinetics can greatly enhance reaction efficiency to facilitate practical application. In the same year, Talyzin et al. [154] conducted the vertically oriented growth of COF-1 on GO through a molecular pillar approach (Fig. 10a) in which diboronic acid molecules were covalently grafted onto GO to serve as nucleation sites to induce the vertical growth of COF-1 (v-COF-GO), giving rise to a 3D hybrid with a forest of 3–15 nm thick COF-1 nanosheets perpendicular to GO. Without molecular grafts, however, COF growth on GO led to a coating of thick COF-1 layers

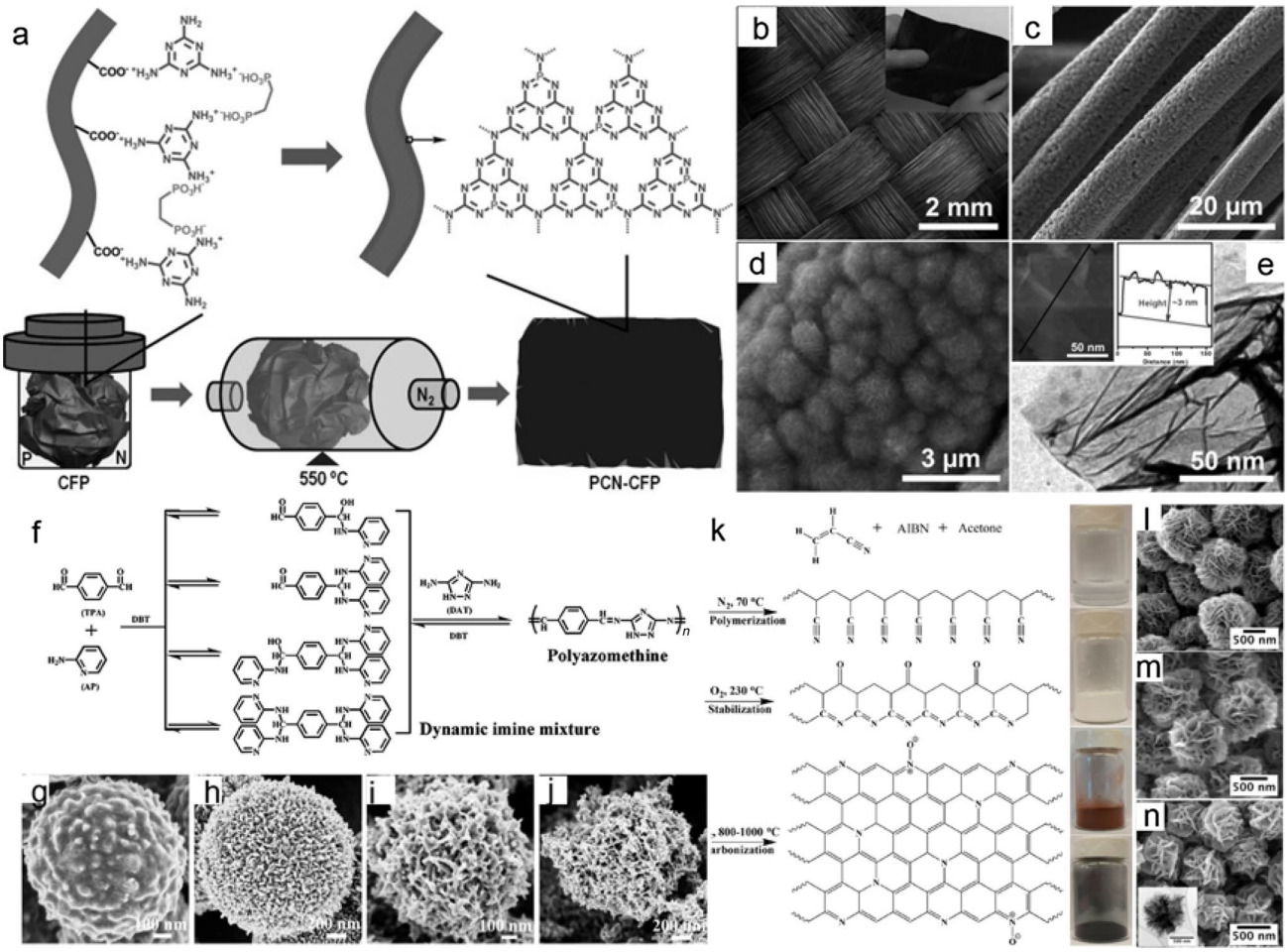

Fig. 9 Other polymer-derived 3D HCMNs. g-C_3N_4 flowers grown on carbon fiber paper. **a** Scheme illustrating the growth of P-doped g-C_3N_4 flowers on CFP. **b-d** SEM images of CFP-supported g-C_3N_4 at different magnifications. **e** TEM image of scraped g-C_3N_4 nanosheets with a thickness of ~ 3 nm. Reprinted with permission from Ref. [141]. Copyright © 2014, John Wiley and Sons. **f–j** Cactus-like PAs and derived carbon microspheres with tunable surface morphology. **f** Scheme for synthesis of PAs through dynamic imine chemistry. **g–j** SEM images of PA-derived carbon superstructures with different surface structures. Reprinted with permission from Ref. [144]. Copyright © 2014, Royal Society of Chemistry. PAN and derived carbon flowers. **k** Synthetic process and structural evolution of PAN and derived carbon. SEM images of **l** PAN flowers, **m** stabilized PAN flowers at 230 °C and **n** 1000 °C treated carbon flowers. Reprinted with permission from Ref. [146]. Copyright © 2018, American Chemical Society

parallel to GO. This molecular pillar approach is expected to be applicable in other COF systems.

Yu et al. [155] in 2018 constructed 3D porphyrin-rich COF superstructures from conjugated ultrathin nanosheets through acid-catalyzed solvothermal reactions between tetra (p-amino-phenyl) porphyrin and terephthaldehyde. The resulting 3D COF assemblies possessed a flower-like superstructure with minimal nanosheet restacking, huge surface area along with multilevel macro-meso-microporosity. COF morphology at different reaction time was tracked, and results unfold an unexpected fiber-to-sheet conversion process, in which after 3 h of reaction, the COF presented with an interconnected network composed of copious amounts of amorphous nanofibers ~ 20 nm in diameter whereas at 12 h, the COF nanofibers became rough and flake-like, which may be due to reversible imine exchange and dissolution-reconstruction. After 72 h, all the nanofibers disappeared and the smooth COF nanosheets assembled into the 3D flower superstructure as possibly caused by crystal fusion.

Very recently, Wang et al. achieved the controllable synthesis of Schiff base COF superstructures using a reversible polycondensation termination (RPT) strategy in which two monofunctional competitors (aniline and benzaldehyde) were simultaneously introduced into the condensation system (Fig. 10b). Here, these researchers reported that the monofunctional competitors can reversibly terminate/activate polycondensation reactions between monomers during synthesis by dynamically combining with monomer reactive functional groups to achieve enhanced reaction reversibility and the transition from kinetic control to

thermodynamic control [156]. Accordingly, a series of COF micro-/nanostructures have been generated, including hierarchical spheres, hierarchical tubes and hierarchical films constructed from nanoflakes (Fig. 10c–e). This approach can further enable the in situ growth of hierarchical COF films on various substrates with ordered structures up to the centimeter scale. This mechanism may also be able to explain the PA superstructures fine-tuned by monofunctional monomers as discussed in the polymer section (Fig. 9f–j). Later, the same group extended the RTP approach to design Schiff base COFs with finely controlled superstructures including core–shell, yolk-shell, hollow and multilayer yolk-shell structures with hierarchical nanosheets as the shell (Fig. 10f, g) [157]. COF shell growth on cores, either COFs or inorganic particles, can be controlled by manipulating self-coagulation and diffusion kinetics after the introduction of monofunctional competitors, whereas the selective decomposition of the amorphous COF core materials is crucial for the generation of yolk-shell and hollow structures. Based on this, the facile and template-free RPT approach is a powerful tool to obtain a variety of 3D COFs with well-defined and fine-controlled morphology that can be extended to other polycondensation systems beyond COF synthesis.

5.2 MOF

As special coordination polymers, metal–organic frameworks (MOFs) with well-defined crystalline porous framework as well as tunable organic ligands and metal species are appealing precursors and templates for creating a family of nanomaterials by cooperative assembly of metal and organic species with/without subsequent pyrolysis [158, 159]. Many MOF-derived nanostructures have excellent chemical and mechanical stability, large specific surface areas, adjustable pore structures and various functionalities [160]. Based on this, this section will discuss the synthesis of 3D MOF-derived superstructures such as urchin, flower and accordion-like MOF derivatives as well as MOF-based nanoarrays involving 1D, 2D or hybrid building blocks on various substrates.

5.2.1 MOF Superstructures with 0D Building Blocks

MOF nanocrystal-assembled hollow spherical superstructures with diameters less than 5 μm can be prepared through spray drying (Fig. 11a–c) [161], which is universally applicable to 14 commonly used MOFs, including HKUST-1, MIL-88A, MIL-88B, NOTT-100, MOF-5, MOF-14, MOF-74, ZIF-8, UiO-66, Cu(II) Prussian blue analogue and IRMOF-3, to enable the simultaneous synthesis and assembly of MOF nanoparticles into superstructures. Multicomponent superstructures and guest encapsulation can also be achieved in MOF superstructures. More impressively, MOF assemblies can be dissembled by sonication to achieve discrete and uniform nanoMOFs.

5.2.2 MOF Superstructures with 1D Building Blocks

MOF superstructures composed of 1D nanostructures have been reported by several groups. For example, Xu et al. [162] transformed Zn-MOF-74 nanoparticles (diameter: 30–50 nm) that were synthesized through the reaction between zinc acetate dihydrate and 2,5-dihydroxyterephthalic acid in methanol into chestnut-shell-like MOFs (diameter: ~ 10 μm) through a hydrothermal process using urea as a modulator in water (Fig. 11d) and reported through control experiments that the lack of urea during synthesis resulted in only small amounts of the superstructure, indicating the role of urea in the facilitation of chestnut-shell-like MOF formation. Time evolution experiments further indicated a mechanism involving the initial formation of 1D MOF nanorods followed by assembly into 3D superstructures that is similar to the hierarchical self-assembly mechanism discussed in the polymer section. The MOF superstructure can be maintained after carbonization to generate carbon superstructures composed of 1D porous carbon nanorods (diameter: ~ 40 nm; length: 2–3 μm). In another example, Chen et al. [163] converted spherical Mn-MOFs based on Mn^{2+} ions and trimesic acid linkers into hollow urchin-shaped carbon-rich superstructures through the carbonization of Mn-MOF and subsequent acid etching in which the resulting 3D hollow carbon superstructure consisted of porous nanorods with atomically dispersed Mn species. However, the superstructure formation process is not further explored in the study. Lou et al. [164] prepared the first MOF on MOF superstructure and studied its conversion into 3D carbon-based nanohybrids. In their preparation process, Fe-based MOF nanorods were initially prepared and added to another MOF precursor solution containing Zn^{2+} and 2-MIM in which during the synthesis of Zn-MOF polyhedron, the Fe-based MOF nanorods assembled onto the surface of Zn-MOF to form a nanorod-on-polyhedron dual-MOF superstructure. Subsequently, space-confined pyrolysis was carried out to transform the dual-MOF superstructure into a 3D composite involving iron carbide nanoparticle-embedded CNT assemblies on a carbon matrix. Of mentioning, MOF pyrolysis approach to prepare the CNT arrays was discussed in the CNT section.

Zhou group conducted a series of studies on MOF-74 superstructures [165–167]. Hierarchical MOF superstructures with tunable morphology were initially discovered through temperature-dependent evolution from MOF-74 crystallites to hierarchical hollow tubes, multichannel porous tubes or helical tubular structures in which the assembly of these superstructures was modulated by the decomposition of *N*,*N*-diethylformamide solvent under solvothermal conditions. They subsequently employed one-pot solvothermal

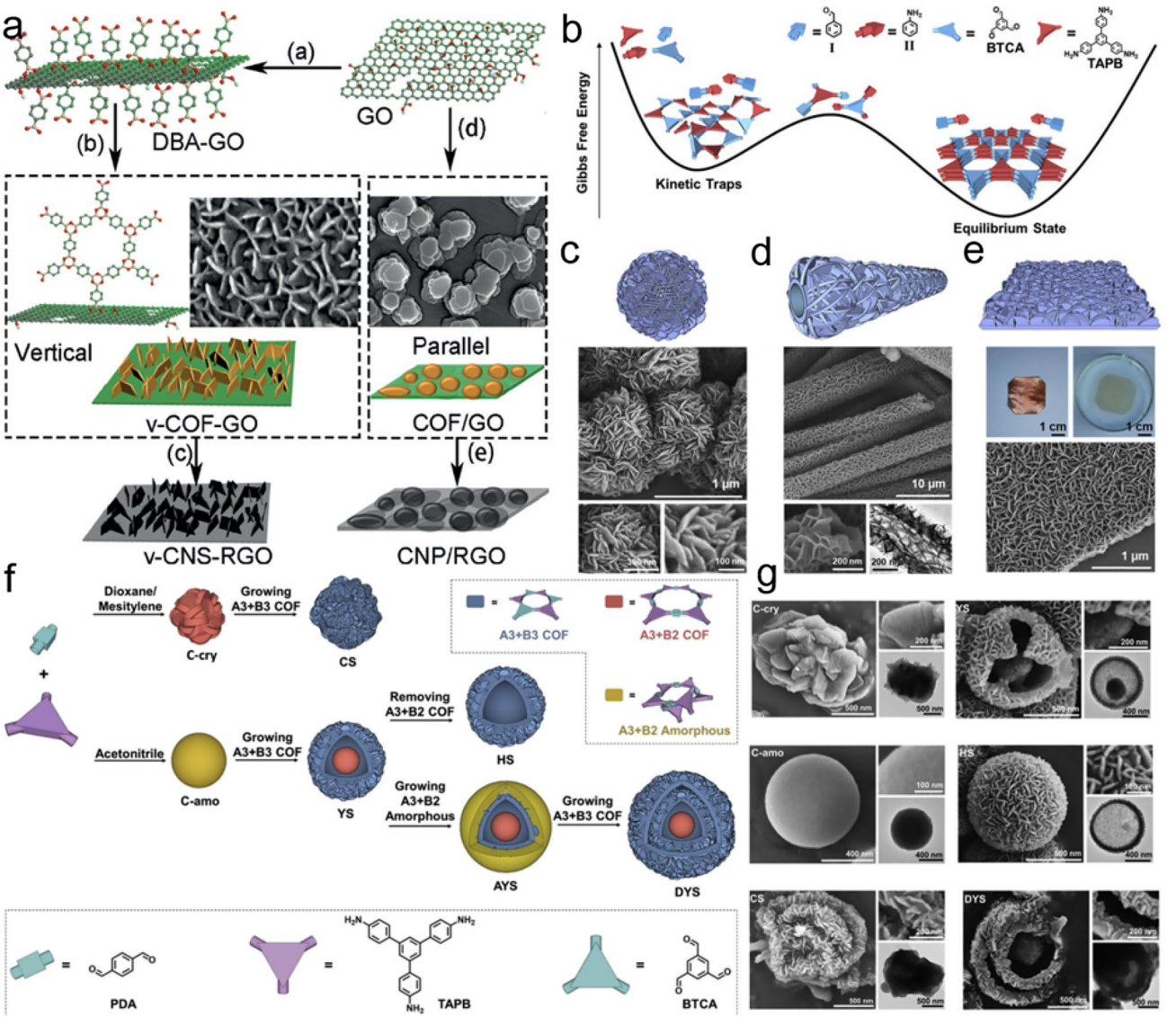

Fig. 10 COF-based 3D HCMNs. **a** Vertically oriented COF-1 nanosheets on the surface of GO (v-COF-GO) through a molecular pillar approach (left) in contrast to the parallel COF grown on GO without molecular modification (right). Reprinted with permission from Ref. [154]. Copyright © 2018, John Wiley and Sons. 3D COFs with tunable morphology (flowers, hierarchical tubes, vertical nanowalls) via reversible polycondensation termination (RPT). **b** Gibbs free energy of COF formation during RPT. Structural models and SEM images of **c** COF flowers, **d** COF hierarchical tubes and **e** vertical nanowalls on Cu foil. **e** Digital photographs showing freestanding COF vertical nanowalls exfoliated from Cu. Reprinted with permission from Ref. [156]. Copyright © 2019, Elsevier. Core–shell, yolk-shell and hollow COFs constructed by nanosheets. **f** Scheme illustration of COF morphological evolution by delicate design and its corresponding **g** FESEM and TEM images in every step. Reprinted with permission from Ref. [157]. Copyright © 2020, Elsevier

treatment to prepare MOF spherulites with a "Maltese cross" pattern which evolved from nanofibers through small-angle branching and can be finely tuned by varying the mixed solvent [166]. This method can also be extended to other MOF systems with spherulite superstructures as well as to incorporate multiple guest components into MOF superstructures. More recently, they used MOF-74-III spherulites as seeds to obtained quaternary MOF superstructures with organic linker-dependent morphology [167] in which MOF-74-III can evolve into hollow MOF-74-I assemblies through self-templated growth, eagle-like MOF-74-II superstructures through branched growth and larger sized MOF-74-III spherulites through epitaxial growth (I, II and III represent the number of benzene ring in the organic linker). Lattice mismatch and linker acidity are crucial factors affecting corresponding hierarchical superstructure evolution.

5.2.3 MOF Superstructures with 2D Building Blocks

MOF superstructures consisting of 2D building blocks have also been widely studied. For example, Zhang et al. [168] prepared hierarchical Zn/Ni-MOF-2 superstructures involving nanosheet-constructed hollow nanocubes through a solvothermal approach using 1,4-benzenedicarboxylic acid as the organic linker and Zn^{2+}, Ni^{2+} as the metallic nodes (Fig. 11e–h). The MOF structure evolved from MOF-5 nanocubes to MOF-2 nanosheets in which the nanocubes can function as in situ sacrificial templates to grow nanosheets on the exterior surface and leave a hollow interior cavity behind following the dissolution and recrystallization of inorganic nanocrystals. Similarly, Yang et al. [169] constructed MOF flowers through Zn^{2+}-assisted Ni-MOF synthesis in which the solvothermal reaction between *p*-benzenedicarboxylic acid and Ni^{2+} can generate Ni-MOF nanosheets that can transform into Zn, Ni-MOF flowers after the addition of Zn^{2+} during Ni-MOF synthesis. With the increase of Zn amount, larger sized MOF flowers could be produced, indicating the facilitator role of Zn ions. Following this, Jiao et al. [170] partially substituted Ni^{2+} in a Ni-MOF with Co^{2+} or Zn^{2+} to obtain similar flower-like superstructures whereas Xia et al. [171] carried out the solvothermal treatment of Zn/Co-MOF in the presence of Ni or Ni/Co ions to obtain hollow flower-shaped Ni-MOF and Ni/Co MOF superstructures. Li et al. [172] further obtained seashell-like Co-MOFs through a surfactant-assisted solvothermal method using cobaltous nitrate hexahydrate as the metal source and terephthalic acid as the organic ligand in which the use of polyvinylpyrrolidone as a surfactant was crucial for the formation of the MOF superstructure. Interestingly, Yan et al. [173] reported that ultrasonication treatment can transform solvothermal-synthesized Ni-MOF into accordion-like superstructures that can maintain the original crystalline structure. The layered crystal structure of the

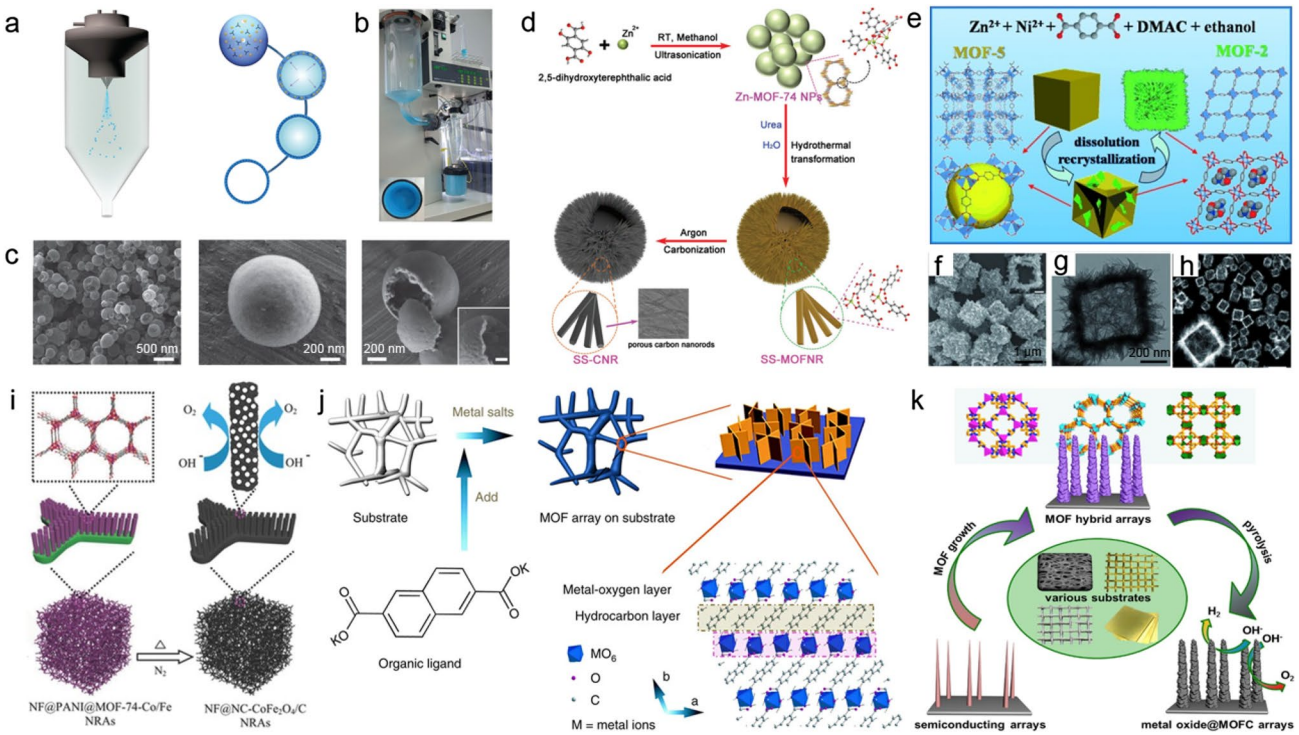

Fig. 11 MOF-derived 3D HCMNs. MOF superstructures with 0D building blocks. **a** Synthesis of HKUST-1 superstructures through spray drying and its proposed formation mechanism. **b** Photograph of the spray-dryer. **c** FESEM images of the HKUST-1 superstructure. Reprinted with permission from Ref. [161]. Copyright © 2013, Springer Nature. **d** MOF superstructure with 1D building blocks. **d** Synthesis of spherical superstructures of MOF nanorods (SS-MOFNR) and carbon nanorods (SS-CNR). Reprinted with permission from Ref. [162]. Copyright © 2019, John Wiley and Sons. MOF superstructures with 2D building blocks. **e** Preparation of hierarchical Zn/Ni-MOF-2 nanosheet-assembled hollow nanocubes and its corresponding **f** SEM image, **g** TEM image and **h** HAADF-STEM image. Reprinted with permission from Ref. [168]. Copyright © 2014, John Wiley and Sons. **i** MOF arrays with 1D building blocks. **i** Synthesis of bi-MOF-derived $CoFe_2O_4$/C porous hybrid nanorod arrays. Reprinted with permission from Ref. [179]. Copyright © 2016, John Wiley and Sons. **j** MOF arrays with 2D building blocks. **j** Fabrication of ultrathin NiFe-MOF nanosheet arrays on Ni foam. Reprinted with permission from Ref. [184]. Copyright © 2017, Springer Nature. **k** MOF-based hybrid arrays. **k** Schematic illustration showing the general preparation of metal oxide@MOF hybrid arrays and their derived metal oxide@carbon arrays on various substrates. Reprinted with permission from Ref. [191]. Copyright © 2017, Elsevier

Ni-MOF was responsible for generating the hierarchical layered morphology. Under strong ultrasonic force, Ni-MOF swelled and split into thin nanosheets, eventually forming accordions comprised of 4.1 nm-thick nanosheet.

Xu et al. [174] further obtained a MOF-derived carbon-based honeycomb superstructure consisting of ~ 10-nm-thick nanoflake cells (size: 40–100 nm), the formation of which was believed to be due to MOF internal pore expansion through internal stress as caused by gas pressure from precursor decomposition during pyrolysis. Here, the synthesis involved the uniform encapsulation of $CoCl_2$ and thiourea guests as cobalt and carbon sources into Al-MOF pores followed by carbonization to achieve guest-induced morphological control and result in a honeycomb-like porous carbon superstructure distributed with homogeneous Co_9S_8 nanoparticles. By simply changing the guests to dicyandiamide and $FeCl_3$, the same group fabricate atomically dispersed Fe–N–C species decorated on the honeycomb carbon superstructure [175]. MOF–guest pyrolysis was further demonstrated by Smoukov et al. [176] as a powerful tool to synthesize carbon-based superstructures with multiple-level hierarchy in which the inclusion of metal salts as guests into Cu-MOF and subsequent carbonization can create carbon-based nano-diatoms with two to four levels of structural hierarchy.

5.2.4 MOF Arrays with 1D Building Blocks

In terms of MOF arrays with 1D building blocks, Ma et al. [177] were able to grow Co-MOF nanowire arrays on Cu foil through the hydrothermal reaction between equal molar dipotassium 2,6-naphthalenedicarboxylate and cobalt (II) acetate tetrahydrate that can further be converted into Co_3O_4/C hybrid arrays in inert gas or carbon-free Co_3O_4 arrays in air. Similarly, Zhang et al. [178] grew Co-MOF nanowire arrays on Ni foam (NF) that possessed 6-coordinated Co centers in which each Co possessed three carboxyl groups and two hydroxy groups as double bridging through a solvothermal reaction using 2,5-dihydroxytelephthalic acid as the organic ligand. Lu et al. [179] further grew ~ 680-nm-diameter MOF-74-Co/Fe nanorod arrays on PANI-coated NF through a solvothermal reaction (Fig. 11i) and reported that PANI electrodeposited onto NF played a crucial role as a metal ion capturer and a heterogeneous nucleation site to accommodate dense MOF array growth in which without PANI, the same conditions generated only random and spare MOF-74-Co/Fe nanorods on NF. The calcination of MOF-74-Co/Fe at 600 °C in N_2 further converted it into $CoFe_2O_4$/C with the retained nanorod arrays embedded with ultrafine metal oxide nanoparticles. Recently, Zhou et al. [180] also directly grew ternary metal-based (Fe, Co, and Ni) MOF-74 nanorod arrays on the NF using a superfast microwave-assisted solvothermal approach in which the growth of the MOF nanorod arrays can be accomplished in 15 min.

Aside from direct growth using solvothermal reaction, MOF 1D arrays can also be fabricated through template-assisted methods. For example, ZnO nanorod arrays can act as sacrificial templates to fabricate MOF nanorod arrays in which Zhang et al. [181] grew vertically aligned ZnO nanorod arrays on flexible CC through chemical bath deposition in which the subsequent reaction between ZnO nanorod arrays in a mixed solvent of *N*,*N*-dimethylformamide and H_2O containing 2-methylimidazole (2-MIM) can result in ZnO@ZIF-8 nanorod arrays with 2-MIM acting as an organic ligand to coordinate with Zn ions. Zhou et al. [182] also grew cobalt carbonate hydroxide nanorod arrays on Ni foil through hydrothermal treatment as a template for growing ZIF-67 nanorod arrays in which the MOF array can further be converted to 3D Co_3O_4@X (X = Co_3O_4, CoS, C and CoP) composites after oxidation, sulfidation, carburization or phosphorization treatment.

5.2.5 MOF Arrays with 2D Building Blocks

As for MOF arrays with 2D building blocks, Fang et al. [183] were able to directly grow Co-MOF and Zn-MOF nanosheet arrays on NF through the hydrothermal reaction between metal salt and 2-MIM. Duan et al. [184] also grew NiFe-MOF nanosheet arrays on NF through the heating of a solution containing 2,6-naphthalenedicarboxylate tetrahydrate as the organic species and Ni and Fe salts as the metal nodes in a sealed vial at low temperature (60 °C, Fig. 11j). Guan et al. [185] further submersed a flexible CC substrate into an aqueous solution containing 2-MIM and cobalt nitrate to achieve the surface-growth of Co-MOF nanowall arrays at room temperature in which subsequent ion exchange using nickel nitrate in ethanol can allow for the simultaneous etching of Co-MOF to transform it into a Ni–Co layered double hydroxide with a hollow walled structure. Next pyrolysis of the layered double hydroxide in air formed hollow and porous $NiCo_2O_4$ nanowall arrays on the CC. Based on this method, researchers have subsequently grown Co-MOF nanowall arrays on various substrates for different applications [186–189] in which Guo et al. [186, 187] grew nanoarrays on electrospun PAN nanofibers followed by conversion into carbon nanowall array-supported atomically dispersed Co sites or hollow Co_3O_4 nanoparticles for oxygen electrodes in flexible Zn-air batteries (discussed in the electrocatalysis section), whereas Yu et al. [189] grew Co-MOF nanoarrays on CC followed by conversion into Co-containing carbon nanowall arrays for lithium metal batteries (discussed in the battery section).

5.2.6 MOF-Based Hybrid Arrays

MOF hybrid arrays can also be constructed by growing MOF arrays onto metal oxide or metal hydroxide nanoarrays on various substrates [190, 191]. For example, Falcaro et al. [190] heteroepitaxially grew MOF arrays onto $Cu(OH)_2$ nanoarrays in which $Cu(OH)_2$ nanotubes were first constructed on Si wafer followed by immersion in H_2BDC solution at room temperature to allow for the growth of MOF crystals in the vertical direction to the nanotube surface within 5 min. In another example, Cai et al. [191] used a general self-sacrificing templated method to grow MOF arrays on various substrates (Fig. 11k) in which metal oxide and hydroxide nanoarrays as self-sacrificing templates were first grown onto a substrate and subsequently converted into MOF arrays. These templates, including CoO, NiO and $Cu(OH)_2$ nanoarrays, grown on substrates, including Ni foam, Cu mesh, Fe mesh or Cu foil, can be successfully converted into corresponding MOFs such as ZIF-67, MOF-74 and HKUST-1 with nanorod and nanowall arrays in which the hybrid arrays can further be converted into carbon-based nanohybrid arrays.

5.2.7 MOF Arrays on Nano-substrates

MOF arrays can grow on microscopic substrates such as GO, silver nanocrystals and LDH as well [40, 192, 193]. For example, Yaghi et al. [192] grew ordered and oriented $[Al_2(OH)_2TCPP]$ MOF arrays on Ag nanocrystals in which the preparation process involved the deposition of Ag with alumina through atomic layer deposition followed by the introduction of porphyrin-based linkers to trigger MOF synthesis. Here, the thickness of the MOF layer is controllable from 10 to 50 nm through the control of alumina thickness from 0.1 to 3 nm, and the ordered and oriented MOF arrays were a result of the porphyrin units perpendicular to the Ag plane. In another example, Shao et al. [193] grew MOFs arrays onto LDH nanoplatelets to obtain a honeycomb carbon network through subsequent thermal conversion and reported that the MOF arrays were in situ homogeneously grown onto the 2D LDH nano-substrates with strong binding, which ensured controllable composition and morphology during transition from MOFs to carbon-based arrays.

6 Templated Carbon-Based 3D HCMNs

Templates are frequently used in the preparation of 3D HCMNs in previous sections. In addition, template-assisted synthesis has been widely adopted to obtain a variety of nanomaterials with different composition and morphology. In general, templates can be divided into hard templates and soft templates in which the hard template approach involves the synthesis of materials in the presence of hard templates followed by template removal to allow for the preparation of highly oriented and ordered nanostructures. Despite this, corresponding template removal processes are tedious and time-consuming and may even damage resulting nanostructures [194]. Alternatively, soft-template synthesis relies on structure-directing molecules such as surfactants and block copolymers that can be easily removed by solvents or thermal treatment. And although the soft template method is simpler and cheaper due to the lack of additional template etching procedures, resulting structures are not as well defined [194]. Based on all of this, this section will summarize the template-assisted synthesis of 3D templated carbon materials, particularly those with small molecules and biomass as the carbon source.

AAO membranes with close-packed hexagonal column arrays are ideal hard templates for the fabrication of large-area nanotube and nanowire arrays with finely tunable structural properties including length and diameter through the adjustment of AAO template thicknesses and pore diameters (AAO-templated synthesis of nanocarbons, polymers and MOFs with nanofiber/nanotube arrays was discussed in previous sections). Aside from AAO templates, other hard templates have also been proposed in the synthesis of 3D hierarchical superstructures such as ZnO flowers, ZnO nanoarrays, MgO hierarchical rods, silica urchins and salt templates. In terms of carbon sources, small molecules and biomaterials other than the above-mentioned nanocarbons and polymers can be used in the templated synthesis of 3D HCMNs. For example, Wang et al. [195] were able to use ZnO flower as the template and pitch as the carbon source to synthesize a hierarchically porous 3D carbon flower structure with large amounts of micropores and mesopores in interlinked macroporous nanowalls that was beneficial for supercapacitor applications. Yu et al. [196] subsequently infiltrated the same carbon flower structure with sulfur to prepare C/S composites for Li–S batteries. Shao et al. [197] further reported that flower-like basic magnesium carbonate microspheres can act as an effective template for carbon flower synthesis. In their synthesis process, the flower-like basic magnesium carbonate microsphere template was coated with coal pitch through solvent evaporation and subjected to carbonization, KOH activation and acidic etching to achieve a hierarchical porous carbon flower structure involving petals containing 15–24-nm nanocages and 2.5–3.0-nm-thick shells that showed high surface areas up to 1927 $m^2 g^{-1}$. Guo et al. [198] also used an urchin-like silica template with vertical pores to prepare a 3D hierarchically porous carbon flower structure (Fig. 12a) in which the simple coating of the silica template (Fig. 12b) with glucose or chitosan followed by pyrolysis with/without activation can result in ~ 200-nm-diameter porous carbon flowers assembled with ~ 4-nm-thick carbon nanosheets (Fig. 12c–e).

Through composition with graphene, more complex 3D carbon materials can be made as well [199] that can showcase multiple mesoporous channels, high surface areas and large pore volumes as promising materials for energy storage and catalysis.

Although hard templates are usually pre-made for synthesis, there are cases in which templates can be in situ generated. For example, Ding et al. [200] obtained a flower-like hierarchical mesoporous carbon superstructure through a process involving hydrothermal reaction between nickel acetate and glucose to give rise to a flower-shaped $Ni(OH)_2$/polysaccharide hybrid in which $Ni(OH)_2$ flowers were in situ generated as the template, followed by the carbonization and template-etching of the $Ni(OH)_2$/polysaccharide hybrid to result in 3D carbon superstructures constructed from ~ 20 nm thick 2D mesoporous carbon petals. Here, nickel acetate plays multiple roles, including the precursor for the in situ generation of the flower-like template, the graphitization-facilitating catalyst and the pore-forming agent. Similarly, Liang et al. [201] in situ fabricated a hollow nest-like $Ni(OH)_2$@*N*-polysaccharide template through the hydrothermal reaction between glucose, $NiSO_4$ and hexamethylenetetramine (HMT) in which glucose served as the carbon precursor, $NiSO_4$ as the structure-guiding agent and HMT as the precipitant and *N* source. Subsequent carbonization-activation-etching treatment of the polymer-coated template yielded N-doped hollow carbon nests with high surface area as well as a hierarchical porous structure composed of interconnected porous carbon sheets.

Besides templated carbon flower structures, Zheng et al. [202] conducted the $Mg(OH)_2$-templated synthesis of hierarchical porous carbon microrods (HPCMs) containing vertically oriented ultrathin nanosheets (Fig. 12f) that were able to integrate a hierarchical superstructure, vertical carbon nanosheets and multilevel pores into one structure (Fig. 12g–i), leading to ideal charge transport and ion diffusion pathways in battery electrode materials. Fellinger et al. [203] further demonstrated a salt templating-induced self-assembly approach for the synthesis of vertically grown carbon nanosheets and carbon-based composites on substrates in which the resulting vertical carbon arrays and metal carbide/carbon arrays can possess ultrathin walls, high conductivity, good adhesions, robust structures and ultrafine nanoparticles, all of which are favorable for electrochemical energy storage and conversion devices.

Vertically oriented ZnO nanoarrays are also popular in the fabrication of 3D carbon arrays on various substrates [204, 205]. For example, Fan et al. [204] fabricated self-supported 3D carbon-based hybrid arrays through sequential chemical bath deposition, electrodeposition and hydrothermal treatment (Fig. 12j–m) in which ZnO nanorod arrays deposited on Ni foil were utilized as a sacrificial template in the fabrication of core–shell Ni tube/carbon sphere hybrid arrays. Here, the self-assembly of the carbon nanospheres onto the substrates can be attributed to simultaneous ZnO etching and glucose polymerization (Fig. 12m). As for the hydrothermal treatment of glucose, polymerization and "carbonization" can occur in which during polymerization, glucose monomers can not only react with each other to form large molecular compounds containing hydroxyl and carboxyl groups through dehydration and aldol condensation, but also decompose into organic acids to result in a weak acidic solution, which allows for the simultaneous etching of ZnO microrods and retention of the electrodeposited Ni shell structure after hydrothermal treatment to result in the increase of organic compounds near the Ni shell. As for "carbonization", nucleation can occur if the organic species concentration surpasses the super-saturation point, which allows the generated nuclei to grow uniformly and isotopically to the surface of the chemical species in solution and ultimately resulting in carbon nanospheres that are attached to the Ni shells.

Biomass materials can further be used as templates in the synthesis of 3D HCMNs. For example, Xia et al. [206] carried out the dual-templated preparation of ordered mesoporous carbon nanofiber arrays using natural crab shell as the hard template and a surfactant as the soft template in which the resulting 3D HCMN was composed of mesoporous carbon nanofibers with 70 nm diameter, 11 nm mesopores and an interspacing distance of 70 nm between the nanofibers, resulting in high surface area, good electrical conductivity and an ordered porous structure that show promise for application in energy devices.

7 3D HCMNs for Energy Storage

7.1 Lithium-Ion Battery

Because of its high energy density and outstanding efficiency, lithium-ion batteries (LIBs) have become mainstream power sources for portable electronics and electric vehicles [207]. To meet the increasing demands of large-scale energy storage applications however, current LIB technologies need to improve in terms of power density, energy density, cycling stability, cost-effectiveness and safety [208, 209]. Typically, the LIBs are composed of an anode, a cathode, a separating membrane, an electrolyte to conduct ions, a current collector and packaging materials in which anode materials can be classified based on their electrochemical reaction with lithium into three groups, including intercalation/de-intercalation, alloy/de-alloy and conversion type materials [210]. Currently, most commercial LIB anodes involve graphite that possesses a low theoretical capacity of 372 mAh g^{-1} through the Li^+ intercalation/de-intercalation mechanism and is no longer sufficient. Because of this, many

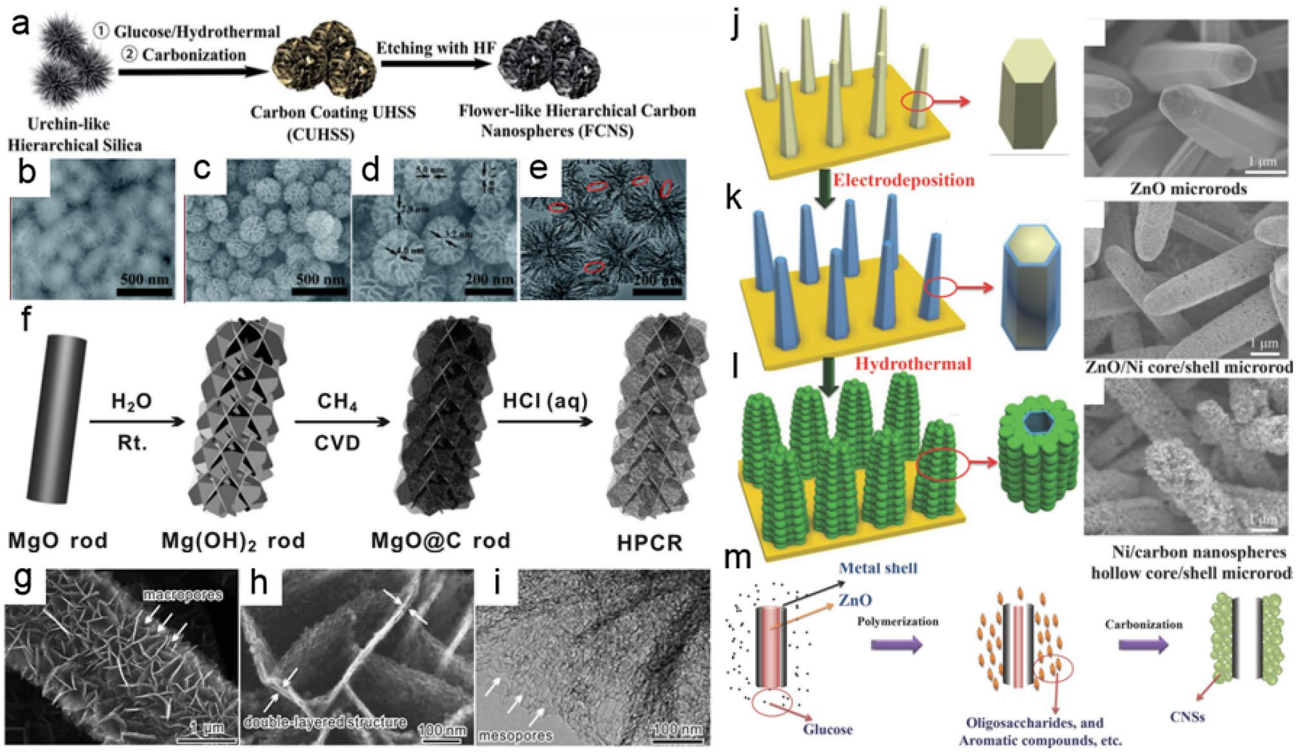

Fig. 12 Templated carbon-based 3D HCMNs. Silica-templated synthesis of highly uniform flower-like hierarchical carbon nanospheres (FCNS). **a** Schematic of the fabrication of FCNS through carbon coating on silica templates, carbonization and etching. SEM images of **b** the silica templates and **c, d** FCNS. **e** TEM image of FCNS. Reprinted with permission from Ref. [198]. Copyright © 2017, Royal Society of Chemistry. $Mg(OH)_2$ templated synthesis of hierarchical porous carbon rods (HPCRs) constructed by vertically oriented graphene-like nanosheets. **f** Synthetic process for HPCR through $Mg(OH)_2$ template synthesis, CVD growth of carbon and template removal. **g-h** SEM and **i** TEM images of the as-made HPCR. Reprinted with permission from Ref. [202]. Copyright © 2015, Royal Society of Chemistry. ZnO array-templated synthesis of self-supported metal (Ni and Co) microtube/carbon nanosphere (CNS) core/shell arrays. Schematic and SEM images of **j** ZnO microrod arrays, **k** Ni-coated ZnO microrods and **l** Ni microtube/CNS core–shell hybrids. **m** Proposed formation mechanism of the Ni microtube/CNS structure. Reprinted with permission from Ref. [204]. Copyright © 2014, John Wiley and Sons

novel carbon materials such as graphene and porous carbon have been investigated to obtain enhanced reversible capacity beyond the theoretical capacity of graphite due to additional lithium storage based on enhanced surface, pore or defect storage mechanisms [108, 211]. Alternatively, alloy/de-alloy and conversion type materials can in most cases afford much higher capacities than intercalation/de-intercalation type materials and have therefore attracted great interest as graphite alternatives [212–220]. Overall, the energy storage/release of LIBs rely on charging/discharging processes involving electrochemical reactions along with charge and mass transportation in electrodes in which Li^+ charging is based on electrons moving from the cathode to the anode and viscera for Li^+ discharging. Because of this, LIB performance is strongly associated with the structure and composition of electrode materials.

Based on this, 3D nanocarbons including CNTs, graphene and GDY have been reported as promising LIB anode materials. For example, Qu et al. [221] fabricated 3D graphene nanocapsules with surface-grown sheets (size: ca. 15 nm) through a partial peeling method and reported that the enriched edges and defects on the capsule walls and surface-grown graphene greatly enhanced lithium storage to result in an ultrahigh capacity of 1373 mAh g^{-1} at 0.5 A g^{-1}, which is more than 3 times higher than the theoretical capacity of graphite. Xiao et al. [222] also grew VG on to a current collector using CVD and reported that the vertical nanoarrays not only facilitated charge transport but also enabled binder agent and conductive agent-free electrode fabrication to substantially increase the fast-rate charging/discharging property of the optimized electrode. GDY also possesses potential as a high-performance LIB anode due to its alkyne-rich system and unique triangular pores that can present abundant Li storage sites, allowing for a theoretical capacity of 744 mAh g^{-1} that is twice that of graphite (372 mAh g^{-1}, LiC_6) [223]. Liu et al. [76] used earth-abundant diatomites as a template to construct 3D GDY superstructures as a low cost anode material (Fig. 13a), and the corresponding 3D

GDY-based LIB presented a higher specific capacity than bulk GDY powder as well as excellent rate performance and a long cycle life (Fig. 13b,c) as a result of its 3D porous structure with both intrinsic highly Li capability and accelerated Li-ion transfer. Wang et al. [224] further applied vertical GDY nanowalls as a LIB anode to achieve a high capacity of ~ 908 mAh g^{-1} and good cyclic stability.

Heteroatom doping, particularly nitrogen doping into carbon materials, can further enhance lithium storage property in corresponding anodes [225]. For example, Cao et al. [226] reported that the pyridinic nitrogen configuration was essential for capacity improvement based on first-principle calculations in which the improved lithium storage can be attributed to electronegative nitrogen that can widen interlayer distance and wettability for electrolytes to allow for rapid lithium diffusion as well as increased defects with more active sites. Despite this, the control of pyridinic nitrogen doping into 3D carbon remains difficult, and therefore, the engineering of 3D carbon with high pyridinic nitrogen doping levels and controllable assemblies for lithium storage is vital. To that end, Yang et al. [108] engineered pyridinic N-rich 3D carbon nanogears through controlled PI assembly followed by pyrolysis to obtain high-performance LIB anodes. Here, they systematically investigated the structure, composition and battery performance of the carbon nanogears synthesized at different temperatures and reported that carbon nanogears pyrolyzed at 600 °C possessed ultrahigh nitrogen doping levels (20.6 at%) and a hierarchical sheet superstructure to allow for a highly stable capacity of more than 1050 mAh g^{-1} that is approaching the theoretical value of N-doped graphene (~ 1230 mAh g^{-1}) along with exceptional rate capability and long-term cycling performance. This polymer assembly–pyrolysis strategy was further extended to other 3D carbon systems to obtain superior lithium storage [109, 111, 114]. For example, Wu et al. [114] fabricated an ordered carbon tube-sheet superstructure through the hierarchical assembly of PI nanosheets onto MoO_3 nanorods followed by etching-pyrolysis in which benefiting from the hierarchically ordered micro-/nanostructure, abundant pores and rich nitrogen doping, the 3D carbon superstructure demonstrated high capacity and cycling stability for more than 1000 cycles, which were much better than carbon disks without long-range ordered structures. In another example, Zheng et al. [202] used $Mg(OH)_2$ as a template and PDA as a N-doped carbon precursor to fabricate hierarchical porous carbon microrods with a 1D hierarchical structure and vertically aligned graphene and reported that the hierarchically porous structure allowed a corresponding 3D carbon electrode to possess high surface area, large pore volume and rapid charge diffusion pathways to result in high capacities of 1150 mAh g^{-1} at 0.1 A g^{-1}, 246 mAh g^{-1} at 10 A g^{-1} and long life cycles with 833 mAh g^{-1} after 700 cycles at 1 A g^{-1} that are superior to many carbon-based anodes. Aside from polymers, MOFs can also be used to fabricate 3D heteroatom-doped carbon anodes for LIBs [176, 227]. For example, Smoukov et al. [176] synthesized 3D carbon-based nano-diatoms with two to four levels of structural hierarchy from MOF–guest precursors to obtain a fast-charging LIB anode.

Besides serving as active materials, 3D carbon materials can also be applied as substrates to fabricate other alloy or conversion type anode materials [212]. Among them, silicon is an appealing anode material with a theoretical capacity of ~ 3590 mAh g^{-1} (based on $Li_{15}Si_4$) at room temperature. However, challenges exist for Si anodes: large volume expansion (~ 300%), low electrical conductivity and the unstable solid electrolyte interface (SEI) [216, 228] that can be alleviated through the uniform dispersion of nanostructured Si onto 3D hierarchical carbon structures. Based on this, Yushin et al. [229] proposed a scalable hierarchical bottom-up assembly strategy to prepare 3D Si/C electrodes with irregular channels for rapid ion transport and internal porosity to buffer Si volume change and achieved highly reversible capacity and stable performance. Zhang et al. [230] also designed 3D hierarchical CNT@Si@C microspheres with a highly porous structure and extraordinary mechanical strength (> 200 MPa, Fig. 13d) in which the composite electrode with a practical loading of 3 mAh cm^{-2} delivered ~ 750 mAh g^{-1} capacity with less than 20% volumetric swelling at full charge, resulting in a corresponding full cell demonstrating high capacity retention (> 92%) for over 500 cycles (Fig. 13e). Researchers have further prepared crumpled-graphene-wrapped Si nanoparticles for LIBs [47, 49] in which the highly hierarchical graphene shell can buffer the large volumetric expansion of interior Si particles during lithium storage and protect Si from SEI deposition, leading to a capacity of 940 mAh g^{-1} after 250 cycles with 83% retention, which is much better than bare Si nanoparticles with only 10% capacity retention. Apart from these carbon-based superstructures, carbon arrays including vertically aligned CNTs and graphene have also been employed as Si protectors. For example, Prashant et al. [231] synthesized vertical Si/CNT arrays on an alloy current collector using CVD and reported that the binder-free hierarchical structural design ensured that all Si/CNTs were electrically connected onto the current collector, therefore boosting mass and ion kinetics. They also reported that the CNT arrays can serve as a flexible substrate to buffer volumetric strain in which the resulting anode provided a stable capacity of ~ 2000 mAh g^{-1} with little loss after 20 cycles.

Other alloy materials including Sn, Sb, Ge and Al have also been confined inside 3D carbon structures to enhance lithium storage [232–235]. For example, Guo et al. [236] in situ synthesized a Sn@graphene nanostructure sandwiched between a vertical graphene host that can buffer critical volume change and protect Sn-NPs from agglomeration,

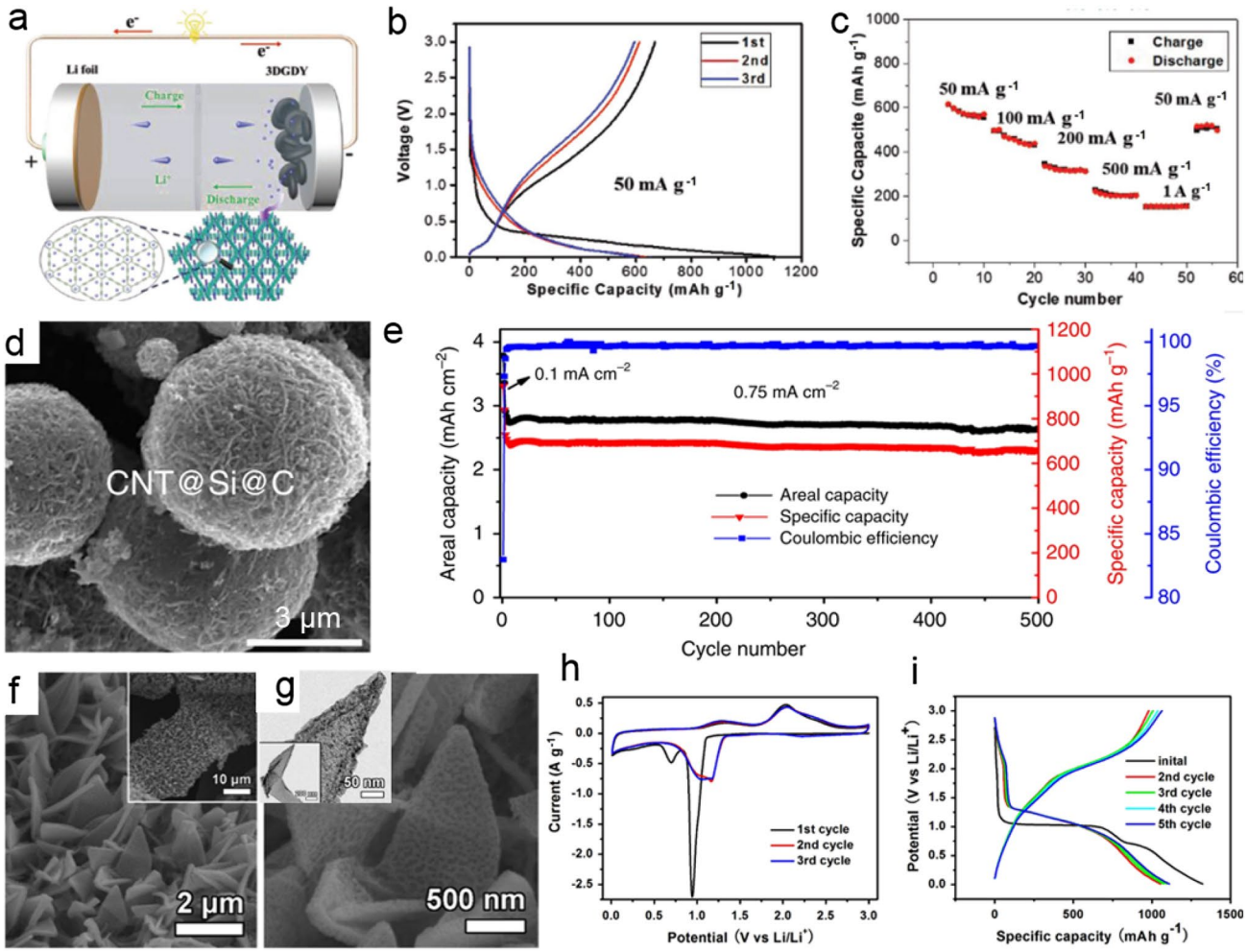

Fig. 13 3D HCMNs for LIBs. 3D GDY superstructures for LIBs. **a** Schematic of a diatomite-templated 3D GDY-assembled LIB. **b** Charge/discharge behavior and **c** rate performance of the 3D GDY superstructure. Reprinted with permission from Ref. [76]. Copyright © 2017, John Wiley and Sons. Hierarchical CNT@Si@C superstructures for LIBs. **d** SEM image of the CNT@Si@C microspheres. **e** Cycling performance of the 3D CNT@Si@C at 0.75 mA cm^{-2}. Reprinted with permission from Ref. [230]. Copyright © 2020, Springer Nature. Vertical carbon nanosheet arrays embedded with metal oxide as a self-supporting anode for LIBs. **f**, **g** SEM images of the 3D Co_3O_4/NF. **h** Initial three CV curves and **i** five charge/discharge profiles of 3D Co_3O_4/NF. Reprinted with permission from Ref. [183]. Copyright © 2016, Elsevier

and the resulting 3D Sn/Graphene@VG exhibited an exceeding-theoretical capacity of 1037 mAh g^{-1} after long-term cycling. 3D carbon structures have also been employed to support conversion type electrode materials such as ZnO, TiO_2, MoO_2, SnO_2, Co_3O_4, Fe_3O_4, MoS_2, MoC_x and WC_x [44, 129, 131, 132, 181, 183, 203, 237–241]. For instance, Liang et al. [183] fabricated an advanced LIB anode based on porous carbon and transition metal oxides derived from MOF arrays (Fig. 13f, g) in which the combination of merits from porous nanosheets, vertical arrays and conductive substrates allowed the 3D Co_3O_4/NF hybrid to exhibit long-term cycling capabilities for 2000 cycles at both 5 A g^{-1} and 20 A g^{-1} as well as rapid charging at 25 A g^{-1} (Fig. 13h, i). In another example, Zhu et al. [203] carried out the salt-template synthesis of N-doped graphene nanosheet arrays as a LIB anode in which the vertically aligned carbon nanosheets decorated with metal carbides exhibited ultrathin walls, ultrasmall nanoparticles, good conductivity and strong adhesion to provide efficient mass transport in LIBs. Hierarchical polymers and MOFs without carbonization can be adopted as LIB anodes as well [113, 172, 180, 242–246]. For example, Zhang et al. [113] fabricated a hierarchical multi-carbonyl PI with a 3D spherulite-like structure as a LIB anode and reported that the ordered packing of the 2D nanosheets into the 3D spherulite superstructure can enhance interfacial energy storage to achieve high capacity, resulting in the 3D PI delivering a high reversible capacity of 1343.8 mAh g^{-1} at 100 mA g^{-1}, good rate capability of 208.9 mAh g^{-1} at 1.5 A g^{-1} and excellent cycling performances with 665.1 mAh g^{-1} retained at 250 mA g^{-1} after 50 cycles.

Alternatively, researchers have developed aqueous rechargeable LIBs to address the safety concerns of energy storage systems. And although the use of water as an electrolyte can enhance safety, corresponding battery energy density is compromised due to a limited operating window (theoretical: ~ 1.23 V) [247]. Because of this, the development of high-voltage aqueous batteries is imperative to ensure competitiveness against non-aqueous LIBs. Here, Zheng et al. [117] reported that PI can passivate hydrogen evolution reactions in water and can therefore expand the operating voltage window of aqueous LIBs. Based on this, these researchers synthesized vertically oriented PI nanosheet arrays on a CNT network and achieved an HER activation barrier of 2.11 eV that was indicative of sluggish HER activity, resulting in a half-cell demonstrating a high capacity of 153.7 mAh g^{-1} and ultrafast rate capability. Full cells based on the PI anode and a $LiMn_2O_4$ cathode were able to deliver a voltage of ~ 2.0 V with a high energy density of 76.1 Wh kg^{-1} as well as a power density of 12.61 kW kg^{-1} and remarkable cycling stability with a capacity retention of 65.5% after 1000 cycles at a high rate.

Hu et al. [246] investigated the Li storage mechanism of a 3D Co-MOF in which soft X-ray spectroscopy and solid-state nuclear magnetic resonance characterizations showed the intercalation/de-intercalation of Li^+ from carboxyl and phenyl groups in MOFs along with the deformation of CoO_6 octahedral sites. And based on this organic ligand-dominated mechanism, the 3D seashell-like Co-MOF anode provided a high initial coulombic efficiency (CE) of 80.4% and extraordinary cyclic stability with a retained capacity of 435 mAh g^{-1} after one thousand cycles at 1 A g^{-1}. Li et al. [180] further combined multicomponent MOF-74 composed of Fe, Co and Ni with low-temperature heating to design 3D nanorod arrays on Ni foam as efficient lithium anodes using a facile microwave-assisted solvothermal method. The MOF-74 arrays possessed an ordered nanostructure, enhanced conductivity from multiple components, shortened ion diffusion pathways and sufficient spacing to buffer electrode swelling, making it ideal for lithium storage and allowing for a reversible capacity of 834 mAh g^{-1} at 50 mA g^{-1} and 93% capacity retention after 500 cycles at 1 A g^{-1}, which are among the best performance in reported MOF and MOF-derived electrode materials.

7.2 Li Metal-Based Batteries

7.2.1 Li-Organic Battery

Sustainable growth requires the development of next-generation battery materials that are inexpensive, environmentally friendly, flexible and sustainable, all of which cannot be satisfied by commercially available inorganic cathode materials for LIBs such as $LiFePO_4$, $LiCoO_2$ and $LiMn_2O_4$ due to limited natural resources as well as limited capacities and energy densities [248]. Alternatively, organic materials such as conducting polymers, organic sulfur-based, azo-based, heterocyclic-based, organic radical-based and carbonyl-based compounds have emerged as promising electrodes for LIBs [249–251]. In particular, carbonyl organic electrodes can exhibit stable electrochemical reaction mechanisms and possess great potential as next-generation electrode materials [252] with corresponding reaction mechanisms involving nucleophilic addition that relies on reversible transition between carbonyl and enolized structures in which during discharge, a carbonyl group accepts one electron from the anode to the cathode to form a negative $C–O^-$ ion that can form C–O–Li bonds with lithium ions in the electrolyte to electrically neutralize the system [249]. Like most organic materials however, obstacles exist for carbonyl organic-based electrodes such as dissolution in electrolyte, poor electrical conductivity and low active carbonyl group utilization. To tackle these obstacles, three major strategies have been developed, including the polymerization of small molecules to minimize the solubility of carbonyl organics, the coupling of carbonyl organics with conductive carbon materials and the construction of highly exposed nanostructures. For example, Song et al. [253] demonstrated the first use of PI as a cathode in rechargeable lithium batteries and further obtained 3D PI/graphene nanocomposites through the in situ polymerization of PI in the presence of graphene sheets to enhance Li storage [254] in which nanoflower-like PI were uniformly coated onto few-layered graphene sheet surfaces through non-covalent interactions between graphene and polymer. Here, the highly dispersed graphene sheets in the composite significantly improved the electronic conductivity of PI and resulted in the efficient utilization of redox-active carbonyl groups in PI. As a result, the 3D PI/graphene nanocomposite delivered superior charging/discharging properties as compared with the pure polymer. These researchers also applied this strategy to construct 3D nanowall-shaped poly(anthraquinonyl sulfide) as another carbonyl organic polymer onto graphene for enhanced LIB performance. Similar approaches were also employed by Wei et al. [116, 255] to construct 3D PI-based LIB flexible cathodes including a PI/SWNT film electrode and a 3D PI/graphene foam electrode in which in both cases, vertical PI nanosheet arrays were aligned onto carbon substrates to fully expose redox sites, resulting in the binder-free PI/SWNT film electrode delivering a capacity of 226 mAh g^{-1} at 0.1 C that was much better than pure PI with a capacity of 170 mAh g^{-1}. Rate performances at 20 C were also significantly improved from almost zero capacity for a pure PI electrode to 120 mAh g^{-1} for the PI/SWNT film electrode.

Very recently, 3D PI micro/nanostructures without carbon matrixes have been constructed for Li-organic batteries [256, 257]. For example, Yu et al. [257] prepared a 3D rose-like nanoporous polymer containing both imide and anthraquinone groups (Fig. 14a–c) and reported that the anisotropic

growth of nanosized rose flakes resulted in a large specific surface area of 116.95 $m^2 g^{-1}$ and an abundant pore structure of 0.2428 $cm^3 g^{-1}$ that can shorten lithium-ion diffusion pathways, reduce material solubility and expose active carbonyl groups. Corresponding cyclic voltammogram (CV) (Fig. 14b) and galvanostatic charge/discharge (GCD) testing of the PI cathode in a Li-organic battery showed several redox peaks during cycling in which the first cycle was attributed to the activation process whereas the subsequent cycles gradually overlapped, indicating the reversible Li storage capability of this polymer. The redox peak voltages at 2.36/2.68 V and 2.24/2.47 V can be assigned to quinone carbonyl group redox reactions, whereas the reduction peaks at 2.0 V and 1.86 V and the oxidation peaks at 2.0 V, 2.14 V and 2.34 V can be attributed to the imide carbon group, indicating a highly reversible 4-electron enolization reaction for lithium storage. Furthermore, the voltage platform gradually decreased/increased and showed a mid-point discharge potential of 2.2 V and charge potential of 2.3 V, respectively, during discharging/charging (Fig. 14c). These researchers further reported that the capacities of the PI cathode can reach 228 mAh g^{-1} (the 1st cycle) and 103 mAh g^{-1} (the 1000th cycle) at 50 mA g^{-1} with a low capacity decay rate of only 0.05% per cycle at 200 mA g^{-1} for over 1000 cycles at a loading of 1 mg cm^{-2}. At a higher loading of 3 mg cm^{-2}, the capacity after 500 cycles still reached 123 mAh g^{-1} accompanied by high CE of 99% in which the polymeric structure during lithiation based on DFT calculations indicated the formation of robust bridge bonds that can promote electrochemical activity during charge/discharge.

In general, carbonyl-rich polymers, especially PI electrode materials possess: (1) intrinsic stability and poor solubility in electrolyte to ensure long-term cyclability; (2) enhanced safety due to excellent thermal stability and nonflammability; (3) environmental benignity due to the hydrolysable characteristic of PI under alkaline conditions; (4) relatively high working voltages (2.0–2.5 V), capacities and energy densities; (5) tunable electrochemical properties through the altering of molecular structure and (6) feasibility for industrial-scale synthesis due to facile and inexpensive preparation processes. Other than use in lithium-based batteries, PIs can also find use in other batteries, including sodium, potassium, magnesium and calcium-based batteries as well as aqueous batteries [117, 258–263].

7.2.2 Li–S Battery

Like carbonyl organic electrodes, sulfur is a promising cathode for LIBs due to a ultrahigh theoretical capacity (1675 mAh g^{-1}), earth abundance and low cost. However, the practical use of Li–S batteries faces severe problems such as the low conductivity of sulfur, the polysulfide shuttling effect and the slow kinetics of sulfide redox reactions, all of which result in low sulfur utilization and rapid performance decay [264]. Here, the design of suitable hosts that can boost electron/ion transport and confine polysulfides can significantly enhance the performance of Li–S batteries. And since the report on the encapsulation of sulfur inside mesoporous carbon materials [265], the rational design of carbon structures to host sulfur continues to receive tremendous attention [266]. For example, deriving from a Pickering emulsion containing silica, melamine, and CO_2, Li et al. [267] synthesized hollow N-doped carbon materials with porous shells as a S host and reported that the corresponding Li–S battery exhibited high rate capabilities up to 9 C and long-term cycling that were much better than batteries based on commercial Ketjen black carbon.

The past decade has witnessed the rapid development of various 3D carbon-based hosts for Li–S batteries. For example, Zhang et al. [268] assembled a flower-like 3D superstructure with 2D nanosheets with built-in 0D hollow graphene nanoshells as a highly efficient sulfur host and the 3D carbon structure demonstrated high capacity with good cyclability and superior rate performance in Li–S batteries. Guo et al. [198] also fabricated highly uniform 3D flower-like hierarchical carbon nanospheres (FCNS) using a template-assisted method. The resulting 200 nm 3D FCNSs constructed from 4-nm-thick carbon nanosheets with many mesoporous channels gave rise to a high specific surface area of 1151 $m^2 g^{-1}$ and a large pore volume of 1.95 $cm^3 g^{-1}$. And because of the synergistic structural features, a FCNS/S hybrid cathode encapsulating 81 wt% S delivered large capacities and long life cycles. Further ammonia treatment also resulted in N-doped FCNSs that provided an enhanced rate capability of 830 mAh g^{-1} at 5 C and cycling stability with 0.03% loss per cycle for over 200 cycles at 1 C. Moreover, the N-doped FCNSs maintained good cyclability with 0.056% decay per cycle for 200 cycles even at an increased areal loading of 2.5 mg S per cm^2.

Aside from flower-like carbon structures [196, 269], other 3D carbon structures including hierarchical tubular structures and vertical arrays have also been explored as potential sulfur hosts. For example, Zheng et al. [270] constructed hierarchical porous carbon rods from vertically oriented porous and ultrathin carbon nanosheets in which with a high specific surface area, large pore volume, hierarchical porous structure and ideal ion transfer pathways, the C/S composite (78.9 wt% S) provided a fast-rate Li storage capacity of 646 mAh g^{-1} at 5 C and good cycle life with a capacity retention of 700 mAh g^{-1} after 300 cycles at 1 C. More impressive, this 3D C/S composite at a higher sulfur loading of 88.8 wt% was still able to give an excellent rate capability of 545 mAh g^{-1} sulfur at 3 C and long-term cycling with capacity retention of 632 mAh g^{-1} sulfur after 200 cycles at 1 C. Yang et al. [271] also constructed vertically aligned sulfur–graphene (S-G) nanowalls on current collectors for

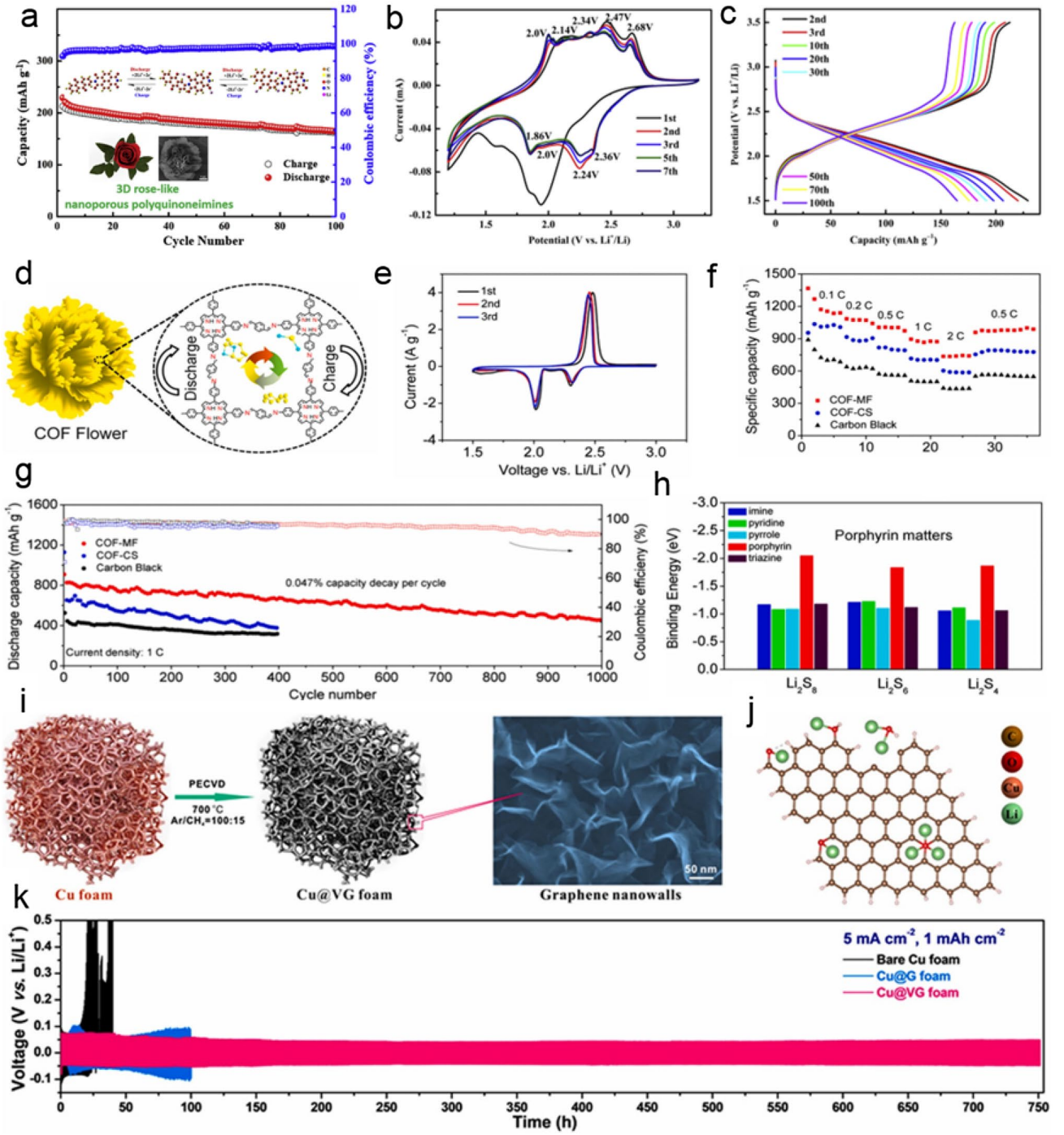

Fig. 14 3D HCMNs for lithium metal-based batteries. Rose-like PI for Li-organic batteries. **a** Cycling performance, **b** CV curves and **c** charge/discharge curves at different cycles of a PI cathode. Inset of **a** shows the rose-like morphology and Li storage mechanism of PI. Reprinted with permission from Ref. [257]. Copyright © 2019, Elsevier. COF flower for Li–S batteries. **d** Schematic of COF-MF. **e** DFT calculated binding energy of Li_2S_8, Li_2S_6 and Li_2S_4 molecules on different functional groups including imine, pyridine, pyrrole, porphyrin and triazine. **f** First three CV curves of the COF-MF@S-60% cathode. **g** Rate capability. **h** Cycling performance. Reprinted with permission from Ref. [155]. Copyright © 2018, Elsevier. Cu foam-supported vertical graphene nanowalls as a 3D host for lithium metal batteries. **i** PECVD growth of VG on Cu and corresponding morphology. **j** Schematic of the adsorption of lithium on oxygen-containing graphene. **k** Cycling performance of symmetric cells based on Cu@Li, Cu@G@Li and Cu@VG@Li electrodes tested at 5 mA cm^{-2} and 1 mA cm^{-2}. Reprinted with permission from Ref. [280]. Copyright © 2019, Elsevier

Li–S batteries in which sulfur nanoparticles were uniformly immobilized and structurally confined between graphene layers in the nanowalls that were vertically standing on the substrate to result in enhanced kinetics during cycling and efficient buffering of sulfur expansion/contraction. Correspondingly, the S-G nanowalls demonstrated a reversible capacity of up to 1261 mAh g^{-1} in the first cycle, more than 1210 mAh g^{-1} after 120 cycles and over 400 mAh g^{-1} at a high current rate of 13.36 A g^{-1}, which remains one of best rate performances reported for S/G cathodes.

Compared with pure carbon materials, carbon-based nanohybrids can potentially be more promising sulfur hosts for advanced Li–S batteries due to synergistic effects from physical confinement, chemical adsorption and polysulfide catalyzation [272–276]. For example, Qian et al. [275] rationally designed and delicately fabricated hollow superstructures involving CNT-coated Co_9S_8 with double shells (Co_9S_8@CNTs) in which each Co_9S_8 shell is sandwiched between two CNT layers to result in two CNT@Co_9S_8@CNTs sandwiches in total being carefully created. Here, these researchers reported that the CNT layers in this fully integrated superstructure can provide exceptional electrical conductivity and intimate interfacial contact between CNTs and the Co_9S_8 as well as the electrode and the current collector in which the Co_9S_8 layers with multiple metal valence states can strongly adsorb polysulfides and efficiently catalyze polysulfide conversion, whereas the multi-porous feature can accelerate charge diffusion and accommodate volume variation, resulting in the S-loaded Co_9S_8@CNTs electrode at 0.2 C providing high capacities up to 1415 mAh g^{-1} that approach the theoretical value of sulfur. Remarkably, this electrode also demonstrated optimal rate performances in literature with an ultrahigh capacity of 676.7 mAh g^{-1} at 10 C as well as ~ 100% CE and superb cycling stability (0.0448% decay per cycle over 1000 cycles).

3D HCMNs without good electrical conductivity but polar functional groups can also act as efficient sulfur hosts. For example, Yu et al. [155] constructed a 3D porphyrin-based COF superstructure with a micro-flower morphology (COF-MF) from ultrathin nanosheets as a S host (Fig. 14d), assembled Li–S batteries after 60 wt% S loading into the COF-MF@S-60% composite and conducted CV and GCD tests. Control samples including carbon black (CB) and bulk COF were synthesized in a conventional manner (COF-CS) and loaded with the same amount of sulfur for comparison. CV profiles of the COF-MF@S in the first three cycles showed typical redox peaks in the Li–S batteries (Fig. 14e). Cathodic peaks emerged at ~ 2.30 V and ~ 2.02 V in which the former peak corresponded to the reduction of S to soluble Li_2S_n ($4 \leqslant n \leqslant 8$), whereas the latter peak corresponded to further reduction to insoluble Li_2S_2 or Li_2S. Alternatively, the oxidation reactions of sulfur contributed to an anodic peak at ~ 2.45 V, whereas well-overlapped curves indicated the excellent reversibility of the COF-MF@S. In terms of rate performances (Fig. 14f), these researchers reported that sequential increases in charge/discharge rates from 0.1, 0.2, 0.5, 1 to 2 C (1.0 C = 1675 mA g^{-1}) resulted in respective capacities of 1366, 1083, 1004, 895 and 743 mAh g^{-1} that were better than those of COF-CS@S and CB@S cathodes. Moreover, the capacity of the COF-MF@S can be restored to 965 mAh g^{-1} after decreasing the current back to 0.5 C, suggesting superb reversibility. The COF-MF@S further showcased excellent cycling stability with a small capacity decay of 0.047% per cycle over 1000 cycles at 1 C (Fig. 14g). To better understand the sulfur-hosting property of the COF-MF, they further conducted DFT calculations to investigate the interactions between Li_2S_n ($n = 4$, 6, 8) and different N species, including porphyrin, imine, pyridine, pyrrole and triazine (Fig. 14h) and reported that the binding energy of Li_2S_4, Li_2S_6 and Li_2S_8 on porphyrin was − 1.86, − 1.83 and − 2.05 eV respectively, which was much larger than that of other N species, suggesting stronger chemical binding between porphyrin and polysulfides and the inhibition of polysulfide shuttling by porphyrin through strong chemisorption, possibly due to the four-coordinated configuration in porphyrin as opposed to one N atom being coordinated with Li in other N species. Based on all of this, the extraordinary battery performances of COF-MF@S can be attributed to the full exposure of abundant porphyrin groups to allow for maximum polysulfide chemisorption and sulfur utilization as a result of the construction of a flower-like COF superstructure with intrinsically rich pores, hierarchical porous structure and large surface area.

7.2.3 Lithium Metal Anode

The commercialization of Li-organic and Li–S batteries faces challenges not only from cathodes but also from the use of lithium metal in battery anodes. And although Li metal anodes are considered to be the "holy grail" anode for next-generation rechargeable batteries due to an optimal theoretical capacity of 3860 $mAhg^{-1}$ and an electrochemical potential of − 3.04 V versus SHE [277], corresponding lithium metal batteries experience significant safety concerns and poor cycling stability due to dendritic lithium growth and low CE. To address these issues, many approaches have been proposed to suppress Li dendrite growth and improve cycling stability, including modifications to electrolytes, electrodes and separators [278]. Among these, the design of suitable Li hosts that can combine excellent conductivity with unique nano-architectures and superb lithiophilic characteristics is considered to be particularly promising in the alleviation of lithium dendrite issues.

For example, Liu et al. [279] reported that hierarchical crumpled graphene balls can function as effective scaffolds in lithium metal anodes in which due to their aggregation-resistant feature, hierarchical graphene balls can be processed into a densely packed and interconnected film electrode with homogeneous thickness and abundant pores. Hierarchical graphene balls are also lithophilic in nature and can allow for the regulation of lithium crystal nucleation and growth. And as a result of these features, lithium loadings up to 10 mAh cm^{-2} can be easily accommodated with tolerable volume variation and high CE of 97.5% can be maintained for over 1500 h, enabling the plating and stripping of lithium onto corresponding hierarchical graphene-assembled electrodes up to 12 mAh cm^{-2} capacity without noticeable dendrite formation.

Yan et al. [280] also used VG-coated copper foam (Cu@VG) as a highly lithiophilic 3D host to manipulate Li nucleation and inhibit dendrite growth (Fig. 14i–k) in which the freestanding binder-free Cu@VG host possessed superb flexibility, large exposed surface and numerous lithiophilic sites such as structural defects and O-containing groups (Fig. 14j) to enable dendrite-free lithium plating, high CE > 99.0% and outstanding stability up to 750 h even at a large rate of 5 mA cm^{-2} (Fig. 14k) that are much better than unmodified Cu foam and Cu foam with horizontal graphene layers. A full cell based on the lithium deposited Cu@VG as an anode and $LiNi_{0.5}Co_{0.2}Mn_{0.3}O_2$ as a cathode further delivered improved rate capability and longer cycle lifespans as compared with pristine lithium metal-based full cells.

Liu et al. [281] further reported that CNT arrays supported by CC (CC/CNT) are stable hosts for lithium metal in which after modification with CNT arrays, the CC substrate can transition from a lithiophobic surface to a lithiophilic surface to enable the easy infiltration of melted lithium into the 3D carbon framework to prepare CC/CNT@Li composite electrodes. These researchers also reported that the high electrical conductivity of the CNTs can reduce electrode polarization, and the ultrasmall CNTs with embedded metal nanoparticles can provide heterogeneous nucleation sites for lithium deposition, whereas the uniformly distributed CNT arrays can ensure homogeneous lithium nucleation and growth during plating and the abundant porous structure involving intercrossed arrays can accommodate volumetric expansion/contraction, all of which can contribute to dendrite-free lithium metal batteries with good cycling stability of more than 500 h with low voltage hysteresis of 18 mV at 1 mA cm^{-2}, 23 mV at 2 mA cm^{-2} and 71 mV at 5 mA cm^{-2}. Alternatively, based on MOF nanoarrays, Qian et al. [282] integrated the merits of 1D and 2D building blocks into a 3D architecture to prepare N/O dual-doped 3D carbon on Cu foam (NOCA@CF) as a dendrite-free lithium metal anode in which the resulting 3D structure showed good hydrophilicity and lithiophilicity as well as rich active sites for heterogeneous Li nucleation and superb electronic conductivity and mechanical strength. As a result, full cells based on Li deposited NOCA@CF as the anode and $LiNi_{0.5}Mn_{1.5}O_4$ or $LiNi_{0.8}Co_{0.1}Mn_{0.1}O_2$ as the cathode provided remarkable long-term cycling performance with high capacity and fast-rate capability.

Apart from 3D carbon structures as lithium hosts, 3D carbon-based nanohybrids can also function as dendrite inhibitors. For example. Zhou et al. [189] embedded small Co nanoparticles into CC-supported N-doped carbon nanosheet arrays (CC@CN-Co) to regulate Li plating and stripping and reported that in the resulting 3D structured system, the conductive framework can lower local current density whereas N dopants can direct homogeneous Li nucleation due to strong interactions between each other, and tiny Co nanocrystals can guide Li deposition and growth direction. As a result, a symmetric cell using the Li-plated CC@CN-Co achieved long-term cycling with a low voltage polarization of 38 mV over 1000 h at 5 mA cm^{-2} and 5 mAh cm^{-2} with no dendritic Li crystal growth. The coupling of this anode with a $LiFePO_4$ cathode in a full cell further allowed for superior rate performances and a prolonged cycling life as compared with pristine Li counterparts.

7.3 Beyond-Li Batteries

See Fig. 15.

7.3.1 Sodium/Potassium Ion Batteries

Compared with lithium-based batteries, sodium-ion batteries (SIBs) and potassium-ion batteries (PIBs) possess several striking advantages, including high natural abundances, low costs and suitable redox potentials. Like LIBs, both SIBs and PIBs follow the rocking chair mechanism in which Na^+/K^+ transports back and forth in electrolytes [283, 284]. Despite this, electrodes suitable for Li storage may not be applicable to SIBs and KIBs due to the larger ionic radii of Na^+/K^+ (0.76, 1.02, 1.38 Å for Li^+, Na^+, K^+ respectively). For example, graphite is not a suitable anode for SIBs and KIBs because Na^+/K^+ diffusion into graphite layers can cause large volume expansion to result in structural collapse and rapid capacity fading [283, 284]. To address this, intensive efforts have been dedicated to the exploration of potential electrode materials for both batteries in which SIB/KIB anode materials can generally be divided into carbon, alloy or conversion type materials analogous to LIBs. Accordingly, carbon-based anodes for SIBs/KIBs have been optimized in recent years [284, 285] to enhance battery performance based on strategies including: (1) increasing interlayer distance, (2) heteroatom doping (e.g., N, S and P), (3) pore structure engineering and (4) micro/nanostructural construction. For example, Wang et al. [286] directly grew

GDY nanosheet arrays on Cu foil for Na^+ storage to achieve high energy and power density along with long cycle life and ascribed the enhanced properties to the 3D array structure and the pores between the GDY sheets that can provide intramolecular pores, an interconnective porous network and exposed active sites to accelerate charge diffusion. As a result, a high capacity of ~ 812 mAh g^{-1} at 0.05 A g^{-1} and 405 mAh g^{-1} over 1000 cycles at 1 A g^{-1}. In another example, Qiu et al. [287] prepared CC-supported N, P dual-doped vertical graphene arrays (N, P-VG@CC) as a flexible anode for KIBs in which by combing a highly conductive and robust framework with the easily accessible surface and rich active sites of the expanded interlayer spacing, the resulting N, P-VG@CC provided a high reversible capacity of 344.3 mAh g^{-1}, a high-rate capacity of 160 mA g^{-1} at 2 Ag^{-1} and long-term cycling for over 1000 cycles with 82% capacity retention, which are among the best reported in literature for metal-free carbon anodes.

3D flower-like hierarchical carbon anodes can also provide excellent electrochemical performance toward SIBs and KIBs in which through morphological, defect and structural engineering, Yu et al. [288] were able to prepare a 3D carbon anode with record-high Na/K-storage capabilities to achieve simultaneously unprecedented capacity and cycle lifes (Fig. 15a, b). Here, the N-doped 3D flower-shaped mesoporous carbon nanosheet (N-CNS)-based anode was obtained through rational engineering in three parts (Fig. 15a) with the first part involving morphological engineering in which a 3D hierarchical carbon structure was constructed through 2D nanopetals with fully exposed active surfaces and shortened charge diffusion pathways. The second step involved defect engineering in which rich N doping in the carbon framework resulted in the creation of rich defects as well as the modification of the electronic structure. As for the third step, this involved structural engineering in which augmented carbon interlayers enabled the rapid kinetics of Na^+/K^+ and simultaneously maintained structural integrity throughout repetitive Na^+/K^+ insertion/extraction. As such, the N-CNS in a corresponding SIB afforded a superb capacity of 370 mA g^{-1} at 1 A g^{-1} as well as remarkable rate capability retention of 106 mA g^{-1} at 50 A g^{-1} and exceptional cycling stability of 239 mA g^{-1} capacity over 4000 cycles at 5 A g^{-1} while for KIB, the N-CNS exhibited a capacity of 362 mA g^{-1} at 2 A g^{-1}, 191 mAh g^{-1} at 20 A g^{-1} and cycling stability of 321 mA g^{-1} at 5 A g^{-1} after 5000 cycles. Researchers further investigated the active sites based on first-principle calculations and found that pyridinic-N and pyrrolic-N possessed Na^+ (K^+) adsorption energy of −4.76 eV (−4.36 eV) and −4.25 eV (−3.91 eV), respectively, that was higher than the values of graphitic N (−0.37 eV for Na^+ and −0.88 eV for K^+) (Fig. 15b), rendering N-CNS with the highest contents of pyridinic and pyrrole N to show the strongest affinity to Na (K) ions and therefore the best Na^+/K^+ storage performance, which matched well with experimental results. Ji et al. [112] also fabricated a polymer-derived 3D N-doped porous carbon material with nanosheet-constructed rose-like morphology, an enlarged interlayer spacing of 0.387 nm and a high surface area of 215.7 m^2 g^{-1}. The resulting micropores/mesopores can shorten ion diffusion distances and increase interlayer distances to enhance Na^+ insertion/extraction, leading to a high reversible capacity of ~ 240 mAh g^{-1} at 100 mA g^{-1} for 100 cycles.

Aside from pure carbon anodes, 3D carbon-based nanohybrids have received equal attention for application in SIBs/KIBs [133, 289–291]. For example, Jiao et al. [133] prepared a WSe_2 nanocrystal-loaded N-doped porous carbon superstructure derived from cooperative self-assembly of a W-PDA complex and SiO_2@C nanospheres that enabled the full utilization of WSe_2 nanocrystal active materials due to the surrounding carbon superstructure with its nanoparticle-isolating capability, high electrical conductivity, maximized surface exposure and rich electroactive N dopants. Based on this, the resulting 3D WSe_2/NPC anode allowed for high reversible capacity and excellent cycling stability in both SIBs and KIBs in which a 316 mAh g^{-1} capacity over 400 cycles for a SIB and a 220 mAh g^{-1} capacity beyond 200 cycles for a PIB were achieved.

3D polymers can also demonstrate charge storage capabilities in SIBs/KIBs [113, 292]. For example, Li et al. [113] constructed 3D multi-carbonyl PI with a spherulite-like superstructure from highly dense and open-ended nanosheets as a SIB anode and reported enhanced interfacial energy storage with a capacity of 275.8 mAh g^{-1} at 25 mA g^{-1} and cycling stability of 130 mAh g^{-1} at 50 mA g^{-1} over 100 cycles.

7.3.2 Aqueous ZIBs and ZMBs

The use of flammable electrolytes as well as the limited reserve and inhomogeneous distribution of lithium mines makes LIB technologies unsuitable for applications such as grid-level energy storage. Alternatively, aqueous zinc ion batteries (ZIBs) have gained increasing attention as a viable candidate due to the large specific capacity (gravimetric, 820 mAh g^{-1}, volumetric, 5850 mAh cm^{-3}), suitable redox potential (−0.76 V vs. the standard hydrogen electrode), high abundance and superb safety of Zn in comparison with Li and other metals [293]. And although many other multivalent ion batteries (such as Mg, Ca and Al) can also provide theoretically large capacities, most perform poorly in water-based electrolytes owing to the formation of passivation layers on metal surfaces [294]. The working principles of ZIBs follow a metal ion migration mechanism similar to that of LIBs/SIBs/KIBs in which Zn ions can move between Zn anodes and cathodes during charge/discharge. Strictly

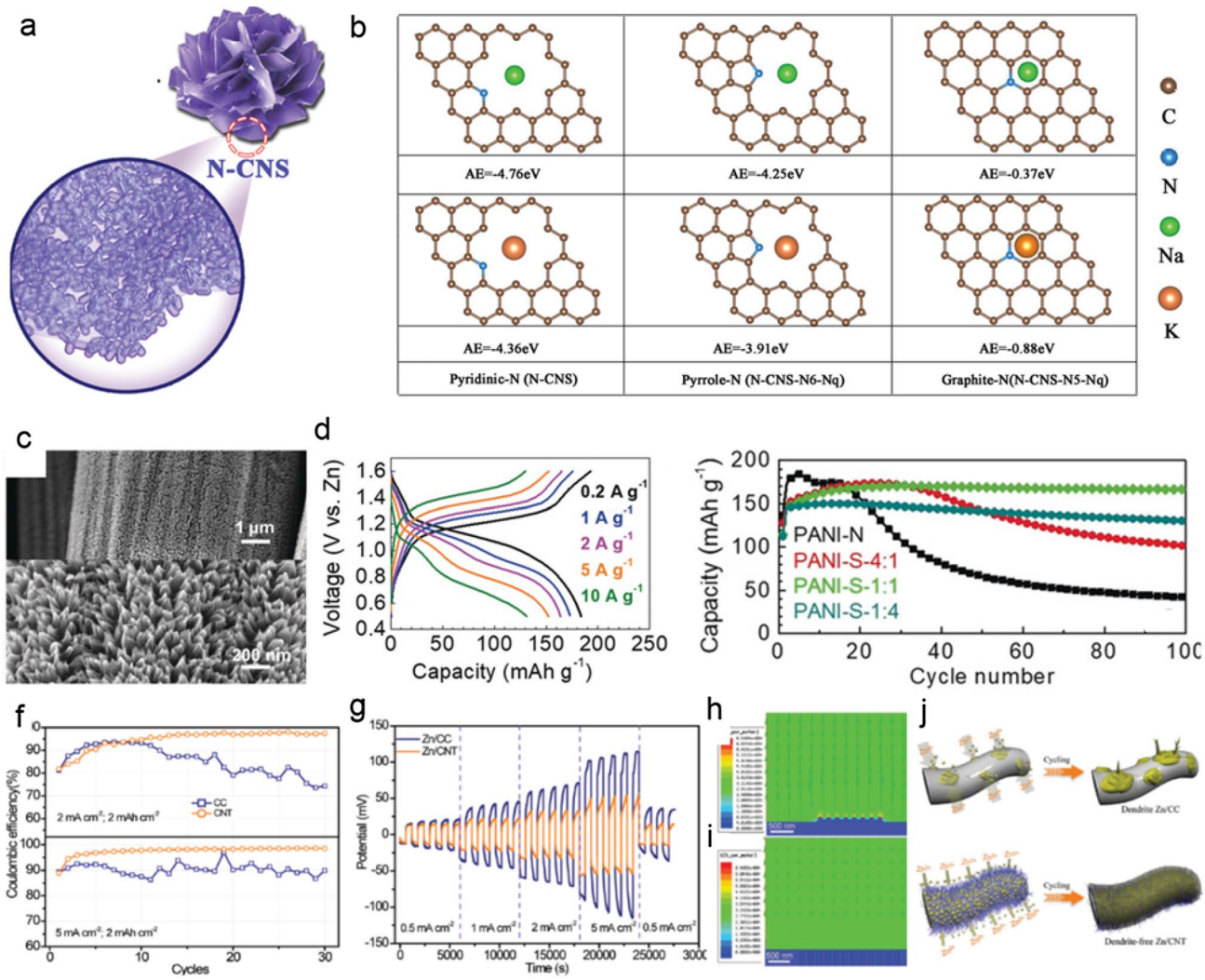

Fig. 15 3D HCMNs for beyond-Li batteries. Carbon flowers for SIBs and KIBs. **a** Schematic for carbon flowers including morphology, defect and structure engineering. **b** Adsorption energy between different nitrogen forms and Na^+/K^+ through first-principle DFT calculations. Reprinted with permission from Ref. [288]. Copyright © 2020, John Wiley and Sons. PANI arrays for ZIBs. **c** Morphology of self-doped PANI arrays on CC. **d** Voltage-capacity curves of PANI for a ZIB tested at different currents (from 0.2 A g^{-1} to 10 A g^{-1}). **e** Cycling stability of PANI with different self-doping levels. Reprinted with permission from Ref. [298]. Copyright © 2018, John Wiley and Sons. Hierarchical CNT arrays on CC for dendrite-free zinc metal anodes. **f** CE of zinc plating and stripping on CC or CNT/CC at 2 or 5 $mAcm^{-2}$ with 2 mAh cm^{-2} capacity. **g** Symmetric cells based on Zn/CC and Zn/CNT. Simulated electric field distribution around **h** pristine CC and **i** CNT/CC with deposited Zn nucleus. **j** Schematic of the growth of Zn crystals on CC and CNT/CC. Reprinted with permission from Ref. [37]. Copyright © 2019, John Wiley and Sons

speaking, this type of ZIB is considered to be Zn metal battery due to the use of Zn metal in the anode. As such, great efforts have been devoted to the search for cathode materials with higher potentials, larger capacities and better long-term cycling stability in which Mn-, V- and Co-based compounds as well as Prussian blue analogs and organic materials have been developed [295].

In comparison with inorganic materials that experience dissolution issues and short cycling lifespans, organic materials appear to be better choices as ZIB cathodes [296, 297]. For example, Shi et al. [298] prepared a sulfo-self-doped PANI (PANI-S) cathode for a rechargeable aqueous ZIB through the electrochemical copolymerization of aniline and metanilic acid onto CC (Fig. 15c-e) in which the resulting 3D PANI-S/CC electrode with vertical PANI nanoarrays was binder-free and self-standing (Fig. 15c) and was able to deliver a capacity of 184 mAh g^{-1} at 200 mA g^{-1}, an average discharge voltage of ~ 1.1 V, excellent rate capabilities of 130 mAh g^{-1} at 10 A g^{-1} as well as long-term cycling stability for over 2000 cycles with nearly 100 % CE (Fig. 15d, e), which were much better than non-self-doped PANI (PANI-N/CC) with worse Zn-storage capability and poorer stability.

Here, the superior performance of the PANI-S/CC can be ascribed to the 3D nanoarray structure with reduced resistances and fully exposed redox centers along with SO_3^- self-dopants that can serve as in situ proton reservoirs to retain high proton concentrations in PANI and boost the redox process as well as enhance long life cycles.

Other than the search for ideal cathode materials, the exploration of stable Zn anodes is of equal if not more significance in the development of ZIBs for large-scale energy storage applications [299] in which similar to many metal anodes including Li and Na, Zn anodes also experience infamous tip-induced dendrite growth that restricts further application in terms of safety and cycle lifespans. And although the use of near-neutral electrolytes can alleviate Zn dendrites to some extent, Zn metal anodes remain unsuitable for practical use in rechargeable battery systems in which dendritic growth and Zn metal anode passivation will lead to low reversibility and compromised ZIB energy density [300]. To address Zn dendrite growth, strategies such as electrolyte formulation, electrode modification, host construction and electrochemical manipulation have been developed. Here, the construction of 3D structured hosts to control Zn plating/stripping behavior is regarded as a promising strategy. For example, Zeng et al. [37] used CC as a substrate for the growth of CNT arrays and tested the resulting CNT/CC as a Zn host in half, symmetric and full cells for comparison with pristine CC as a control sample. The corresponding half-cell maintained the CE (ratio of stripping capacity to plating capacity) at ~ 95 to 97% in contrast to the rapid decay of the CE for pristine CC to 74% after 30 cycles at 2 mA cm^{-2} with 2 mAh cm^{-2} capacity (Fig. 15f), whereas at a high current density of 5 mA cm^{-2}, the CNT/CC displayed a stable CE of ~ 97.9% that was better than CC at only 90.3%. In addition, Zn dendrites were not observed on the smooth and uniformly deposited layers of the CNT/CC host during plating/stripping. Moreover, the symmetric cell tested at various rates demonstrate that the Zn-deposited CNT/CC electrode possessed considerably lower voltage hysteresis than that of the CC counterpart (Fig. 15g) in which as current reverted to low values (0.5 mA cm^{-2}), the Zn/CNT/CC experienced unchanged voltage hysteresis, whereas the Zn/CC experienced increased hysteresis, indicating the low polarization and high stability of the Zn/CNT/CC electrode. Furthermore, the full cell based on a Zn/CNT/CC anode and a MnO_2 cathode was able to deliver a high energy density of 126 Wh kg^{-1} and ultra-stable capacity with 88.7% retention over 1000 cycles. These researchers further simulated electric field distributions on the CNT/CC and CNT electrodes to uncover the 3D CNT framework as an efficient Zn host in which the Zn/CC electrode was revealed to possess inhomogeneous distribution with a high charge area near the Zn nucleus accompanied by uneven Zn deposition and dendrite growth (Fig. 15h, j), whereas the Zn/CNT/CC homogenized the electric field distribution with a minimized Zn nucleus and enabled plating without protuberance (Fig. 15i, j).

7.4 EDLC

In contrast to typical rechargeable batteries with low power densities, supercapacitors as another energy storage system can achieve high power densities to meet the increasing demand for rapid charging and discharging at high power. Because of this, supercapacitors are widely used in electric vehicles, industrial power generation devices and backup systems. According to the charge storage mechanism, supercapacitors can be divided into electrical double-layer capacitors (EDLCs) and pseudocapacitors in which EDLCs depend on the accumulation/release of electrostatic charge during charging/discharging at the electrode/electrolyte interface, whereas pseudo-capacitors are based on surface Faradic redox reactions such as charge intercalation/de-intercalation, adsorption/desorption and protonation/deprotonation [301]. In terms of components, although activated carbons are commonly used in commercial supercapacitors, their micropore-dominated porous structure is electrolyte-inaccessible and can hinder ion diffusion to lead to low capacitance and power density. Alternatively, 3D HCMNs with hierarchical pores and continuous networks possess greater potential in future supercapacitors due to advantages including high electrolyte-accessible surface areas for ion adsorption to give rise to high capacitance and energy density; ideal porous networks with hierarchical pores to facilitate ion diffusion and endow high rate performance; and minimal internal resistance within electrodes, especially at the interface between active materials and current collectors to allow for high power density. Because of this, 3D HCMNs have been intensively studied in recent years as both the active material for EDLCs and the supporting framework for pseudocapacitive materials for pseudocapacitors [302].

7.4.1 Microscale 3D HCMNs for EDLCs

As an example of microscale 3D HCMNs for EDLCs, Zhang et al. [303] studied CNT/PANI ensembles derived 3D carbon with 1D nanowhiskers on the 1D carbon nanofiber (CNF) as an EDLC electrode and reported that the 1D on 1D carbon architecture achieved an optimal capacitance of 210.1 F g^{-1} at 5 mV s^{-1} that was much higher than pure CNFs (2.6 F g^{-1}) and CNTs (10.6 F g^{-1}). Lee et al. [50] further fabricated 3D hierarchical crumpled graphene balls in large quantities for assembly into a binder-free 3D macroporous network that exhibited superb energy density for capacitive energy storage. To further improve performance, Chen et al. [63] decorated hierarchical graphene balls with CNT networks and reported that due to accelerated mass/charge transport and increased contact within the electrode, the 3D hierarchical

carbon far surpassed pristine crumpled graphene and flat GO sheets in terms of both capacitance and rate capability. Fan et al. [61] also investigated 3D CNT/graphene sandwiches with CNT arrays bridging graphene layers and reported that the 3D carbon ensured rapid charge transport within the EDLC electrode to give rise to a capacitance of 385 F g^{-1} at 10 mV s^{-1} as well as increased capacitance after 2000 cycles due to activation.

Researchers have also extensively applied flower-shaped 3D carbons as EDLC electrode materials [107, 147, 195, 197, 199, 200, 304–306] in which carbon flowers can be prepared based on templated synthesis, self-assembly or electrodeposition. As examples, Fan et al. [195] used a ZnO template, whereas Ding et al. [200] used an in situ generated $Ni(OH)_2$ template and Ma et al. [197] used a $Mg_5(CO_3)_4(OH)_2{\cdot}4H_2O$ template to achieve 3D carbon flower materials with hierarchical porous structures for supercapacitors in which the carbon flower material obtained by Ma et al. [197] possessed advantages including a high surface area up to 1927 m^2 g^{-1}, multilevel macro-/meso-/micropores, interlinked ultrasmall carbon nanocages and a 3D conductive network, resulting in the 3D carbon displaying a capacitance as high as 380 F g^{-1} at 1 A g^{-1} as well as high rate performance with a capacitance of 312 F g^{-1} even at 50 A g^{-1} in the three-electrode test. Symmetric supercapacitor based on the 3D carbon flower further demonstrated capacitances of 288 F g^{-1} at 1 A g^{-1} and 256 F g^{-1} at 10 A g^{-1}. Besides templated synthesis, self-assembly can also allow for the fabrication of carbon flowers. For example, based on hierarchically assembled PI, Xu et al. [107] synthesized carbon flowers which exhibited the capacitance of ~ 360 F g^{-1} at 0.5 A g^{-1} and 200 F g^{-1} at 10 A g^{-1} as well as remarkable stability for more than 10000 cycles. Liu et al. [147] further fabricated a carbon mint leaf structure based on a PAN ensemble that possessed an ultrahigh surface area of 3292.3 m^2 g^{-1} and showed capacitances of 331 F g^{-1} at 0.5 A g^{-1} and 220 F g^{-1} at 50 A g^{-1} in three-electrode tests. They also reported that a flexible all-solid-state asymmetric supercapacitor based on this 3D carbon electrode achieved an energy density of ~ 136 Wh kg^{-1} at a power density of 28.7 kW kg^{-1}. Moreover, Wang et al. [304] prepared an ordered mesoporous carbon flower structure based on a carbohydrate assembly that possessed a capacitance of ~ 200 F g^{-1} at 1 A g^{-1} for the EDLC, whereas Li et al. [305] fabricated 3D carbon mesh clusters (CMCs) in the form of a flower consisting of atomically thick N-doped carbon nanosheets based on electrodeposited Zn coordination polymer in which the resulting 3D N-CMC demonstrated a superhigh capacitance of 984 F g^{-1} at 0.5 A g^{-1}, superb rate capabilities of 541 F g^{-1} at 50 A g^{-1} and exceptional cycling durability with an enhanced 37% capacitance after 40000 charge–discharge cycles in a three-electrode configuration in acidic media. Two-electrode symmetric supercapacitor based on the 3D N-CMC showcased high capacitances of 385 F g^{-1} at 0.1 A g^{-1} and 297 F g^{-1} at 50 A g^{-1} along with minimal decay after 6000 charge/discharge cycles at 10 A g^{-1}, which were among the best reported for EDLCs. Sun et al. [154] further fabricated 3D B-doped carbon superstructures composed of vertical carbon nanosheets on graphene from vertically oriented COF nanosheets grown on GO and reported that the resulting carbon electrode afforded capacitances of ~ 165 F g^{-1} at 0.5 F g^{-1} and 150 F g^{-1} at 15 A g^{-1} with stability exceeding 3000 cycles, which were significantly better than parallelly grown carbon nanosheets on graphene due to enhanced electron transfer and ion diffusion as a result of the vertical sheets, demonstrating the potential of vertical graphene for application in high-performance EDLCs.

7.4.2 Macroscale 3D HCMNs for EDLCs

Vertical graphene (VG) are ideal electrode materials for EDLCs due to a binder-free feature and fully exposed surface areas with minimized internal resistance and maximized active carbon surface utilization. For example, Seo et al. [307] used butter as a precursor to grow VG on Ni foam through PECVD as an EDLC electrode material and obtained a high capacitance of 230 F g^{-1} at 10 mV s^{-1} scan rate and negligible capacitance loss over 1500 cycles at high current densities. VG can also function as bridging materials between graphene film active materials and nickel foam current collectors to greatly reduce interfacial resistance from limited contact points in which the vertical orientation, in-plane electrical conductivity, densely exposed edges, strong substrate binding and high chemical tolerance of VG as bridges can accelerate electron transport to endow supercapacitors with outstanding rate and power capabilities. Based on this, Bo et al. [308] prepared a VG-bridged supercapacitor that was able to maintain ~ 90% capacitance with a current density increase from 1 to 100 A g^{-1}, which led to ultrahigh power capabilities up to 112.6 kW kg^{-1} even at 600 A g^{-1}, surpassing almost all previously reported high-rate EDLCs. VG-based supercapacitors can also be applied as alternating current line filters for electronics with superfast frequency responses [309–312] in which at a frequency of 120 Hz, a VG/Ni foam-based EDLC demonstrated a phase angle of -82^{o} that was close to the ideal value (-90^{o}) and is superior to activated carbon-based EDLCs with values around 0^{o} [309].

3D covalently bonded CNT/graphene hybrid with vertically aligned SWCNT on graphene and a superhigh surface area > 2000 m^2 g^{-1} can be further applied to EDLCs [64]. Because the substrate for carbon growth was also used as the current collector, no binders were needed for electrode fabrication, which reduced overall device weight to allow for higher gravimetric energy density. And based on the 3D

CNT/graphene hybrid electrode, a corresponding supercapacitor delivered an output voltage up to 4 V and energy density of more than 60 Wh kg^{-1}, which are among the highest for EDLCs. Cycling tests further showed negligible energy loss after 5000 cycles, which can be attributed to the ultrahigh surface area as well as the ohmic contact between graphene and SWCNTs with covalent bonding at the atomic level.

Inspired by the structure and function of leaves on tree branches, Fisher et al. [313] designed a nanocarbon-based branch-and-leaves structure as a highly efficient and stable supercapacitor electrode (Fig. 16a) in which sharp-edged ultrathin graphene as "leaves" were arranged hierarchically on CNT array stems as "branches", both of which were grown on CC. Here, these structures were further formed into tunnel-shaped arrays to facilitate charge transfer between the electrolyte and the electrode surface in which the leaf-like graphene petals (GP) can provide electrode stability. As a result, the CNT/GP@CC electrode achieved record-high performance with 30% better gravimetric capacitance, 30 times better areal capacitance and 10 times more power than carbon-based supercapacitors (Fig. 16b) along with 95% capacitance retention after 10,000 cycles (Fig. 16c). And as compared with graphene-free CNT arrays and pure CC electrode materials, the CNT/GP@CC further exhibited the highest capacitive storage as shown in CV curves with the largest area (Fig. 16d) as well as the fastest charging/discharging rates as displayed in GCD plots (Fig. 16e).

Jia et al. [205] prepared radically aligned porous CNT arrays on flexible carbon fibers using ZnO nanorod arrays as a template and reported that the 3D arrangement, diameter and length of the CNT arrays can be adjusted through the fine-tuning of the ZnO template synthetic procedure in which the optimized 3D CNT electrode afforded a high specific capacitance of 182 F g^{-1} at 40 A g^{-1} under a three-electrode configuration, whereas a symmetric supercapacitor based on the 3D carbon exhibited excellent cycling stability for over 10000 continuous cycles at 12 A g^{-1}. Similar strategies involving the ZnO-templated synthesis of 3D carbon electrodes for EDLCs have also been reported. For example, Fan et al. [204] prepared 3D Ni tube/carbon sphere hybrid arrays based on vertical ZnO arrays on Ni foil as electrode materials for a symmetric supercapacitor and achieved high capacitance/energy density, power density and long-term cycling due to the unique composition and 3D core/shell arrayed structure in which Ni tubes as the core can enhance electrical conductivity and form intimate contact with carbon active materials to achieve high-rate charge/discharge performance.

7.5 Pseudocapacitors

In contrast to EDLCs based on the electrostatic adsorption of ions, pseudocapacitors relying on surface Faradaic-redox reactions typically show higher capacitances but lower power densities and shorter cycling lifespans [301] in which promising electrode materials with pseudocapacitive behaviors include RuO_2, metal oxides, conducting polymers and Mxenes. And although promising, these electrode materials have yet been extensively applied due to the high cost of RuO_2, the low capacitance of metal oxides, the poor stability of conducting polymers and the synthetic hazards of Mxenes [314].

7.5.1 Conducting Polymers

In terms of conducting polymers, these materials have been extensively investigated in pseudocapacitors due to their environmental friendliness, facile preparation, adjustable conductivity and reversible protonation/deprotonation features [315, 316]. In addition, suitable nanostructure designs and corresponding carbon material composition have been explored to resolve corresponding issues concerning low power density and poor stability. Here, the construction of vertical arrays can effectively extend cycle life in which Huang et al. [90] fabricated large-area vertically oriented PPy nanowire arrays (diameter: 80–100 nm) with controllable lengths (range: 1–4 μm) through electrochemical polymerization to present a high capacitance of 566 F g^{-1} and acceptable cycling stability with 70% retention after 300 cycles as a pseudocapacitor electrode that were superior to disordered nanowire networks with lower capacitances or conventional films with worse cycling lifespans (Fig. 16f, g). The optimal performance of the PPy arrays was attributed to the strain relaxation effects of the nanowire arrays and more accessible ion diffusion pathways. Yang et al. [102] also grew vertical PPy nanosheet arrays on Ni foam through evaporation-induced self-assembly for application in flexible solid-state asymmetric supercapacitors with activated carbon-coated Ni foam as the other electrode and reported a capacitance of 38 F g^{-1} at 0.2 A g^{-1}, an energy density of ~ 14 Wh kg^{-1} and a power density of 6.2 kW kg^{-1} as well as good stability (~ 82% capacitance retention after 2000 cycles).

In comparison with PPy, PANI has garnered more attention as a supercapacitor electrode material due to a higher theoretical capacitance. For example, Wang et al. [88] grew 50-nm-diameter vertically aligned PANI nanowire arrays onto various conducting substrates (Au, Pt, stainless steel, graphite, etc.) through electrochemical polymerization and reported capacitances as high as 950 F g^{-1} that can be maintained at 780 F g^{-1} at 40 A g^{-1}, which are better than values previously reported based on disordered PANI nanowires

and PPy-based materials, demonstrating the potential of PANI and oriented nanostructure designs for high-power pseudocapacitors. In another example, Tong et al. [317] facilely synthesized PANI nanotube arrays through ZnO nanorod arrays-directed electrochemical polymerization and subsequent acid etching as an electrode and reported mechanical flexibility and high capacitance, demonstrating promise for application in flexible supercapacitors.

In the past decade, researchers have started to combine PANI arrays with various carbon materials such as microscale fullerene, CNTs and graphene as well as macroscale carbon fibers, paper/films and aerogels to prepare 3D PANI/C supercapacitor electrodes. For example, Xiong et al. [318] synthesized a coral-shaped fullerene–PANI hybrid (C_{60}/PANI) through the chemical copolymerization of aniline with phenylenediamine-functionalized C_{60} in

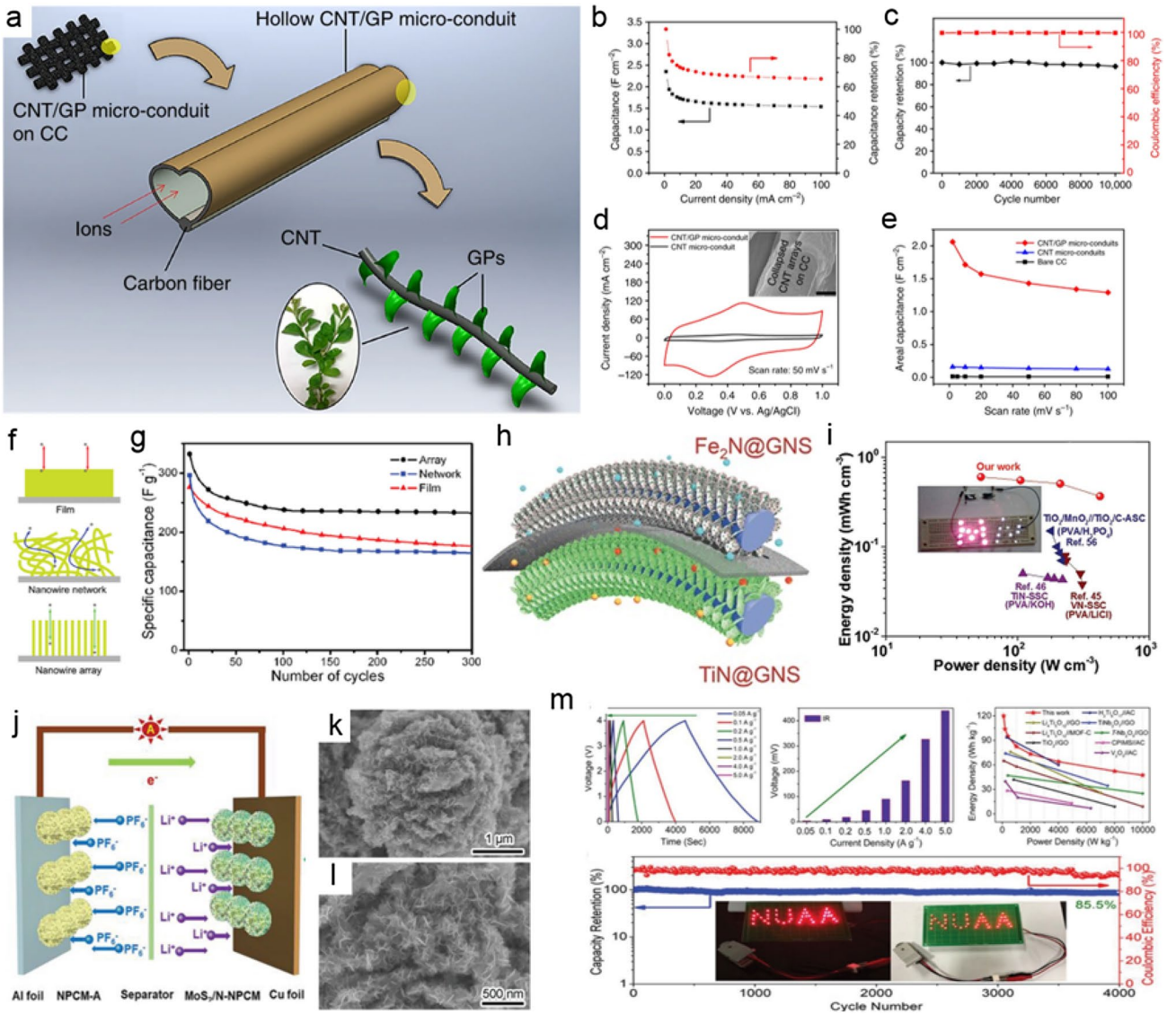

Fig. 16 3D HCMNs for supercapacitors. Bio-inspired hybrid carbon nanostructure for supercapacitors. **a** Schematic of CNT/GP micro-conduits in a leaves-on-branchlet nanostructure on CC substrates. **b** Specific capacitance and capacitance retention. **c** Charge/discharge cyclic stability. **d** Comparative CV curves. **e** Comparison of areal specific capacitances. Reprinted with permission from Ref. [313]. Copyright © 2018, Springer Nature. Conducting polymer nanowire arrays for supercapacitors. **f** Schematic comparing ion diffusion in PPy films, NW networks and NW arrays. **g** Stability of PPy with varying morphology. Ref. [90]. Copyright © 2010, Royal Society of Chemistry. TiN@GNS cathode and Fe_2N@GNS anode for asymmetric supercapacitors. **h** Schematic of TiN-Fe_2N ASC. **i** Ragone plots of quasi-solid-state TiN-Fe_2N ASC. Reprinted with permission from Ref. [327]. Copyright © 2015, John Wiley and Sons. Ultrathin MoS_2 nanosheets anchored onto N-doped carbon microspheres for pseudo supercapacitors. **j** Schematic of the application of MoS_2/N-NPCM battery-type anodes. **k-l** FESEM images. **m** Electrochemical properties of individual electrodes and full devices. Reprinted with permission from Ref. [334]. Copyright © 2019, John Wiley and Sons

which the porous C_{60}/PANI coral was constructed based on interconnected nanofibers with low crystallinity to enhance ionic conductivity, whereas the covalent bonding of C_{60} with PANI can result in strong electron-withdrawing property to enhance electrical conductivity and electrochemical stability. As a consequence, the obtained C_{60}/PANI showed much higher capacitance (776 F g^{-1} for C_{60}/PANI as compared with 492 F g^{-1} for PANI at 1 mA cm^{-2}), better specific power and energy densities and superior cycling stability as compared with pristine PANI. Wang et al. [93] further grew ordered whisk-like PANI nanoarrays onto mesoporous carbon for application in pseudocapacitors and obtained high capacitances of 900 F g^{-1} at 0.5 A g^{-1} and 768 F g^{-1} at 5 A g^{-1} as well as long cycling stability for over 3000 cycles with only 5% loss.

In another example, Malik et al. [319] composited 3D CNT film-supported vertically aligned N-doped CNT arrays with PANI nanolayers and obtained binder-free PANI/NCNT electrodes that demonstrated a capacitance of 359 F g^{-1} at 1.56 mA cm^{-2} and high-rate capabilities with 82% capacitance retention at 46.87 mA cm^{-2}. A corresponding flexible symmetric supercapacitor further presented a capacitance of 128 F g^{-1} at 2.47 A g^{-1} and capacitance decays less than 8% after 10000 cycles even at a high current density of 24.7 A g^{-1}. Other CNT-based substrates including CNT carbon fibers and CNT paper have also been applied for the vertical growth of PANI arrays to manufacture 3D electrodes for all-solid-state flexible symmetric supercapacitors [320, 321].

Alternatively, VG arrays on CC can function as substrates for the conformal deposition of PANI nanolayers. For example, Xiong et al. [322] obtained a PANI/VG/CC hybrid electrode that yielded a near-theoretical gravimetric capacitance of 2000 F g^{-1} (based on PANI), an areal capacitance of ~ 2.6 F cm^{-2}, a volumetric capacitance of ~ 230 F cm^{-3} at 1 A g^{-1} and capacitances greater than 1200 F g^{-1} for currents up to 100 A g^{-1}, which is equivalent to an optimal energy density of ~ 110 Wh kg^{-1} and a power density of 265 kW kg^{-1} at 100 A g^{-1}, along with good cyclic stability with 93% initial capacitance retention after 2000 cycles. Based on two PANI/VG/CC electrodes, an all-solid-state flexible supercapacitor further achieved excellent capacitive performances. Aside from VG arrays, graphene oxide nanosheets, graphene membranes and aerogels have also been explored to enhance PANI performance [94, 99, 323].

The rational design of composites based on conducting polymers and metal oxides can further provide opportunities to enhance pseudocapacitors. In one representative example, Wang et al. [324] prepared large-area single-walled PPy nanotube arrays and multi-walled MnO_2/PPy/MnO_2 nanotube arrays with controllable structures through template-assisted electrodeposition in which the diameters, lengths and wall thicknesses of the nanotubes can be fine-tuned and reported that in the MnO_2/PPy/MnO_2 arrays, the PPy nanolayers can act as high-speed electrically conductive pathways to closely connect MnO_2 shells and facilitate redox reactions in the double MnO_2 shells, the design of multi-walled nanotube arrays enabled easy access to electrolytes and rapid charge transport to result in high capacitances, large energy and power densities and excellent long-term cycling stability. Based on this, this method can potentially be applied in other composites of metal oxides and conducting polymers to achieve multifunctional micro/nanostructured hybrids.

7.5.2 Metal-Containing Carbon Hybrids

Transition metal-based materials, particularly metal oxides, have been extensively explored as electrodes for pseudocapacitors. And although transition metal-based supercapacitor electrodes face major challenges such as low specific capacitance and poor electrical conductivity, the coupling of these metal-containing species with 3D carbon substrates can synergistically enhance electrochemical performance in which CNTs, graphene and corresponding hybrids have been employed as efficient conductivity and performance enhancers. For example, Zhang et al. [325] grew MnO_2 nanoflowers onto VACNT arrays through electrodeposition to prepare binder-free MnO_2/VACNT pseudocapacitor electrodes and obtained a gravimetric capacitance of 199 F g^{-1} and a volumetric capacitance of 305 F cm^{-3} as well as rate capability with 50.8% capacity retention at 77 A g^{-1} and cyclic stability with 97% capacitance retention after 20000 cycles. A similar strategy was adopted by Zhang et al. [326] to prepare vanadium nitride/CNT arrays for pseudocapacitors to achieve a specific capacitance of 289 F g^{-1} and rate performances up to 1000 mV s^{-1}. Aside from VACNT arrays, VG arrays are also effective conductive supports. For example, Zhu et al. [327] homogeneously grew Fe_2N and TiN metal nitrides onto VG arrays through atomic layer deposition (Fig. 16h) and used the obtained Fe_2N@VG and TiN@VG as the anode and cathode in an all-solid-state supercapacitor, respectively, to achieve a capacitance of ~ 58 F g^{-1} at 4 A g^{-1} and long cycling stability up to 20000 cycles as well as high energy (gravimetric: ~ 15.4 Wh kg^{-1}, volumetric: ~ 0.51 mWh cm^{-3}) and power densities (gravimetric: ~ 6.4 kW kg^{-1}; volumetric: ~ 211.4 mW cm^{-3}; Fig. 16i). Xiong et al. [328] further used 3D CNT/graphene hybrids for transition metal-based pseudocapacitive storage in which VGA were grown on CNT bulky paper through CVD as a substrate for the electrodeposition of a MnO_2 thin layer in which the final binder-free MnO_2/VGA/CNT composite as an electrode material for a supercapacitor provided a high capacitance of 580 F g^{-1}, an energy density of 28 Wh kg^{-1} and a power density of 25 kW kg^{-1} at 50 A g^{-1} along with good cyclability. Here, DFT calculations revealed that the vertical orientation of graphene accelerated ion diffusion whereas the

covalently connected MnO_2 and graphene favored charge transfer, all of which contributed to high-performance. 3D pillared VACNT–graphene structures have also been used to improve the capacitive storage performance of $Ni(OH)_2$ electrode materials [62].

More recently, MOFs have been investigated as supercapacitor electrode materials due to capacitive storage potentials based on the combination of metal species with organic ligands. For example, Yang et al. [169] prepared flower-shaped Zn-doped Ni-MOFs through a wet chemical approach as a supercapacitor electrode material in which an optimized MOF with a Zn/Ni ratio of 0.26 exhibited specific capacitances of 1620 F g^{-1} at 0.25 A g^{-1} and 860 F g^{-1} at 10 A g^{-1} as well as small capacitance losses of 9% over 3000 cycles that can be ascribed to the hierarchical structure, expanded interlayer spacing and rich porosity of the material. Jiao et al. [170] subsequently enhanced this Ni-MOF electrode through the partial substitution of Ni with Co to achieve an ultrahigh energy density of 61.8 Wh kg^{-1} at a power density of 725 W kg^{-1} accompanied by a long cycling lifespan of over 5000 cycles in which the better performance can be attributed to Co substitution with increased electronic conductivity, higher specific surface area and pore enlargement in the bimetallic MOF. Yang et al. [173] further fabricated an accordion-like Ni-MOF capacitive electrode and achieved high capacitances of 988 F g^{-1} at 1.4 A g^{-1} and 823 F g^{-1} at 7.0 A g^{-1} as well as prolonged cycling with negligible loss over 5000 cycles. This accordion-like Ni-MOF capacitive electrode was also assembled into a flexible solid-state asymmetric supercapacitor with activated carbon as a counter-electrode to achieve a capacitance of 230 mF cm^{-2}, long-term cycling stability for more than 5000 cycles with a maximum energy density of 4.18 mWh cm^{-3} and a power density of 231.2 mW cm^{-3}. Zhang et al. [329] also coated Mn-MOF with a layer of MnO_x nanoflower through rapid reaction with NH_4F additive to achieve threefold enhancement in capacitance (1200 F g^{-1} vs. ~ 300 F g^{-1} at 10 A g^{-1}) in comparison with pristine Mn-MOF in which a flexible supercapacitor based on the MOF-MnO_x and an activated carbon electrode showed optimal specific capacitance and energy density among MOF-based supercapacitors.

Aside from direct use as an active material, MOFs can also be converted into carbon or carbon-based hybrids for supercapacitors. For example, Guan et al. [185] grew Co-MOF nanowall arrays onto a CC substrate to accommodate an ion exchange and carbonization process to generate $NiCo_2O_4$/C arrays for flexible supercapacitors in which benefiting from the ultrathin nanosheet arrays with a hollow and porous structure on a conductive substrate, the constructed flexible supercapacitor enabled a high energy density of 31.9 Wh kg^{-1} at 2.9 kW kg^{-1}, a maximum power density of 22.9 kW kg^{-1} and extended cycling. In another example, Huang et al. [330] used MOF-derived carbon nanowall arrays for the secondary growth of vanadium nitride and $Na_{0.5}MnO_2$ as the anode and the cathode, respectively, in an asymmetric supercapacitor to obtain high capacitance and good stability in which the assembled aqueous supercapacitor achieved a 2.6 V voltage window, an ultrahigh energy density of 96.7 Wh kg^{-1}, a high power density of 1.29 kW kg^{-1} and excellent durability for over 10000 cycles, which surpassed most reported water-based supercapacitors and were even comparable to organic electrolyte-based supercapacitors.

7.6 Hybrid Metal-Ion Capacitors

Hybrid metal-ion capacitors (HMICs) involving the combination of supercapacitor cathodes with battery anodes can simultaneously achieve high energy density and power density in a variety of applications ranging from portable electronics to electric vehicles [331]. And although lithium ion capacitors (LICs) have been extensively investigated and can present a typical energy density of ~ 30 Wh kg^{-1}, sodium ion capacitors (NICs) and potassium ion capacitors (KICs) have attracted increasing attention in recent years due to the elemental abundance of Na and K. Despite this, kinetic differences between battery anodes and capacitor cathodes in HMICs hinder application, especially sluggish Faradaic reactions on the battery side [331]. To address this, tremendous efforts have been dedicated to the design of 3D hierarchical structured electrodes with short diffusion pathways for electron and ion transport.

For example, Wang et al. [224] grew GDY nanowall arrays onto Cu foil as a LIC anode and obtained a high capacitance of ~ 208 F g^{-1} over 10000 cycles at 1 A g^{-1}. And as coupled with an activated carbon cathode at a wide voltage range of 2–4 V, the resulting LIC manifests a high energy density of 217 Wh kg^{-1} at a specific power of 150 W kg^{-1}. PI superstructures and nanoarrays can also be applied to hybrid supercapacitors. For example, Cui et al. [332] applied N-doped carbon spheres derived from self-assembled PI as a LIC anode and reported that the optimized electrode delivered specific capacities of 328.3 and 48.2 mAh g^{-1} at 10 mA g^{-1} and 10 A g^{-1}, respectively. And if coupled with an activated carbon cathode, the spherical carbon electrode provided an energy density of 28.5 Wh kg^{-1} at 348 W kg^{-1} based on both electrodes. Zhang et al. [333] also prepared a LIC based on the direct use of PI-derived N-doped carbon flowers (NCFs) as an anode and KOH-activated NCF with high surface areas up to 2007 m^2 g^{-1} as the cathode and reported that due to the superstructured electrode materials and the porous current collector, the LIC displayed energy densities as high as 95.08 Wh kg^{-1} together with long cycling stability for 5000 cycles at a fading rate of only ~ 0.004% per cycle. Jiang et al. [334] subsequently in situ grew MoS_2 onto NCF with expanded

interlayer distance to act as a LIC anode (Fig. 16j) in which the typical MoS_2/NCF hybrid morphology involved numerous ultrathin MoS_2 nanosheets standing on a spherical flower-like carbon superstructure (Fig. 16k, l) and reported that if coupled with an activated carbon cathode, an assembled LIC can provide a high energy density of 120 Wh kg^{-1} with 85.5% performance retention over 4000 cycles, which is better than most reported LICs in literature (Fig. 16 m).

Beyond LICs, 3D PI and derived carbons have also been applied as electrodes for NICs and KICs. For example, Zhang et al. [335] fabricated an aqueous NIC using PI as the anode, PI-derived porous carbon as the cathode and 17 M $NaClO_4$ in water as the super concentrated electrolyte and obtained a working voltage of 2.0 V, a high energy density of 65.1 Wh kg^{-1}, a power density of 20 kW kg^{-1} and good stability with 14% capacity decay over 1000 cycles. Zhao and coworkers [336] also applied PI in a non-aqueous NIC with a working voltage of 4.2 V to obtain a maximum energy density of 66 Wh kg^{-1} and a power density of 1200 W kg^{-1}. The same group [337] further enhanced the capacity of PI from 50 mAh g^{-1} to 225 mAh g^{-1} through growth onto 3D rGO gels in which a flexible NIC fabricated based on the freestanding PI/rGO–rGO composite as the anode and rGO as the cathode afforded a high energy density of 55.5 Wh kg^{-1} at 395 W kg^{-1}. In another study, Nie et al. [338] fabricated a KIC based on PI-derived NCF as the anode and activated NCF as the cathode and obtained a maximum energy density of 90.1 Wh kg^{-1}, a power density of 3000 W kg^{-1} and long-term cycling up to 5000 cycles with ~ 100% CE.

Fan et al. [339] also reported the use of 3D carbon-supported VO_2 as the anode and $Na_3V_2(PO_4)_3$ as the cathode for a NIC. Here, the 3D carbon was composed of carbon nanosheet arrays derived from MOF arrays on CC with rich oxygen/nitrogen-containing functional groups that can allow for the easy binding of metal ions through coordination or electrostatic interactions. As a result, a solid-state hybrid NIC using the flexible binder-free electrodes coupled with a gel polymer electrolyte provided high energy densities (gravimetric: ~ 161 Wh kg^{-1}; volumetric: 8.83 mWh cm^{-3}) and power densities (gravimetric: 24 kW kg^{-1}, volumetric: 1.32 Wh cm^{-3}) that surpassed most previously reported NICs.

7.7 Device Configuration

Recently, portable and wearable electronics have become increasingly important and require miniaturized, light, safe, durable and integrated devices [340, 341]. To power these devices, the development of miniaturized energy storage devices (MESDs) that are in the centimeter or even millimeter scale with working electrodes in the micron scale is crucial. Here, MESDs can be divided into fiber, in-plane and 3D configurations [341], and this section will briefly discuss the recent progress of 3D HCMNs for miniaturized supercapacitors.

Fiber-like supercapacitors Flexible fiber-shaped supercapacitors (Fig. 17a) have been extensively investigated in recent years to meet the demands of modern flexible and stretchable electronics [342]. For example, Wang et al. [100] prepared a fiber-shaped supercapacitor involving the two-ply CNT yarn grown with PANI nanowire arrays as the electrodes and salt-containing PVA gel as the electrolyte that was flexible and can be easily woven into fabrics for wearable electronics to obtain an areal capacitance of 38 mF cm^{-2} that was 16-fold greater that of pristine CNT yarn (~ 2.3 mF cm^{-2}) as well as 91% capacitance retention after 800 cycles. Xiong et al. [343] also used a special paper-wrap-twist-fiber device structure containing VG grown on carbon fiber as a negative electrode, MnO_2 nanosheets grown on CNT paper as the positive electrode and PVA with KOH/H_3PO_4 as the electrolyte and separator to prepare an all-solid-state asymmetric fiber supercapacitor that showcased large capacitance, mechanical flexibility, good stability and high energy and power densities, which these researchers attributed to the edge-on carbon structure and the rationally designed device architecture. Dai et al. [66] further designed and fabricated 3D graphene–CNT hollow fibers with covalent connections between the graphene layers and the aligned CNT arrays as an electrode material for an all-solid-state wire-shaped supercapacitor to obtain a record-high areal capacitance of 89.4 mF cm^{-2} and a line capacitance of 23.9 mF cm^{-1} that were much better than other fiber-like supercapacitors, which can be attributed to the high surface area and minimized interfacial resistance of electrode materials. Moreover, these fiber supercapacitors can be integrated in series or parallel to increase output potential and/or current in which the electrochemical performance of three 3D graphene–CNT fiber-based supercapacitors connected in series (Fig. 17b) provided an increased voltage from 0.8 to 2.4 V with no change in capacitance (Fig. 17c, d). In another example, Peng et al. [118] prepared a fiber-shaped asymmetric supercapacitor (FAS) using PI nanosheet arrays on CNT fiber as the negative electrode and hierarchical MnO_2 nanosheet-coated CNT fiber as the positive electrode to achieve a large voltage window of 2.1 V, a high areal energy density of 36.4 μWh cm^{-2} and a power density of 15.6 mW cm^{-2} at 30.2 μWh cm^{-2} along with long-term cycling, high rate performances and excellent flexibility.

Micro-supercapacitors In recent years, micro-supercapacitors (Fig. 17e) have also been regarded as promising micro-battery replacements or energy harvester compensators to power microelectronics [340]. For example, Wei et al. [96] combined "top-down" photolithography and "bottom-up" in situ polymerization approaches to grow PANI arrays onto interdigital electrodes on flexible polymer

films for micro-supercapacitors in which the resulting flexible micro-supercapacitor displayed an ultrahigh volumetric capacitance of 588 F cm^{-3} as well as good rate capabilities and reduced leakage current. These devices can further be integrated in series or parallel to output higher voltages or currents. Through simple laser writing, Tour et al. [123] prepared micro-supercapacitors on PI membranes that used interdigital electrodes containing the vertically aligned laser-induced graphene fiber (LIGF) up to 1 mm in height (Fig. 17f) and reported that the micro-supercapacitor based on the LIGF/LIG hybrid showed the highest capacitance, whereas a micro-supercapacitor based on LIGF showed 50% higher capacitance as compared with a micro-supercapacitor based on LIG (Fig. 17g).

Integrated system Integrated energy systems have become more prominent in recent years in which ideal integrated energy systems should combine energy conversion, energy storage and sensors in one. Due to fabrication complexities however, only a few integrated energy systems have been achieved, including self-powered LIBs, self-charging supercapacitors and smart windows [342]. For example, Wang et al. [98] proposed a concept device called the Energy Storage Smart Window (ESS window) through the integration of a solar cell with a supercapacitor (Fig. 17h) in which under sunlight, solar energy can be stored into the ESS window to gradually darken its color until the strong sunlight is cut-off. Based on this, this smart device can provide energy for devices such as cell phones and screens. In addition, because the color of the window lightens after energy consumption, it is a good indicator of power level in corresponding energy storage devices and in turn can provide the possible control of light transmission. Here, the fabrication of the sandwich-like supercapacitor involved the spin coating of a PET film surface as the substrate with PEDOT:PSS as a current collector followed by the in situ polymerization of PANI nanowire arrays as the active material onto the current collector and the coating of a H_2SO_4-PVA gel electrolyte onto the electrode surface (Fig. 17i, j), which will result in a device that shows a yellow green color if fully discharged (0 V) and a dark blue color if fully charged (1 V, Fig. 17k).

8 3D HCMNs for Catalysis

8.1 Electrocatalysis

See Fig. 18.

8.1.1 ORR

Fuel cells are energy storage devices that rely on cathodic oxygen reduction and anodic oxidation. Unlike anodic hydrogen oxidation with relatively fast kinetics, cathodic oxygen reduction reactions (ORRs) are sluggish and thus

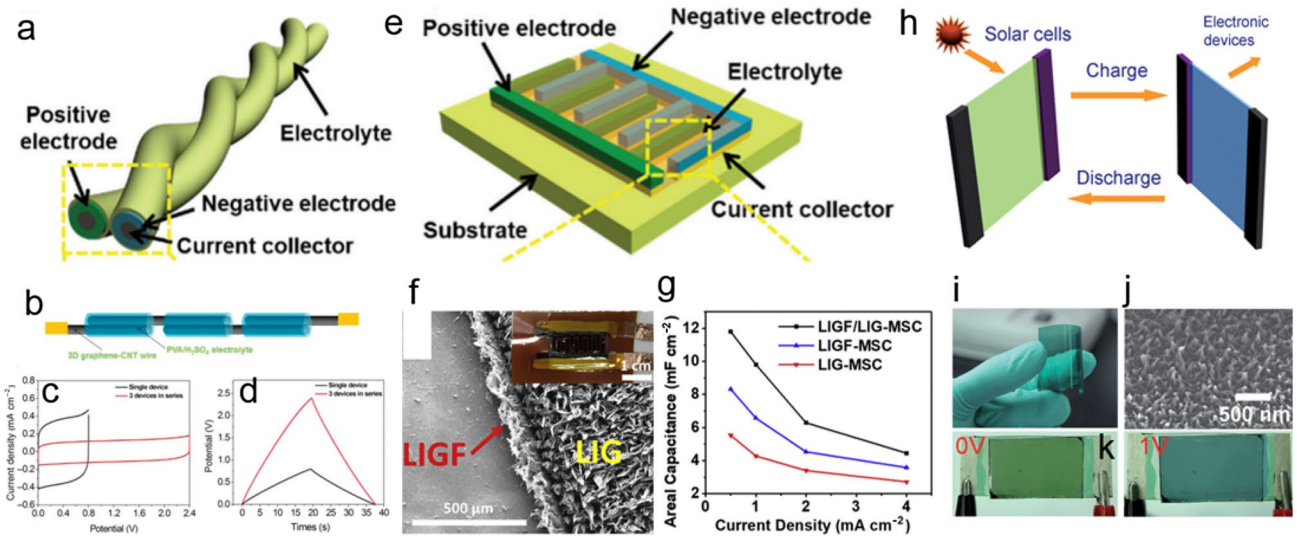

Fig. 17 3D HCMNs for miniaturized supercapacitors with different configurations and functions. Fiber-like supercapacitors. **a** Reprinted with permission from Ref. [341]. Copyright © 2018, Royal Society of Chemistry. 3D CNT/graphene for all-solid-state fiber-shaped supercapacitors. **b** Schematic of a three-wire supercapacitor connected in series and corresponding **c** CV curves and **d** GCD curves. Reprinted with permission from Ref. [66]. Copyright © 2015, American Association for the Advancement of Science. Micro-supercapacitors. **e** Reprinted with permission from Ref. [341]. Copyright © 2018, Royal Society of Chemistry. Laser-induced graphene for solid state micro-supercapacitors. **f** SEM image of the LIG-LIGF-MSC. **g** Capacitance comparison between LIG samples. Reprinted with permission from Ref. [123]. Copyright © 2017, Elsevier. Integrated system. **h** Energy Storage Smart Window. **i** Photograph showing a single electrode with certain transmission. **j** Morphology of PANI arrays. **k** Images of the device under different potentials. Reprinted with permission from Ref. [98]. Copyright © 2012, Royal Society of Chemistry

play a decisive role in fuel cell performance. And this sluggishness necessitates the use of electrocatalysts such as noble metal-based catalysts, which however are expensive and scarce, hindering the widespread commercialization of fuel cells. Because of this, the development of cost-effective non-noble metal catalysts is required and has resulted in considerable progress in the past decade such as metal-free catalysts, carbon-rich nanohybrid catalysts and single-atom catalysts [11, 344, 345].

Metal-free catalysts Dai et al. [31] were the first to prepare N-doped VACNTs through CVD as a metal-free carbon-based ORR catalyst that followed the four-electron pathway for ORR to provide enhanced electrocatalytic activity and stability as compared with Pt as well as better tolerance to crossover effects in alkaline fuel cells in which the exceptional performances were ascribed to the modified electronic structure of CNTs after electron-withdrawing N atom incorporation and NCNT vertical alignment. Subsequently, many metal-free carbon electrocatalysts with single or multiple dopants (N, P, S, O, B, F, etc.) and optimized micro/nanostructures have been developed [346]. For example, Guo et al. [347] grew VA-NCNTs onto carbon nanofibers to achieve a freestanding NCNT/CNF composite as an efficient ORR catalyst through the pyrolysis of pyridine over CNF film with a pre-loaded Fe catalyst in which the resulting 3D NCNT/CNF enabled more efficient alkaline ORR catalysis and demonstrated superior stability and methanol resistance as compared with powdery NCNT, CNT/CNF and Pt/C catalysts due to pyridinic-N doping and a binder-free hierarchical structure. Che et al. [348] further used an AAO-templated route to prepare N-doped carbonaceous nanotube arrays with an inner diameter of ~ 200 nm for ORR by infiltrating PAN into the template followed by etching-pyrolysis and reported that the resulting macroporous tubular structure can facilitate mass transfer whereas electron-rich N doping can activate the π electrons of sp^2 carbon materials to lead to better catalytic performances than Pt/C catalysts, including more positive onset potentials and half-wave potentials, higher reaction currents along with a four-electron-transfer reduction pathway. Yu et al. [349] also prepared P and N co-doped vertically aligned CNT arrays through injection-assisted CVD for ORR and obtained good catalytic activity and long-term durability that outclassed single doped counterparts such as P-doped or N-doped CNT arrays. Similarly, Zhu et al. [350] reported that the direct pyrolysis of nitrogen and phosphorus-containing polymers in the presence of nickel foam can result in N, P-dual-doped CNT arrays with open-ended structures and large hollow pores that can provide easily accessible active sites to render superior catalytic ORR activity which is better than previously reported N, P-dual-doped CNTs and is comparable to Pt/C but with much better methanol/CO tolerances and stability due to the synergistic effects of dual doping and the 3D structure.

Besides macroscopic vertical carbon arrays, microscale hierarchical carbons are also being actively investigated as ORR catalysts. For example, Xu et al. [107] derived N-doped porous carbon superstructures (NPCs) with various morphology including flower (NCP-F), disk (NCP-D) and lantern (NPC-L) from hierarchically assembled polymers as high-efficient ORR electrocatalysts (Fig. 18a) as well as spherical carbon particles (NPC-S) for comparison and reported that in terms of half-wave potential and diffusion-limiting current density (Fig. 18b), the ORR activity trend followed in the order of: Pt/C (0.85 V, 5.6 mA cm^{-2}) ≈ NPC-F (0.84 V, 5.5 mA cm^{-2}) > NPC-D (0.80 V, 5.1 mA cm^{-2}) > NPC-L (0.81 V, 4.8 mA cm^{-2}) > NPC-S (0.67 V, 4.5 mA cm^{-2}). They also reported that the electron transfer number of NPC-F at 3.67–3.94 over a potential range of 0.0–0.8 V (Fig. 18c) was higher than other NPCs (less than 3.5 transfer electrons) and signified a four-electron transfer mechanism for ORR catalysis. Chronoamperometric testing further verified the excellent durability and methanol tolerance property of NPC-F that were much better than Pt/C catalysts. Overall, the exceptional ORR performances of the NPC-F were among the best for metal-free electrocatalysts and can be attributed to its optimal surface area with its mostly open structure and maximum exposed active sites. Li et al. [351] also prepared 3D flower-shaped N-doped carbon through the one-step high temperature annealing of ferrocene and melamine in which N dopant was modulated by pyrolysis temperature and pyridinic-N species were determined to be the active sites for ORR. Huang et al. [352] further use a silica-urchin-templated approach to synthesize uniformly sized 3D hierarchical N-doped carbon nanoflowers (NCNFs) with ample mesopores and a large surface area of 907 $m^2 g^{-1}$ as well as a high pore volume of 1.85 $cm^3 g^{-1}$. As a result, the NCNF exhibited remarkable electrocatalytic activities approaching Pt/C (20 wt%) but with much better durability. These researchers also doped S into the NCNF by charging/discharging in Li–S batteries and reported that the resulting sample demonstrated superior ORR activity to Pt/C with enhanced onset and half-wave potentials as well as limiting current densities. In another study, Yamauchi et al. [353] prepared a 3D carbon electrocatalyst with a conductive graphitic structure and abundant N dopants through the pyrolysis of MOF-derived graphitic carbon@COF core–shell hybrids in which COF shells can serve as precursors to form N-doped porous carbon whereas ZIF-67 cores can derive graphitic carbon, resulting in a core–shell heterostructure that allowed for high ORR activity with comparable onset and half-wave potentials (0.923 V, 0.841 V) but superior stability to Pt/C catalyst.

Carbon-based hybrid catalysts Apart from metal-free catalysts, 3D carbons can also function as catalyst supports for electroactive components such as metals, metal sulfides and carbides [354, 355]. For example, Xu et al.

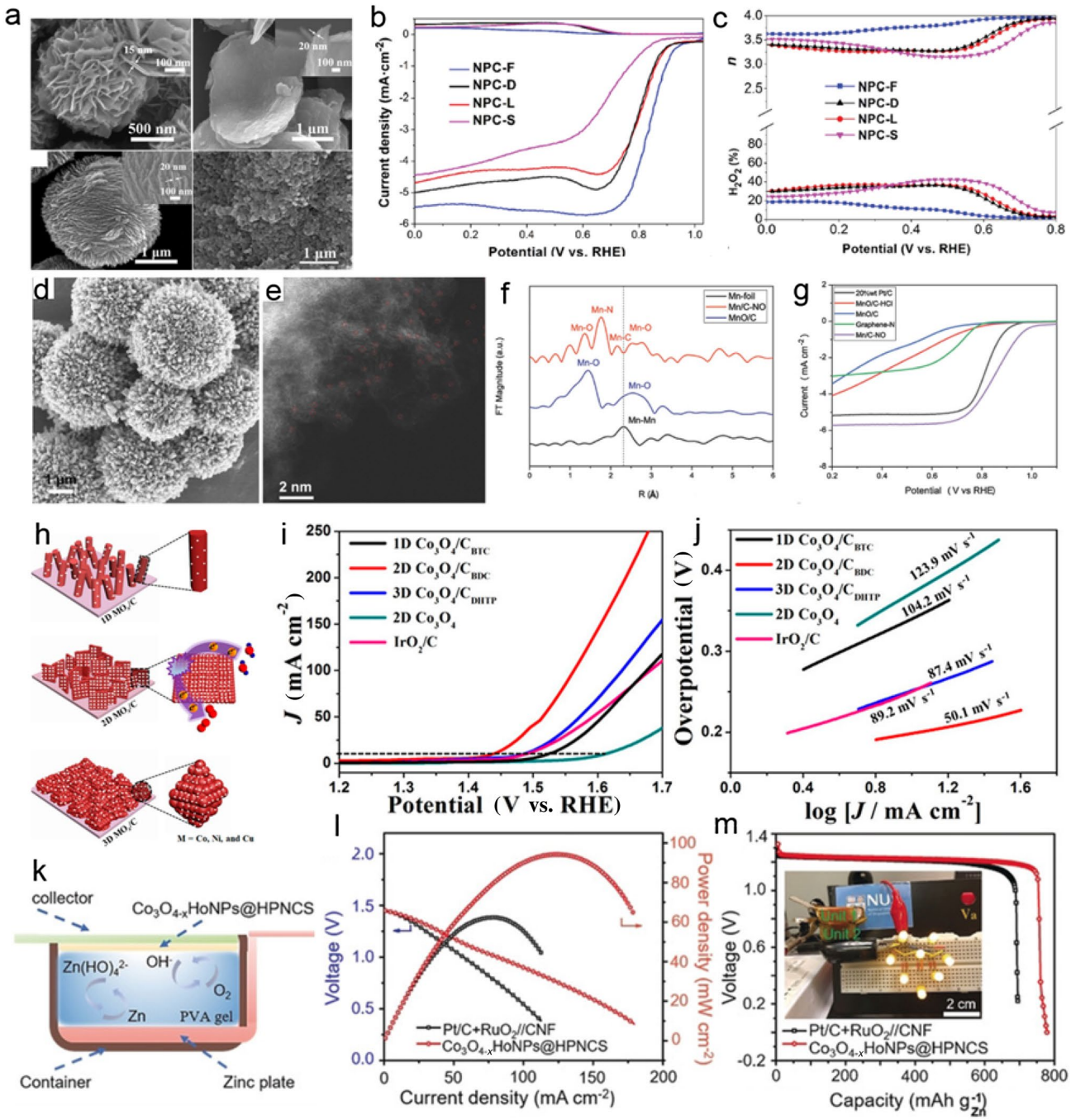

Fig. 18 3D HCMN-based electrocatalysts for ORR, OER and Zn-air batteries. N-doped porous carbon superstructures (NPCs) for ORR. **a** PI-derived carbon with various morphology, including flowers (NPC-F), disks (NPC-D), lanterns (NPC-L) and spheres (NPC-S). **b** Polarization curves, **c** electron transfer numbers and generated hydrogen peroxides of NPCs. Reprinted with permission from Ref [107]. Copyright © 2016, John Wiley and Sons. O and N atom coordinated Mn active sites dispersed on 3D graphene framework for ORR. **d** FESEM and **e** TEM images of Mn/C-NO showing atomically dispersed $MnNO_x$ active sites on hollow urchin-shaped carbon. **f** Mn K-edge EXAFS of Mn/C-NO, Mn foil and MnO/C. **g** Polarization curves of ORR catalysts. Reprinted with permission from Ref. [163]. Copyright © 2018, John Wiley and Sons. Metal oxide/carbon (MO_x/C, M = Co, Ni, and Cu) nanoarrays with 1D, 2D or 3D building units for OER. **h** Schematic of MOF-derived multidimensional MO_x/C arrays grown on Ni foil. **i** Polarization curves and **j** Tafel plots of 1D, 2D and 3D MO_x/C arrays as well as IrO_2 and 2D MO_x. Reprinted with permission from Ref. [361]. Copyright © 2018, American Chemical Society. Cobalt oxide hollow nanoparticle-embedded hierarchical porous carbon nanosheet arrays (Co_3O_{4-x} HoNPs@HPCNS) for portable Zn-air batteries. **k** Schematic of the home-made portable Zn-air battery, **l** discharge behaviors under different currents and corresponding power density curves, **m** voltage–capacity plots of portable Zn-air batteries based on Co_3O_{4-x} HoNPs@HPCNS or noble metal coupled cathodes. Inset of **m** shows the lighting LED applications of two Zn-air batteries. Reprinted with permission from Ref. [187]. Copyright © 2019, John Wiley and Sons

[174] constructed a N and S dual-doped honeycomb-like porous carbon structure embedded with Co_9S_8 nanoparticles through a MOF encapsulation–carbonization approach in which thiourea and $CoCl_2$ were homogeneously encapsulated into MOF internal pores and subsequently carbonized to 3D Co_9S_8/carbon hybrids. As such, the hybrid manifested optimal catalytic performances among cobalt sulfide-based catalysts for alkaline ORR, which can be attributed to the hierarchical honeycomb-like open structure with large surface area and pore volume as well as the suitable graphitization degree and high content of uniformly distributed active species with synergetic interactions. Li et al. [193] applied a MOF@ LDH derived Co-containing carbon superstructure with a nanoplate-supported honeycomb network for ORR in which MOF polyhedra were strongly immobilized on LDH and transformed into a carbon honeycomb network through pyrolysis. And with the resulting highly active sites including N–C and Co–N–C as well as a large surface area and hierarchical porous structure, the 3D Co/C hybrid showcased excellent ORR activities with a 0.94 V onset potential and 0.83 V half-wave potential along with long-term stability that surpassed Pt/C. Guan et al. [164] further prepared dual-MOF-derived porous carbon matrix supported N-doped CNT arrays embedded with iron carbide nanoparticles (Fe_3C@NCNT) as an advanced ORR electrocatalyst and reported that the dual-MOF precursor ensured the conformal space-confined carbonization of the MIL-88B nanorods to give rise to ultrasmall Fe_3C nanoparticles-embedded NCNTs without aggregation that cannot be attained through the direct pyrolysis of only MIL-88B. Consequently, the Fe_3C@NCNT possessed a hierarchical open structure as well as homogeneously dispersed ultrafine Fe_3C nanocrystals and a conductive porous carbon superstructure with rich N doping to allow for striking electrocatalytic ORR activities that were comparable to Pt/C in basic media.

single-atom catalysts Single-atom catalysts possessing unique coordination structures, optimal metal utilizations and unparalleled activity have been considered as potential alternatives to noble metal catalysts [356]. For example, by carbonizing MOF–guest composites, Zhu et al. [175] atomically dispersed N and Fe dopants into hierarchical porous carbon architectures in which the Fe K-edge of the extended X-ray absorption fine structure (EXAFS) data suggested a Fe–N shell with a coordination number of 2.7 and a bonding length of 2.01 Å, while Fe–Fe and Fe–C interactions were confirmed by both XANES and TEM characterizations. The interactions between metallic Fe and the FeNx coordination structure can benefit oxygen adsorption to enhance ORR catalytic activity. In addition, the 3D honeycomb-like open structure with its hierarchical pores and the fully exposed and atomically distributed high-density Fe-based active sites within the final sample can enable catalytic performances superior to commercial Pt/C and state-of-the-art noble-metal-free catalysts toward alkaline ORR in terms of onset and half-wave potential as well as durability. And although Mn-based catalytic sites are generally considered to be less efficient as compared with commonly known Fe- and Co-based active sites for ORR, natural Mn-based biocatalysts can achieve highly efficient oxygen reduction. Inspired by Mn cofactors in heme–copper oxygen reductases enzymes, Chen et al. [163] designed 3D carbon-supported atomically dispersed Mn-coordinated O and N active centers derived from Mn-based MOFs in which the atomic dispersion of Mn single sites onto the 3D urchin-shaped carbon superstructure was revealed using aberration-corrected high-angle annular dark-field scanning transmission electron microscopy (HAADF-STEM, Fig. 18d, e) and EXAFS (Fig. 18f). As a result, the biomimetic catalyst demonstrated exceptional alkaline ORR activity with a half-wave potential of 0.86 V that is superior to the Pt/C catalyst (0.82 V, Fig. 18g) and is ranked as one of the best Mn-based catalysts, which can be ascribed to the abundant single-atom Mn-N/O sites, the 3D hierarchical, hollow structure and the enhanced electrical conductivity from carbon encapsulation. DFT calculations further indicated that the d-electron orbitals of Mn can be modified through coordination with O and N atoms to accommodate reasonable electronic interactions with oxygen-bearing intermediates including O*, OH* and OOH* and therefore improve catalytic performance. In particular, the Mn-N_3O_1 active sites demonstrated the fastest ORR kinetics and highest activity.

8.1.2 OER and Bifunctional Catalysts for Zn-Air Batteries

Due to the use of mild zinc metals and water-based electrolytes (e.g., 6 M KOH), Zn-air batteries with an ultrahigh theoretical energy density of 1084 Wh kg^{-1} are regarded as cheap, safe and environmentally friendly energy storage systems [357, 358]. In terms of the development of rechargeable Zn-air batteries, both ORR during discharge and sluggish oxygen evolution reactions (OER) during charge need to be addressed. Similar to ORR, optimal OER catalysts are based on precious metals such as IrO_2 and RuO_2 in which the replacement of these noble metals is required for commercialization. In addition, practical metal-air batteries require active and durable air electrodes toward both ORR and OER in the form of bifunctional catalysts. Based on this, enormous efforts have been devoted to the search for earth abundant and cost-effective OER and ORR/OER bifunctional catalysts with high activity and stability. Among these, 3D HCMNs derived from different sources have been intensively investigated as not only metal-free active catalysts, but also robust catalyst supports for other components including metal, metal oxide, metal hydroxide and even single-atom catalysts [354, 355, 357, 359].

3D g-C_3N_4 Catalysts Ma et al. [141] prepared a metal-free 3D g-C_3N_4-based flexible bifunctional electrocatalyst for an oxygen electrode through the direct growth of phosphorus-doped g-C_3N_4 (P-g-C_3N_4) on carbon fiber paper (CFP) to result in a P-g-C_3N_4 with a nanoflower structure composed of thin nanosheets (~3 nm thickness) strongly coupled with CFP to afford a 3D hierarchical hybrid with substantial N and P doping (N: 13.2 wt%; P: 0.9 wt%) as well as superb catalytic activity (reversible oxygen overpotential of 0.96 V) and durability towards ORR and OER that are superior to P-free counterpart (1.06 V) and CFP-supported Pt catalyst (1.02 V). The extraordinary activity, stability and reversibility of the freestanding PCN–CFP also enabled its immediate application as an air cathode in Zn–air batteries to achieve low overpotentials and long-term cycling.

GDY-based catalysts GDY can also act as efficient catalyst supports for OER-active components. Take the Cu foam-supported GDY nanowalls as an example, Li et al. [78] took into consideration the strong interactions between metal species and conjugated structures to chemically reduce cobalt ions in the presence of GDY to Co to obtain a self-supported Co-loaded GDY catalyst and reported that the prepared 3D Cu@GDY/Co electrode exhibited superb OER activities with a small overpotential of 300 mV and a high mass activity of 413 A g^{-1} at 1.60 V versus RHE in which during 4 h of electrolysis, a constant current density was maintained to indicate high stability.

MOF superstructure-derived catalysts Lou et al. [38] proposed a general MOF-derived strategy to synthesize 3D hollow frameworks with N-doped CNTs as a bifunctional electrocatalyst for ORR and OER. The resulting 3D carbon displayed outstanding catalytic activities and durability that outperformed commercial Pt/C, which these researchers attributed to the high content of active sites including N dopants and carbon defects, proper electronic interactions between residual metallic Co nanoparticles and CNTs, a 3D hierarchical porous hollow structure with high surface area and a robust framework composed of numerous CNTs with excellent conductivity and corrosion resistance. Similarly, Xu et al. [360] synthesized a hydrangea-like N-doped carbon superstructure through the morphology-maintained thermal conversion of core@shell Zn/Co-based MOFs. Here, these researchers further introduced guest Fe ions into the core@shell MOF precursor to act as catalysts for the in situ growth of CNT networks onto the carbon superstructure during co-pyrolysis, resulting in a highly opened-up structure with catalytically active sites based on Fe and Co nanoparticles and Fe, Co–N_x species with synergetic effects between Fe and Co to enable efficient bifunctional catalysis for both OER and ORR. Based on this, a corresponding Zn-air battery provided an ultrahigh power density of 190.3 mW cm^{-2} and a large capacity of 787.9 mAh g_{Zn}^{-1} equal to an energy density of 1012 Wh kg_{Zn}^{-1}.

MOF nanoarray-derived catalysts Although promising for OER electrocatalysts, pure transition metal oxides with low electrical conductivity and deficient active sites, show limited activity. To address this, the embedding of these oxides into highly open and conductive carbon supports can enhance OER performance. For example, Zhou et al. [361] derived a family of highly oriented nanoarrays of 1D, 2D and 3D MO_x/C (M = Co, Ni, and Cu) from MOFs for OER (Fig. 18h) and reported that for Co_3O_4/C arrays, corresponding polarization curves (Fig. 18i) and Tafel plots (Fig. 18j) clearly indicated a catalytic activity trend in terms of η_{10} and the Tafel slope to follow: 2D Co_3O_4/C (208 mV, 50.1 mV dec^{-1}) > 3D Co_3O_4/C (260 mV, 87.4 mV dec^{-1}) > IrO_2 (265 mV, 89.2 mV dec^{-1}) > 1D Co_3O_4/C (295 mV, 104.2 mV dec^{-1}) > 2D Co_3O_4 (370 mV, 123.9 mV dec^{-1}), which demonstrated the superiority of 2D building blocks as compared with 3D or 1D building blocks as well as the significance of conductive carbon supports with high exposure. Of note, all of these nanoarrays possess 3D structures but contain either 1D, 2D or 3D nanostructured building blocks.

Guo et al. [186] further reported a facile and scalable "impregnation-carbonization-acidification" strategy to prepare carbon fiber paper-supported vertical carbon flake arrays anchored with single metal atoms (including Co and Ni) as a freestanding dual-functional electrocatalyst for ORR and OER using MOFs and electrospun PAN fibers as precursors. Due to the enhanced accessibility of active sites and optimized correlations within the single-sites/pore structures, a low reversible oxygen overpotential of only 0.75 V and high durability was achieved in the resulting Co single site-decorated 3D carbon catalyst. DFT calculations further indicated that the single-atom coordination sites possessed a lower OH* hydrogenation barrier than the cluster configuration, which accounted for the superb oxygen catalytic activity of the single sites. And as a binder-free flexible electrode in a wearable Zn-air battery, this catalyst enabled a high capacity of 530.17 mAh g_{zn}^{-1} as well as deformable capability and great potential in the integrated system.

The same group further modified a 3D catalyst for oxygen reactions through Kirkendall effect-induced vacancy defect engineering [187] in which the Kirkendall effect is a classical phenomenon to form hollow nanostructures due to differential diffusion rates in solid-state reactants. Different from the previous study in which metal nanoparticles were converted into single metal sites, the Co in this study was transformed into an O-vacancy-rich Co_3O_{4-x} hollow structure embedded in hierarchical porous carbon nanosheet arrays (HPCNS) through low-temperature oxidation. The regulation of the Kirkendall oxidation degree allowed for the tuning of the oxygen vacancy defect concentration and therefore the number of active sites and the catalytic performance. As a result, the optimized Co_3O_{4-x} HoNPs@HPCNS catalyst presented one of smallest reversible oxygen overpotentials of

0.74 V in the catalysis of alkaline ORR and OER to achieve enhanced performance in a custom designed portable solid-state Zn-air battery (Fig. 18k), enabling stable cycling performances, higher power densities (94.1 vs. 62.7 mW cm^{-2}, Fig. 18l) and larger capacities (779.4 vs. 708.5 mAh g_{zn}^{-1}, Fig. 18m) that surpassed noble metal catalysts.

Similar to the preparation of 3D carbon-supported hollow Co_3O_4, Guan et al. [185] prepared hollow and porous $NiCo_2O_4$/C nanowall arrays on flexible CC through an ion exchange process and reported that due to the highly hollow and porous structure, the flexible and conductive CC and the large surface area vertical arrays, the resulting binder-free carbon-supported $NiCo_2O_4$/C nanowall arrays demonstrated superior OER performances in terms of onset potential (1.49 V) and stability. Aside from the synthesis of hollow structures, the same strategy can also be employed to prepare N-doped ultrafine Co_3O_4 nanoparticles (4–5 nm) immobilized in vertical porous carbon sheet arrays supported on CC with a high surface area (173 m^2 g^{-1}) and a rich N dopant (~3 at%),;Wang et al. [188] reported that their as-made 3D catalyst was able to present a superhigh half-wave potential of ~0.9 V for alkaline ORR and a low overpotential of 330 mV at 10 mA cm^{-2} for alkaline OER, which amounted to a record low oxygen overpotential gap of 0.66 V. And when directly applied in an all-solid-state flexible zinc-air battery, the 3D electrode achieved ultrahigh power densities of 200 mW cm^{-2} and 99.8 mW cm^{-3} together with an ultralong cycle life of 400 h (1200 cycles) that were much better than previous results.

8.1.3 HER and Bifunctional Catalysts for Water Electrolyzers

Water electrolysis is regarded as a promising technology to generate hydrogen fuel because of its high purity, zero emission and easy integration with other energy conversion devices, including solar cells and thermoelectric devices [362, 363]. Fundamentally, water electrolyzers consist of a hydrogen-generating cathode and an oxygen-generating anode and involve hydrogen and oxygen reactions (HER and OER) that require catalysts to enhance sluggish kinetics [364]. And although HER is faster than OER, catalysts are still required in which similar to ORR and OER, optimal HER electrocatalysts are currently based on noble metals, especially Pt. Because of this, the development of active, durable and inexpensive HER catalysts based on non-noble metals is vital for the wide deployment of water electrolyzers. To address this, researchers have intensively explored transition metal-based catalysts with appropriate structures, sizes and composition to optimize hydrogen/oxygen binding energy for water splitting [365, 366]. Among these, molybdenum-based catalysts such as MoS_2 and Mo_2C have garnered tremendous attention as HER catalysts due to Pt-like electronic structures and wide-pH-range catalytic performances [367]. Despite this, corresponding catalytic HER activities remain inferior to most advanced catalysts, mostly due to aggregation issues and low conductivity. The homogeneous dispersion of these catalysts onto carbon supports with open structures has proven effective in the enhancement of catalytic activity and stability.

MoS_x For example, Smith et al. [368] grew MoS_x onto 3D modified carbon substrates as HER catalysts in which crumpled graphene can act as a surface area enhancer for 3D electrode substrates such as CC to facilitate the homogeneous growth of MoS_x, resulting in MoS_x grown on crumpled-graphene-modified CC achieving a current density of 220 mA cm^{-2} at an overpotential of 0.3 V, which is superior to MoS_x grown on unmodified CC at the same loading. In another example, Wang et al. [241] grew vertical graphene nanosheet arrays loaded with MoS_2 nano-leaves onto graphite through CVD combined with solvothermal treatment and reported that due to the 3D VG/MoS_2 nanoarchitecture-enabled mechanical robustness along with exposed defect sites, improved electrolyte accessibility and reduced ion diffusion lengths, the resulting hybrid demonstrated highly efficient HER catalysis with a low Tafel slope of 41.3 mV dec^{-1} and a good double-layer capacitance of 7.96 mF cm^{-2}.

Mo_2C As for Mo_2C, this catalyst material has been grown on various 3D carbon supports to enhance HER performance. For example, Lou et al. [126] constructed hierarchical Mo_2C tubes from ultrathin nanosheets derived from cooperative self-assembled Mo-PDA precursors and reported that due to nanosized crystals, highly exposed active sites, rapid charge transfer and delicate tubular superstructure, the as-obtained hierarchical Mo_2C tubes experienced small HER overpotentials in both acid and base media together with acceptable stability. Similarly, Huang et al. [128] carbonized Mo-PDA flower-like assemblies to uniformly distribute ultrasmall Mo_2C nanoparticles on hierarchical carbon flowers, and the resulting catalyst showed impressive activity with small overpotentials, low Tafel slopes and superb stability that were among the best for non-noble HER catalysts in which the high performance was ascribed to the fully open and accessible 3D structure with hierarchical ordering at different levels. In another example, Xu et al. [369] adopted an assembly-carburization-leaching approach to obtain hierarchical nanohybrids of Mo_2C nanoparticle-decorated N-doped carbon tube-sheet superstructures (Mo_2C/CTSSs, Fig. 19a–c) in which the simple adjustment of assembly conditions can allow for the arrangement of vertical nanosheet arrays (periodic vs. random) in the carbon superstructures along with enhanced catalytic activity (Fig. 19a). As a result, as-obtained Mo_2C/CTSS nanohybrid comprised of regularly patterned vertical carbon nanosheet arrays with rich N doping and hierarchical pores demonstrated small overpotentials and low Tafel slopes in both acidic (97 mV,

48 mV dec^{-1}) and basic media (95 mV, 54 mV $decade^{-1}$) that were comparable to state-of-the-art catalysts and better than counterparts with randomly arranged carbon nanosheet arrays (Fig. 19b, c) in which the superiority of periodicity over randomness was thought to be a result of the higher exposed electroactive surface area and more favorable mass and charge transport. Late transition metals such as Fe, Co and Ni were also found to be effective activity enhancers for Mo_2C catalysts toward HER due to modified electronic structures and additional active sites in Mo_2C-metal interfaces. Based on this, Wang et al. [127] fabricated flower structured Ni-doped Mo_2C/carbon hybrids through the conversion of self-assembled Ni-Mo-PDA complexes and reported that due to Ni doping with additional active sites and enhanced electrical conductivities, the Ni-doped Mo_2C/carbon hybrid provided better performances than Mo_2C without Ni doping.

Metal carbide Other 3D carbon-supported metal carbides have further been explored for application in water electrolysis. For example, Fan et al. [370] decorated single crystalline tungsten carbide (WC) nanoparticles (size: 4.5–21.6 nm) onto the tips of VACNTs through direct reaction between W and carbon precursors in a hot filament CVD furnace and reported that due to the homogeneously distributed ultrafine WC nanocrystals on the open-ended carbon support with fully exposed active sites, the resulting 3D WC–CNT hybrid provided remarkable HER catalytic activities with onset potential, η_{10} and Tafel slope values of 15 mV, 145 mV and 72 mV dec^{-1} in acidic electrolyte as well as 16 mV, 137 mV and 106 mV dec^{-1} in basic electrolytes, respectively, along with robust durability without oxidation or corrosion. Using the same strategy, Fan et al. [371] embedded Fe_3C, Co_3C and Ni_3C nanocrystals into graphitic shells comprised of vertically aligned graphene nanoribbons (GNR) and reported that the resulting Fe_3C-GNR, Co_3C-GNR and Ni_3C-GNR catalysts exhibited excellent acidic HER activities with low onset overpotentials of 32, 41 and 35 mV as well as small Tafel slopes of 46, 57 and 54 mV dec^{-1}, respectively, accompanied by good stability. Salt-template-generated vertical graphitic carbon-supported metal carbides including $MoC_{0.654}$, WC, TaC and NbC have also shown activity toward HER [203].

Metal and alloys In terms of metal and alloys, these have further been loaded onto 3D carbon materials as highly efficient HER catalysts. For example, Li et al. [71] proposed a GDY-based 3D structure for HER catalysis involving Cu foam-supported core–shell arrays with Cu nanowires as the core and GDY nanosheets as the shell and reported that the 3D electrode provided high acidic HER activities with a low onset overpotential of 52 mV, a Tafel slope of 69 mV dec^{-1} and small overpotentials of 79 mV and 162 mV to generate current densities of 10 and 100 mA cm^{-2}, respectively, as well as long-term stability of ~ 20 h that were much better than counterparts such as Cu nanowire arrays and GDY nanosheet arrays on Cu foam in which the active sites were determined to be the hybrid coordination between GDY and Cu. Alternatively, Chen et al. [40] combined 0D ultrafine Co nanoparticles with 1D N-doped CNTs and 2D graphene into a 3D hierarchical structure through the carbonization of GO-wrapped core–shell bimetallic (Co, Zn) MOFs. The resulting 3D composite was able to demonstrate a current density of 10 mA cm^{-2} at overpotentials of only 108 and 87 mV in alkaline and acidic media, respectively, which were better than previously reported Co-based HER catalysts. Moreover, the strategy was universally applicable to the synthesis of 3D rGO@NCNT-supported transition metals, binary and even ternary alloys toward efficient HER. In particular, a 3D carbon-based Co-Fe hybrid delivered performances of 10 mA cm^{-2} at 86 mV in 1.0 m KOH and 74 mV in 0.5 M H_2SO_4, which were among the best in HER electrocatalysts.

Overall, practical water electrolyzers should possess efficiently coupled HER and OER catalysts. However, electrolytes for HER or OER catalysts are often incompatible (acid vs. base), which complicates the electrolyzer assembly process. And although some catalysts can demonstrate bifunctional activity for HER/OER in the same electrolyte, their composition is quite different and can cause mutual influences during catalytic reactions as induced by the dissolution and redeposition of metal species [372]. Consequently, the preparation of bifunctional catalysts with minimal mutual interferences for water electrolysis is critical. Based on this, Si et al. [79] developed a 3D hierarchical GDY@NiFe layered double hydroxide (LDH) heterostructured catalyst toward overall water splitting through the coupling of NiFe LDH and GDY growth on Cu foam (CF, Fig. 19d). The electrocatalyst exhibited high activities for both OER and HER with overpotentials of 220 mV and 163 mV at 10 mA cm^{-2}, respectively, as well as an OER Tafel slope of 39.33 mV dec^{-1} that was much lower than that of NiFe LDH/CF (112 mV dec^{-1}), resulting in the heterostructured GDY@NiFe LDH electrocatalyst providing high activity toward overall water splitting with a current density of 20 mA cm^{-2} at 1.512 V (Fig. 19e). For 10 h of continuous electrolysis (Fig. 19f), the electrolyzer did not require higher potentials to maintain current based on chronopotentiometry results, but that lower potentials can actually meet demand, possibly due to catalyst activation. DFT calculations further indicated that synergetic effects arising from transition metal 3d orbitals and GDY carbon–carbon triple bonds were responsible for the bifunctional electrocatalytic activity.

In another example, Duan et al. [184] grew NiFe-MOF nanosheet arrays onto Ni foam for water splitting in which the catalyst was tested in 0.1 M KOH without iR-correction to report that the obtained catalyst can provide an OER overpotential of 240 mV at 10 mA cm^{-2} and a Tafel slope of 34 mV dec^{-1} that were much smaller than the Ni-MOF, the

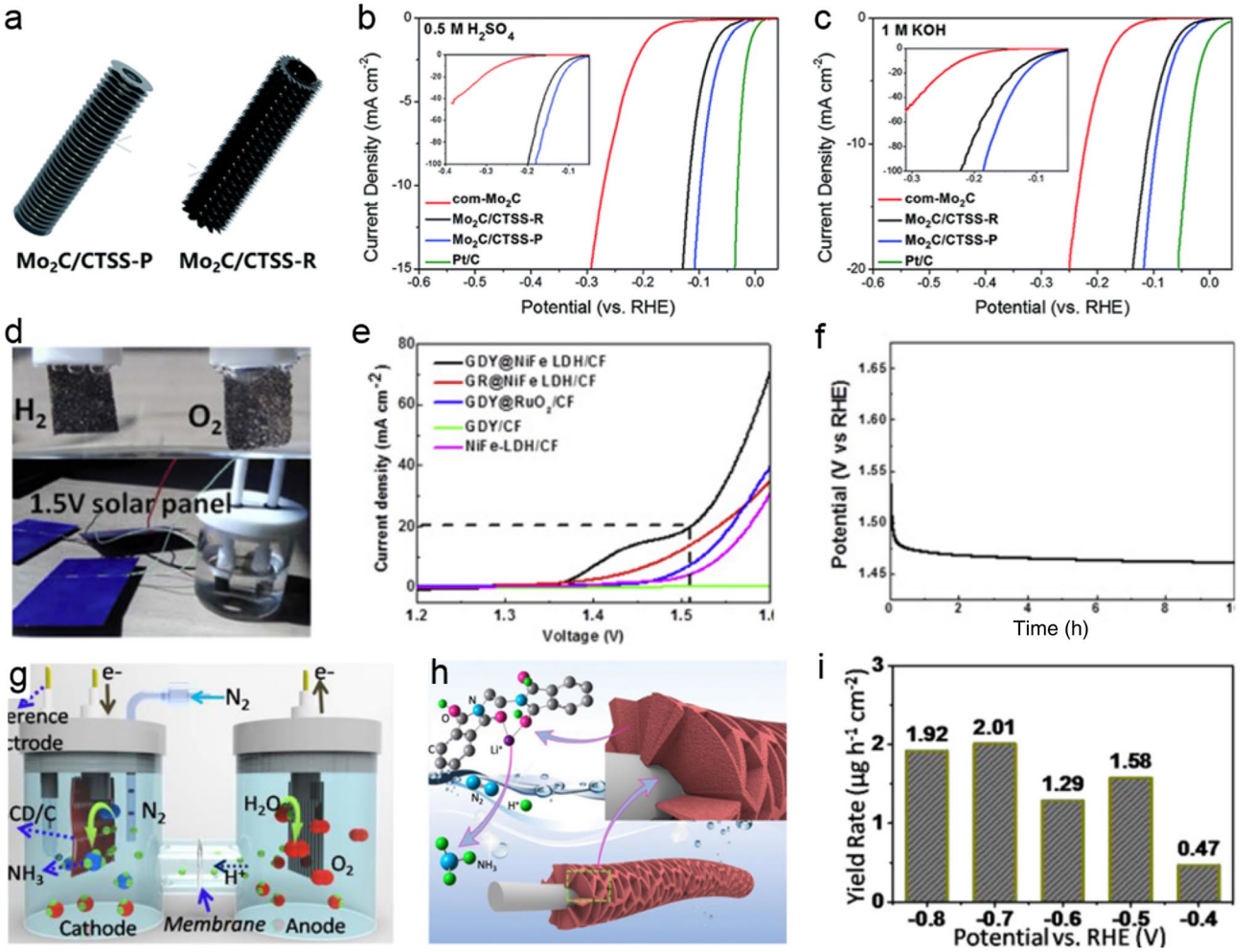

Fig. 19 3D HCMN-based electrocatalysts for HER, water electrolysis and NRR. Mo_2C/carbon tube sheet superstructured nanohybrids (Mo_2C/CTSSs) with controllable carbon nanosheet arrays for HER. **a** Models for Mo_2C/CTSS-P with periodic patterned nanosheets (left) and Mo_2C/CTSS-R with randomly arranged nanosheets (right). HER performance of Mo_2C/CTSS-P, Mo_2C/CTSS-R, commercial Mo_2C and Pt/C in **b** acidic and **c** alkaline media. Reprinted with permission from Ref. [369]. Copyright © 2018, Royal Society of Chemistry. Cu foam-supported GDY nanowall arrays coupled with NiFe LDH (GDY@NiFe LDH/CF) for overall water splitting. **d** Integrated device with the solar cell-driven water electrolyzer. **e** Polarization curves of different catalysts toward water electrolysis. **f** Chronopotentiometry data of GDY@NiFe LDH/CF during 10 h. Reprinted with permission from Ref. [79]. Copyright © 2019, Elsevier. Li^+ coordinated PI nanosheet arrays for NRR. **g** Electrolytic cell for NRR. **h** Scheme illustrating the Li^+-incorporated PI as active sites to convert N_2 into NH_3. **i** NH_3 yield rates of Li^+ coordinated PI catalysts at various potentials. Reprinted with permission from Ref. [119]. Copyright © 2017, American Chemical Society

Fe-MOF/NF, the powdery NiFe-MOF loaded NF, the carbonized NiFe-MOF and even IrO_2. Negligible activity loss was also experienced after 20000 s of operation, indicating good stability. The 3D NiFe-MOF/NF further possessed a TOF of 3.8 s^{-1} as compared with IrO_2 with only 0.14 s^{-1}, indicating much higher catalytic efficiency that was among the best for reported OER electrocatalysts. Moreover, the 3D NiFe-MOF/NF presented high activity and efficiency toward HER with an overpotential of 134 mV at 10 mA cm^{-2} and a TOF of 2.8 s^{-1}. As a result, a corresponding water electrolyzer only required 1.55 V to drive 10 mA cm^{-2} current, which was 70 mV smaller than noble Pt/C//IrO_2 couple catalysts. Here, these researchers attributed the ultrahigh performance of the 3D NiFe-MOF/NF for water splitting to the ultrathin MOF sheets (~3.5 nm) with high conductivity and vertically oriented arrays with hierarchical porosity as well as the macroporous Ni foam that can accelerate electrolyte and gas transport and the open pores between vertically aligned nanosheets together with mesopores and micropores from MOFs that can provide easily accessible active sites with short ion diffusion distances.

Chen et al. [40] further used N-doped carbon nanosheet arrays end-grafted with hollow carbon polyhedra grown on CC as a 3D carbon support for ultrafine Co nanoparticles

for water electrolysis and reported that the resulting electrocatalyst was able to manifest better HER and OER activities than the majority of documented transition metal-based catalysts in which an alkaline electrolyzer based on this bifunctional catalyst generated a current density of 10 mA cm^{-2} at 1.545 V that outperformed that of noble metal catalysts (Pt/IrO_2, 1.592 V). The remarkable performance can be ascribed to the hierarchical structure with 0D ultrasmall Co nanocrystals, 1D carbon fiber network, 2D N-doped carbon nanoflakes and 3D hollow carbon, all of which led to exposed active sites, strong structural durability, accelerated mass transport and enhanced charge transfer.

Metal oxide@MOF or metal hydroxide@MOF grown on conductive substrates can also be converted to carbon-based metal oxide hierarchical arrays as self-supporting catalysts for water electrolysis. For example, Cai et al. [191] used thermal pyrolysis to convert ZIF-67 coated CoO@Ni foam (Ni@CoO@ZIF-67) to Co nanoparticle-embedded N-doped porous carbon coatings on CoO nanofiber arrays grown on Ni foam and reported that the resulting Ni@CoO@Co-NC can be directly applied as a bifunctional catalyst for water electrolysis to achieve much better activity and stability toward OER and HER as compared with corresponding counterparts with single components or lacking self-supporting structures. Here, these researchers attributed the superior performance to the hierarchical porous structure of the 3D arrays as well as the synergistic coupling between the metal oxide and the MOF-derived carbon framework.

8.1.4 NRR

Ammonia as a crucial feedstock for agricultural, pharmaceutical and textile industries is synthesized industrially through the Haber–Bosch process [373]. However, high CO_2 emissions and harsh synthetic conditions hinder sustainable development. To address this, the electrocatalytic nitrogen reduction reaction (NRR) has been developed to synthesize ammonia in a clean and environmentally friendly manner [374], but requires efficient electrocatalysts with high Faradic efficiency and selectivity for the industrial application of electrochemical NH_3 synthesis.

In terms of 3D HCMNs, Chen et al. [119] grew vertically oriented PI nanosheet arrays onto CC as an NRR electrocatalyst in 0.5 M Li_2SO_4 (Fig. 19g, h) and reported that the incorporation of Li^+ into the carbonyl groups of PI to form O-Li^+ active sites can play a crucial role in inhibiting HER and boosting N_2 adsorption to allow for a wide voltage window for NRR with high selectivity following the "[O–Li^+]·N_2–H_x" alternating hydrogenation mode (Fig. 19h). And as a result of the highly exposed active sites on the 3D framework, optimal electrocatalytic performances were achieved at a potential of −0.5 V with Faradaic efficiency of 2.85% and a NH_3 yield rate of 1.58 μg h^{-1} cm^{-2} (Fig. 19i). In another example, Lin et al. [375] constructed an inorganic metal/organic semiconductor Mott–Schottky interface to boost NRR in basic solutions with high selectivity and activity by loading Cu nanoparticles onto a flower-like PI structure in which the Mott–Schottky effect can modify the electronic Cu/PI interfacial structure to achieve electron-deficient Cu nanoparticles and enable the preferred adsorption of OH^- to inhibit HER and enhance N_2 pre-adsorption, resulting in a high NH_3 yield rate of ~ 17.2 μg h^{-1} cm^{-2} and a claimed record-high turnover frequency of ~ 0.26 h^{-1}, which is even higher than that of noble metal catalysts.

8.2 Photo(electro)catalysis

Photoelectrochemical water splitting is a promising and environmentally friendly method to address the current energy crisis because it can integrate the collection and conversion of solar energy into photocathodes and photoanodes in which electrons and holes can be collected to produce hydrogen and oxygen, respectively [376]. On the other hand, heterogeneous photocatalytic reduction and oxidation reactions based largely on photocatalysts and sunlight have recently attracted extensive interest in the fields of energy, catalysis and environment [14], resulting in the development of numerous photo(electro)catalysts in the past decades such as Si, MoS_2, CdSe, $BiVO_4$ and g-C_3N_4 [376]. Despite this, current catalysts cannot fully satisfy requirements for practical application such as enhanced safety, reduced cost, high efficiency, small band gaps and long-term stability as well as prolonged photogenerated charge [13]. Because of this, there is an urgent need to develop highly efficient and stable visible light-driven photo(electro)catalysts through the optimization of methodologies such as carbon coupling, cocatalyst addition and heterojunction construction. [14] Coupling with 3D hierarchical carbon supports is beneficial for exposing active surface areas, enhancing electric conductivity, harvesting light energy, and is therefore widely employed to improve photo(electro)catalytic performance.

Although Si nanowire (SiNW)-based photoelectrochemical conversion can provide high efficiency as compared with other semiconductors, Si faces surface oxidation and corrosion in liquid electrolytes. To address this, Hong et al. [377] grew carbon nanowires (CNWs) onto a SiNW electrode with Cu vapor as the catalyst through CVD to obtain a hierarchical branch structure similar to a tree and reported that the small-sized SiNWs enabled efficient charge separation and minimized carrier diffusion to the surface before recombination. The hierarchical CNW-SiNW heterostructure can provide additional surface area to enhance access to the electrolyte, which together with the high conductivity of the CNWs can reduce diffusion pathways for photogenerated carriers, allowing the hierarchical CNW-SiNW

heterostructure to demonstrate increased photocurrents, smaller overpotentials and better cyclability for photocatalytic hydrogen production.

MoS_2 as an environmentally friendly and abundant semiconductor has also been intensively studied as a replacement of Pt in HER; however, poor conductivity restricts further activity improvements. To address this, Carraro et al. [378] fabricated hierarchical nanohybrids composed of N-doped crumpled graphene decorated with uniformly distributed MoS_2 nanoparticles for photoelectrochemical hydrogen generation through a fast and facile aerosol processing method; the resulting 3D N-doped graphene/MoS_2 nanohybrid enabled a sevenfold enhancement in activity as compared with pure MoS_2, which can be attributed to the generation of p–n MoS_2/N-doped graphene nanojunctions, the aggregation-resistant dispersion and smaller size distribution of MoS_2 and the efficient charge carrier separation as a result of N doping and the 3D graphene structure.

GDY nanowall arrays as a hole transportation layer were firstly applied by Wu et al. for photoelectrochemical hydrogen production in neutral water in which CdSe quantum dots were decorated onto GDY nanowalls to act as a photocatalyst with the spontaneous injection of photoexcited holes from CdSe into GDY based on the valence band positions of the CdSe quantum dots (~ 1.23 V vs. NHE) and GDY (~ 1.05 V vs. NHE) [77]. In addition, spectroscopic results indicated strong π–π interactions between GDY and surface-functionalized CdSe quantum dots that can facilitate hole transfer and enhance generated photocurrent, resulting in the CdSe/GDY photocathode delivering ~ − 70 μA cm^{-2} photocurrent in neutral electrolytes at an potential of 0 V versus NHE, a hydrogen yield of 27 mmol h^{-1} g^{-1} cm^{-2} at −0.20 V along with high Faradic efficiency up to 95% and good stability over 12 h under Xe lamp irradiation. GDY nanowalls were also constructed on $BiVO_4$ electrodes to fabricate a GDY/$BiVO_4$ composite photoanode in which the GDY nanoarrays can again rapidly capture photoexcited holes to prevent charge recombination and allow for significantly enhanced photoelectrochemical activity and stability in comparison with single $BiVO_4$ photoanodes [75].

A metal-free heterojunction of g-C_3N_4/GDY involving g-C_3N_4 nanosheets anchored onto vertical GDY nanowall arrays was constructed through solvothermal treatment to function as a composite photocathode for photoelectrochemical hydrogen generation in neutral media (Fig. 20a) [379]. Due to the suitable band structures of g-C_3N_4 and GDY, photoexcited holes from g-C_3N_4 can be injected into GDY to facilitate hole transfer (Fig. 20b). And based on the obtained open circuit potential plot (Fig. 20c), an increased potential from 37 mV to 66 mV was detected for g-C_3N_4/GDY under light radiation. The g-C_3N_4/GDY hybrid also achieved a sevenfold enhancement in the electron lifetime (610 μs) as compared with g-C_3N_4 (88 μs) as well as an ultrahigh photocurrent of −98 μA cm^{-2} at 0 V versus NHE that was more than three times that of a g-C_3N_4 photocathode (−32 μA cm^{-2}, Fig. 20d). These researchers also reported that the catalytic activity can further be increased through the use of a Pt cocatalyst to enable a record-high photocurrent of −133 μA cm^{-2} and suggested that the high catalytic activity of the g-C_3N_4/GDY heterostructure can be attributed to its corresponding structural features, including the ultrathin structure of the g-C_3N_4/GDY that can shorten photocarriers transport distance and enhance efficient hole injection from g-C_3N_4 to GDY, the high hole mobility of GDY that can enhance hole transfer rate and therefore efficiently restrain photocarrier recombination in g-C_3N_4, the nanosheet array and large surface area of GDY that can enhance active site exposure for photoelectrocatalysis and the enriched N atoms in g-C_3N_4 that can easily couple with cocatalysts for the dual control of photo-induced electrons and holes.

g-C_3N_4 is also a promising metal-free photocatalyst for solar energy conversion and pollutant photodegradation with corresponding catalytic performances being adjustable through the modification of structural, optical and electronic properties based on methods such as doping, copolymerization and structural engineering. For example, Jun et al. [136, 137] proposed a molecular cooperative assembly strategy to synthesize a series of 3D g-CN catalysts for photocatalysis and reported that the 3D hierarchical mesoporous structure of graphitic carbon nitride inherited from melamine cyanuric acid complexes can induce better light absorption, widen optical bandgaps and prolong the lifetime of photogenerated carriers as compared with bulk g-CN [136]. When applied for dye photodegradation, the 3D g-CN can allow for a tenfold enhancement in rhodamine B photodegradation kinetics under visible light irradiation in comparison with bulk g-CN. The same group [137] further investigated the influence of temperature, solvent and monomer on molecular cooperative assembly and subsequent photocatalytic hydrogen evolution and reported that the optimized 3D g-CN can provide a tenfold enhancement in photocurrent and a ninefold improvement in quantum efficiency (~ 2.3%) as compared with g-CN synthesized from melamine without cooperative assembly.

In another example, Wang et al. [139] prepared nanospherical g-C_3N_4 (NS-g-C_3N_4) with a highly open 3D flower structure constructed from sharp-edged nanosheets for photocatalytic hydrogen generation (Fig. 20e) and evaluated the photocatalytic activities of NS-g-C_3N_4 and different structured g-C_3N_4 control samples including hollow g-C_3N_4 nanospheres (HCNS), g-C_3N_4 nanosheets, bulk-g-C_3N_4, structurally deformed NS-g-C_3N_4 and mpg-C_3N_4 (of comparable surface area and optical absorption properties to NS-g-C_3N_4) in which Pt nanoparticles as a cocatalyst were deposited onto the samples before testing. Here, these researchers reported that an optimal H_2 generation rate of 574 μmol h^{-1} can be obtained based on 3 wt%

Pt/NS-g-C_3N_4 (1) that significantly outperformed 3 wt% Pt loaded bulk-g-C_3N_4 (2, 12.5 μmol h^{-1}), mpg-C_3N_4 (3, 123 μmol h^{-1}), HCNS (4, 319 μmol h^{-1}), g-C_3N_4 nanosheets (5, 98 μmol h^{-1}) and deformed NS-g-C_3N_4 (6 & 7) (Fig. 20f) and that g-C_3N_4 loaded with 3 wt% Pt possessed considerably enhanced catalytic performances with a record-high apparent quantum yield (AQY) of 9.6% at 420 nm that were better than other samples, all of which suggested that apart from enlarged surface areas and enhanced light harvesting, the engineering of well-defined 2D nanosheets into highly open 3D structures is of great significance and can realize synergistic effects for photocatalysis. They further reported that wavelength-dependent H_2 yield rates of 3 wt% Pt/NS-g-C_3N_4 showed the same trend as the absorption spectrum, implying a photoexcited electron-dominated hydrogen evolution process (Fig. 20g). Yuan et al. [140] further synthesized mesoporous P-doped flower-shaped g-C_3N_4 through the condensation reaction between melamine and diphosphosnic acid followed by thermal annealing in which P doping allowed for the retention of the g-C_3N_4 polymeric framework but significantly modified the electronic structure to show red-shifted light absorption and enhanced electronic conductivity. As a result, the obtained 3D structure with in-plane mesopores and nanosheet construction units provided a high surface area for enhanced active site exposure and in conjunction with P doping can enhance light harvesting, matter transfer and charge separation to enable outstanding photocatalytic water reduction with a hydrogen yield of 104.1 μmol h^{-1} that significantly surpassed pristine bulk g-C_3N_4 (11.2 μmol h^{-1}). Xu et al. [380] fabricated 3D hierarchical g-C_3N_4 superstructures assembled with ultrathin (5–6 nm) nanosheets for photocatalytic hydrogen evolution through an easily scalable hexamethylenetetramine activation approach and reported that the resulting 3D structure of the nanosheet building units allowed for strong light absorption, adjustable band gaps, good electrical conductivity, rapid charge splitting and high surface areas with rich active sites to provide a high quantum efficiency of ~ 7.8% and a H_2 yield rate of more than 2.7×10^4 μmol g^{-1} h^{-1} that was over 30 times that of inactivated g-C_3N_4.

9 Summary and Perspective

3D hierarchical carbon-rich micro/nanomaterials with diverse superstructures and nanoarrays (urchins, flowers, hierarchical tubes and multidimensional arrays on arbitrary substrates from the microscale to the macroscale) including nanocarbons (fullerene, CNT, graphene, GDY), polymers (PANI, PPy, PI, PDA, g-C_3N_4, PA, etc.), COFs, MOFs, templated carbons and derived carbon-based hybrids are an aesthetically appealing and practically powerful family of materials for application in electrochemical energy devices, including batteries (LIB, LMB, SIB, KIB, ZIB, ZMB, etc.), supercapacitors (EDLCs, pseudocapacitors and hybrid capacitors), fuel cells, metal-air batteries and electrolyzers as well as in associated catalytic reactions (ORR, OER, HER, NRR, etc.). Because of this, many strategies have been developed for the synthesis of optimized 3D HCMNs, such as template-assisted synthesis, CVD, solvothermal treatment, physical treatment (laser, arc discharge, microwave radiation), electrochemical deposition and condensation- and coordination-induced self-assembly. In addition, primary units, hierarchical pores, heteroatom dopants and guest components in 3D HCMNs can be finely controlled and manipulated by varying synthetic conditions and post-treatment processes to provide a platform for the optimization of materials performance in corresponding energy devices.

Despite the rapid progress of 3D HCMNs, challenges remain with respect to better structural control, deeper formation mechanism understanding, optimized device performance as well as increased application exploration. The first challenge is the controllable synthesis of freestanding superstructures with uniform size distributions and broader size ranges from the nanoscale to the macroscale as well as the facile large-area and high-density growth of nanoarrays on both microscopic and macroscopic substrates, particularly the scalable growth of wide-range, dense and long VACNT arrays with controlled CNT diameter, chirality and purity onto substrates. The second challenge involves the more in-depth understanding of 3D HCMN formation mechanisms in which one possible solution is the use of advanced characterization tools such as in situ electron microscopy to provide live observations of morphological evolution. As for the understanding of the impacts of molecular building blocks on hierarchical structure, computational simulations and modeling need to be further developed in which in an ideal situation, the simple input of information such as building blocks and synthetic conditions into a simulation model can allow for the actual prediction of final morphology that match with experimental results. The third challenge is to achieve high performance for practical application in energy devices. Unlike porous carbon materials such as graphene aerogels with numerous large-sized macropores and low volumetric energy densities, 3D HCMNs possess much smaller pore sizes that can enable dense packing and higher volumetric energy density in energy storage devices. However, the overall volumetric energy density of 3D HCMNs remains low and requires optimization through suitable structure design. In addition, current 3D HCMNs have mainly been tested in laboratory settings, which are different from industrial settings where electrode material loadings need to be increased for energy storage devices and corresponding catalysts need to be evaluated based on longer stability timeframes, meaning the

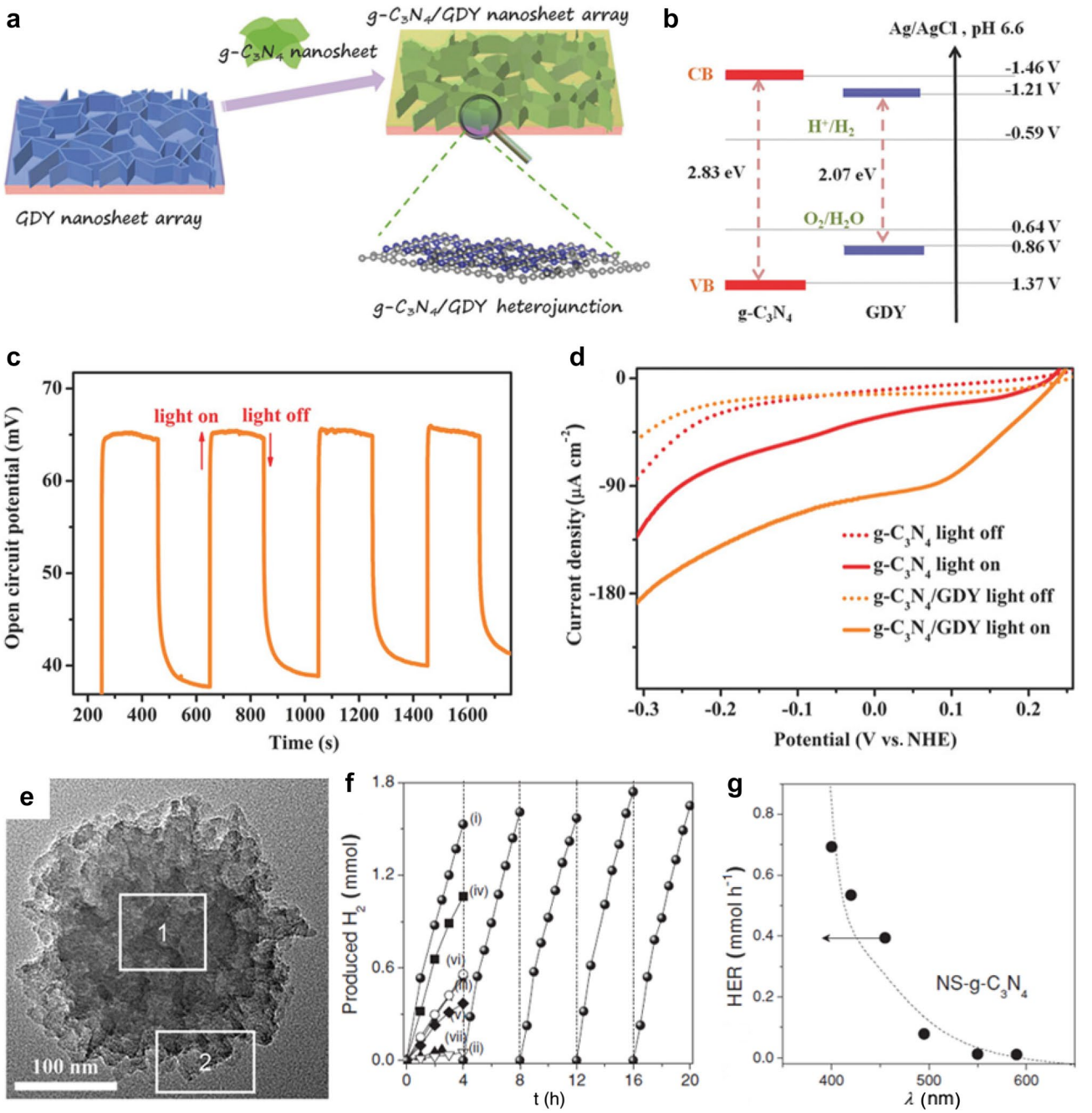

Fig. 20 3D HCMNs for photo(electro)catalysis. Cu-supported vertical grown metal-free 2D/2D g-C_3N_4/GDY heterojunctions for photoelectrochemical water splitting. **a** Schematic illustration for the construction of 3D g-C_3N_4/GDY. **b** Band structures of g-C_3N_4 and GDY. **c** Open circuit potential curve of the g-C_3N_4/GDY photocathode in response to light. **d** Polarization curves for g-C_3N_4/GDY and g-C_3N_4 photocathodes with or without light. Reprinted with permission from Ref. [379]. Copyright © 2018, John Wiley and Sons. Nanospherical g-C_3N_4 flower (NS-g-C_3N_4) for photocatalytic hydrogen production. **e** TEM image of flower-like g-C_3N_4. **f** Durability measurements of photocatalysts under visible light irradiation ($\lambda > 420$ nm): (1) 3 wt% Pt/NS-g-C_3N_4, (2) 3 wt% Pt/bulk-g-C_3N_4, (3) 3 wt% Pt/mpg-C_3N_4, (4) 3 wt% Pt/HCNS, (5) 3 wt% Pt/g-C_3N_4 nanosheets, (6) 3 wt% NS-g-C_3N_4 deformed by vigorous stirring in NH_4HF_2 and (vii) 3 wt% NS-g-C_3N_4 deformed by grinding. **g** Wavelength-dependent photocatalytic H_2 evolution rates of NS-g-C_3N_4. Reprinted with permission from Ref. [139]. Copyright © 2014, John Wiley and Sons

optimization of structures and properties needs to be based on hasher industrial conditions. Overall, increasing amounts of 3D HCMNs are expected to be designed and prepared in the future, especially condensation and coordination systems such as COFs and MOFs based on designable organic species, different metal types and various combinations to

achieve novel properties and applications in electronic, environmental, photonic, thermal, biological and medical fields.

Acknowledgements This work was financially supported by the Natural Sciences and Engineering Research Council of Canada (NSERC) through the Discovery Grant Program (RGPIN-2018-06725) and the Discovery Accelerator Supplement Grant Program (RGPAS-2018-522651) as well as the New Frontiers in Research Fund-Exploration Program (NFRFE-2019-00488). Prof. Xiaolei Wang also acknowledges the support from the University of Alberta and Future Energy Systems (FES).

References

1. Chu, S., Cui, Y., Liu, N.: The path towards sustainable energy. Nat. Mater. **16**, 16–22 (2016). https://doi.org/10.1038/nmat4834
2. Pomerantseva, E., Bonaccorso, F., Feng, X., et al.: Energy storage: the future enabled by nanomaterials. Science. (2019). https://doi.org/10.1126/science.aan8285
3. Yun, Q.B., Lu, Q.P., Zhang, X., et al.: Three-dimensional architectures constructed from transition-metal dichalcogenide nanomaterials for electrochemical energy storage and conversion. Angew. Chem. Int. Ed. **57**, 626–646 (2018). https://doi.org/10.1002/anie.201706426
4. Li, Z., Liu, Z., Sun, H.Y., et al.: Superstructured assembly of nanocarbons: fullerenes, nanotubes, and graphene. Chem. Rev. **115**, 7046–7117 (2015). https://doi.org/10.1021/acs.chemrev.5b00102
5. Tang, C., Wang, H.F., Huang, J.Q., et al.: 3D hierarchical porous graphene-based energy materials: synthesis, functionalization, and application in energy storage and conversion. Electrochem. Energy Rev. **2**, 332–371 (2019). https://doi.org/10.1007/s41918-019-00033-7
6. Li, K., Liang, M.Y., Wang, H., et al.: 3D MXene architectures for efficient energy storage and conversion. Adv. Funct. Mater. **30**, 2000842 (2020). https://doi.org/10.1002/adfm.202000842
7. Nardecchia, S., Carriazo, D., Ferrer, M.L., et al.: Three dimensional macroporous architectures and aerogels built of carbon nanotubes and/or graphene: synthesis and applications. Chem. Soc. Rev. **42**, 794–830 (2013). https://doi.org/10.1039/c2cs35353a
8. Xu, Y., Zhou, M., Lei, Y.: Nanoarchitectured array electrodes for rechargeable lithium- and sodium-ion batteries. Adv. Energy Mater. **6**, 1502514 (2016). https://doi.org/10.1002/aenm.201502514
9. Sun, H.T., Zhu, J., Baumann, D., et al.: Hierarchical 3D electrodes for electrochemical energy storage. Nat. Rev. Mater. **4**, 45–60 (2019). https://doi.org/10.1038/s41578-018-0069-9
10. Cong, L.N., Xie, H.M., Li, J.H.: Hierarchical structures based on two-dimensional nanomaterials for rechargeable lithium batteries. Adv. Energy Mater. **7**, 1601906 (2017). https://doi.org/10.1002/aenm.201601906
11. Jorge, A.B., Jervis, R., Periasamy, A.P., et al.: 3D carbon materials for efficient oxygen and hydrogen electrocatalysis. Adv. Energy Mater. **10**, 1902494 (2020). https://doi.org/10.1002/aenm.201902494
12. Hou, J.G., Wu, Y.Z., Zhang, B., et al.: Rational design of nanoarray architectures for electrocatalytic water splitting. Adv. Funct. Mater. **29**, 1808367 (2019). https://doi.org/10.1002/adfm.201808367
13. Li, X., Yu, J.G., Jaroniec, M.: Hierarchical photocatalysts. Chem. Soc. Rev. **45**, 2603–2636 (2016). https://doi.org/10.1039/c5cs00838g
14. Tang, S.T., Qiu, W.T., Xiao, S., et al.: Harnessing hierarchical architectures to trap light for efficient photoelectrochemical cells. Energy Environ. Sci. **13**, 660–684 (2020). https://doi.org/10.1039/C9EE02986A
15. Hao, Q., Jia, G.H., Wei, W., et al.: Graphitic carbon nitride with different dimensionalities for energy and environmental applications. Nano Res. **13**, 18–37 (2020). https://doi.org/10.1007/s12274-019-2589-z
16. Lu, F.N., Neal, E.A., Nakanishi, T.: Self-assembled and non-assembled alkylated-fullerene materials. Acc. Chem. Res. **52**, 1834–1843 (2019). https://doi.org/10.1021/acs.accounts.9b00217
17. Das, S., Presselt, M.: Progress and development in structural and optoelectronic tunability of supramolecular nonbonded fullerene assemblies. J. Mater. Chem. C **7**, 6194–6216 (2019). https://doi.org/10.1039/c9tc00889f
18. Babu, S.S., Möhwald, H., Nakanishi, T.: Recent progress in morphology control of supramolecular fullerene assemblies and its applications. Chem. Soc. Rev. **39**, 4021–4035 (2010). https://doi.org/10.1039/c000680g
19. Nakanishi, T., Ariga, K., Michinobu, T., et al.: Flower-shaped supramolecular assemblies: hierarchical organization of a fullerene bearing long aliphatic chains. Small **3**, 2019–2023 (2007). https://doi.org/10.1002/smll.200700647
20. Nakanishi, T., Michinobu, T., Yoshida, K., et al.: Nanocarbon superhydrophobic surfaces created from fullerene-based hierarchical supramolecular assemblies. Adv. Mater. **20**, 443–446 (2008). https://doi.org/10.1002/adma.200701537
21. Wang, J.B., Shen, Y.F., Kessel, S., et al.: Self-assembly made durable: water-repellent materials formed by cross-linking fullerene derivatives. Angew. Chem. Int. Ed. **48**, 2166–2170 (2009). https://doi.org/10.1002/anie.200900106
22. Zhang, X., Li, X.D., Ma, L.X., et al.: Electronic and electrochemical properties as well as flowerlike supramolecular assemblies of fulleropyrrolidines bearing ester substituents with different alkyl chain lengths. RSC Adv. **4**, 60342–60348 (2014). https://doi.org/10.1039/C4RA10654G
23. Zhang, X., Nakanishi, T., Ogawa, T., et al.: Flowerlike supramolecular architectures assembled from C60 equipped with a pyridine substituent. Chem. Commun. (Camb.) **46**, 8752–8754 (2010). https://doi.org/10.1039/c0cc03331f
24. Cha, S.I., Miyazawa, K., Kim, J.D.: Vertically well-aligned C60 microtube crystal array prepared using a solution-based, one-step process. Chem. Mater. **20**, 1667–1669 (2008). https://doi.org/10.1021/cm702986f
25. Iijima, S.: Helical microtubules of graphitic carbon. Nature **354**, 56–58 (1991). https://doi.org/10.1038/354056a0
26. Zhang, S.C., Qian, L., Zhao, Q.C., et al.: Carbon nanotube: controlled synthesis determines its future. Sci. China Mater. **63**, 16–34 (2020). https://doi.org/10.1007/s40843-019-9581-4
27. Rao, R., Pint, C.L., Islam, A.E., et al.: Carbon nanotubes and related nanomaterials: critical advances and challenges for synthesis toward mainstream commercial applications. ACS Nano **12**, 11756–11784 (2018). https://doi.org/10.1021/acsnano.8b06511
28. Shah, K.A., Tali, B.A.: Synthesis of carbon nanotubes by catalytic chemical vapour deposition: a review on carbon sources, catalysts and substrates. Mater. Sci. Semicond. Process. **41**, 67–82 (2016). https://doi.org/10.1016/j.mssp.2015.08.013
29. Hata, K., Futaba, D.N., Mizuno, K., et al.: Water-assisted highly efficient synthesis of impurity-free single-walled carbon nanotubes. Science **306**, 1362–1364 (2004). https://doi.org/10.1126/science.1104962
30. Cho, W., Schulz, M., Shanov, V.: Growth and characterization of vertically aligned centimeter long CNT arrays. Carbon **72**, 264–273 (2014). https://doi.org/10.1016/j.carbon.2014.01.074

31. Gong, K.P., Du, F., Xia, Z.H., et al.: Nitrogen-doped carbon nanotube arrays with high electrocatalytic activity for oxygen reduction. Science **323**, 760–764 (2009). https://doi.org/10.1126/science.1168049
32. Wang, H.Y., Moore, J.J.: Low temperature growth mechanisms of vertically aligned carbon nanofibers and nanotubes by radio frequency-plasma enhanced chemical vapor deposition. Carbon **50**, 1235–1242 (2012). https://doi.org/10.1016/j.carbon.2011.10.041
33. Sharma, P., Pavelyev, V., Kumar, S., et al.: Analysis on the synthesis of vertically aligned carbon nanotubes: growth mechanism and techniques. J. Mater. Sci.: Mater. Electron. **31**, 4399–4443 (2020). https://doi.org/10.1007/s10854-020-03021-6
34. Arora, N., Sharma, N.N.: Arc discharge synthesis of carbon nanotubes: comprehensive review. Diam. Relat. Mater. **50**, 135–150 (2014). https://doi.org/10.1016/j.diamond.2014.10.001
35. Cai, X.K., Cong, H.T., Liu, C.: Synthesis of vertically-aligned carbon nanotubes without a catalyst by hydrogen arc discharge. Carbon **50**, 2726–2730 (2012). https://doi.org/10.1016/j.carbon.2012.02.031
36. Hou, H., Reneker, D.: Carbon nanotubes on carbon nanofibers: a novel structure based on electrospun polymer nanofibers. Adv. Mater. **16**, 69–73 (2004). https://doi.org/10.1002/adma.200306205
37. Zeng, Y.X., Zhang, X.Y., Qin, R.F., et al.: Dendrite-free zinc deposition induced by multifunctional CNT frameworks for stable flexible Zn-ion batteries. Adv. Mater. **31**, 1903675 (2019). https://doi.org/10.1002/adma.201903675
38. Xia, B.Y., Yan, Y., Li, N., et al.: A metal–organic framework-derived bifunctional oxygen electrocatalyst. Nat. Energy **1**, 15006 (2016). https://doi.org/10.1038/nenergy.2015.6
39. Meng, J.S., Niu, C.J., Xu, L.H., et al.: General oriented formation of carbon nanotubes from metal-organic frameworks. J. Am. Chem. Soc. **139**, 8212–8221 (2017). https://doi.org/10.1021/jacs.7b01942
40. Chen, Z.L., Wu, R.B., Liu, Y., et al.: Ultrafine Co nanoparticles encapsulated in carbon-nanotubes-grafted graphene sheets as advanced electrocatalysts for the hydrogen evolution reaction. Adv. Mater. **30**, 1802011 (2018). https://doi.org/10.1002/adma.201802011
41. Lee, S.H., Sridhar, V., Jung, J.H., et al.: Graphene–nanotube–iron hierarchical nanostructure as lithium ion battery anode. ACS Nano **7**, 4242–4251 (2013). https://doi.org/10.1021/nn4007253
42. Adeniran, B., Mokaya, R.: Low temperature synthesized carbon nanotube superstructures with superior $CO_2$and hydrogen storage capacity. J. Mater. Chem. A **3**, 5148–5161 (2015). https://doi.org/10.1039/c4ta06539e
43. Chen, L.F., Feng, Y., Liang, H.W., et al.: Macroscopic-scale three-dimensional carbon nanofiber architectures for electrochemical energy storage devices. Adv. Energy Mater. **7**, 1700826 (2017). https://doi.org/10.1002/aenm.201700826
44. Jin, S.L., Deng, H.G., Long, D.H., et al.: Facile synthesis of hierarchically structured Fe_3O_4/carbon micro-flowers and their application to lithium-ion battery anodes. J. Power Sources **196**, 3887–3893 (2011). https://doi.org/10.1016/j.jpowsour.2010.12.078
45. Shi, W.B., Zhou, X.C., Li, J.Y., et al.: High-performance capacitive deionization via manganese oxide-coated, vertically aligned carbon nanotubes. Environ. Sci. Technol. Lett. **5**, 692–700 (2018). https://doi.org/10.1021/acs.estlett.8b00397
46. Luo, J.Y., Jang, H.D., Sun, T., et al.: Compression and aggregation-resistant particles of crumpled soft sheets. ACS Nano **5**, 8943–8949 (2011). https://doi.org/10.1021/nn203115u
47. Luo, J.Y., Zhao, X., Wu, J.S., et al.: Crumpled graphene-encapsulated Si nanoparticles for lithium ion battery anodes. J. Phys. Chem. Lett. **3**, 1824–1829 (2012). https://doi.org/10.1021/jz3006892
48. Chen, C., Xu, Z., Han, Y., et al.: Redissolution of flower-shaped graphene oxide powder with high density. ACS Appl. Mater. Interfaces. **8**, 8000–8007 (2016). https://doi.org/10.1021/acsami.6b00126
49. Park, S.H., Kim, H.K., Yoon, S.B., et al.: Spray-assisted deep-frying process for the in situ spherical assembly of graphene for energy-storage devices. Chem. Mater. **27**, 457–465 (2015). https://doi.org/10.1021/cm5034244
50. Lee, J.Y., Lee, K.H., Kim, Y.J., et al.: Sea-urchin-inspired 3D crumpled graphene balls using simultaneous etching and reduction process for high-density capacitive energy storage. Adv. Funct. Mater. **25**, 3606–3614 (2015). https://doi.org/10.1002/adfm.201404507
51. Jin, H.L., Bu, Y.F., Li, J., et al.: Strong graphene 3D assemblies with high elastic recovery and hardness. Adv. Mater. **30**, 1707424 (2018). https://doi.org/10.1002/adma.201707424
52. Chen, J., Bo, Z., Lu, G.: Vertically-Oriented Graphene. Springer, Cham (2015). https://doi.org/10.1007/978-3-319-15302-5
53. Bo, Z., Mao, S., Han, Z.J., et al.: Emerging energy and environmental applications of vertically-oriented graphenes. Chem. Soc. Rev. **44**, 2108–2121 (2015). https://doi.org/10.1039/c4cs00352g
54. Wang, S.G., Wang, J.J., Miraldo, P., et al.: High field emission reproducibility and stability of carbon nanosheets and nanosheet-based backgated triode emission devices. Appl. Phys. Lett. **89**, 183103 (2006). https://doi.org/10.1063/1.2372708
55. Ren, G.F., Pan, X., Bayne, S., et al.: Kilohertz ultrafast electrochemical supercapacitors based on perpendicularly-oriented graphene grown inside of nickel foam. Carbon **71**, 94–101 (2014). https://doi.org/10.1016/j.carbon.2014.01.017
56. Bo, Z., Yu, K.H., Lu, G.H., et al.: Vertically oriented graphene sheets grown on metallic wires for greener corona discharges: lower power consumption and minimized ozone emission. Energy Environ. Sci. **4**, 2525–2528 (2011). https://doi.org/10.1039/C1EE01140E
57. Chang, H.C., Chang, H.Y., Su, W.J., et al.: Preparation and electrochemical characterization of NiO nanostructure-carbon nanowall composites grown on carbon cloth. Appl. Surf. Sci. **258**, 8599–8602 (2012). https://doi.org/10.1016/j.apsusc.2012.05.057
58. Yu, K.H., Lu, G.H., Bo, Z., et al.: Carbon nanotube with chemically bonded graphene leaves for electronic and optoelectronic applications. J. Phys. Chem. Lett. **2**, 1556–1562 (2011). https://doi.org/10.1021/jz200641c
59. Zhu, M.Y., Wang, J.J., Holloway, B.C., et al.: A mechanism for carbon nanosheet formation. Carbon **45**, 2229–2234 (2007). https://doi.org/10.1016/j.carbon.2007.06.017
60. Zhao, J., Shaygan, M., Eckert, J., et al.: A growth mechanism for free-standing vertical graphene. Nano Lett. **14**, 3064–3071 (2014). https://doi.org/10.1021/nl501039c
61. Fan, Z.J., Yan, J., Zhi, L.J., et al.: A three-dimensional carbon nanotube/graphene sandwich and its application as electrode in supercapacitors. Adv. Mater. **22**, 3723–3728 (2010). https://doi.org/10.1002/adma.201001029
62. Du, F., Yu, D.S., Dai, L.M., et al.: Preparation of tunable 3D pillared carbon nanotube-graphene networks for high-performance capacitance. Chem. Mater. **23**, 4810–4816 (2011). https://doi.org/10.1021/cm2021214
63. Mao, B.S., Wen, Z.H., Bo, Z., et al.: Hierarchical nanohybrids with porous CNT-networks decorated crumpled graphene balls for supercapacitors. ACS Appl. Mater. Interfaces. **6**, 9881–9889 (2014). https://doi.org/10.1021/am502604u
64. Zhu, Y., Li, L., Zhang, C.G., et al.: A seamless three-dimensional carbon nanotube graphene hybrid material. Nat. Commun. **3**, 1225 (2012). https://doi.org/10.1038/ncomms2234

65. Lee, D.H., Kim, J.E., Han, T.H., et al.: Versatile carbon hybrid films composed of vertical carbon nanotubes grown on mechanically compliant graphene films. Adv. Mater. **22**, 1247–1252 (2010). https://doi.org/10.1002/adma.200903063
66. Xue, Y., Ding, Y., Niu, J., et al.: Rationally designed graphene-nanotube 3D architectures with a seamless nodal junction for efficient energy conversion and storage. Sci Adv **1**, 1400198 (2015). https://doi.org/10.1126/sciadv.1400198
67. Xue, Y.R., Li, Y.L., Zhang, J., et al.: 2D graphdiyne materials: challenges and opportunities in energy field. Sci. China Chem. **61**, 765–786 (2018). https://doi.org/10.1007/s11426-018-9270-y
68. Li, G.X., Li, Y.L., Qian, X.M., et al.: Construction of tubular molecule aggregations of graphdiyne for highly efficient field emission. J. Phys. Chem. C **115**, 2611–2615 (2011). https://doi.org/10.1021/jp107996f
69. Qian, X., Ning, Z., Li, Y., et al.: Construction of graphdiyne nanowires with high-conductivity and mobility. Dalton Trans. **41**, 730–733 (2012). https://doi.org/10.1039/c1dt11641j
70. Gao, X., Zhu, Y., Yi, D., et al.: Ultrathin graphdiyne film on graphene through solution-phase van der Waals epitaxy. Sci Adv **4**, eaat6378 (2018). https://doi.org/10.1126/sciadv.aat6378
71. Xue, Y.R., Guo, Y., Yi, Y.P., et al.: Self-catalyzed growth of Cu@graphdiyne core-shell nanowires array for high efficient hydrogen evolution cathode. Nano Energy **30**, 858–866 (2016). https://doi.org/10.1016/j.nanoen.2016.09.005
72. Wang, S.S., Liu, H.B., Kan, X.N., et al.: Superlyophilicity-facilitated synthesis reaction at the microscale: ordered graphdiyne stripe arrays. Small **13**, 1602265 (2017). https://doi.org/10.1002/smll.201602265
73. Zhou, J.Y., Gao, X., Liu, R., et al.: Synthesis of graphdiyne nanowalls using acetylenic coupling reaction. J. Am. Chem. Soc. **137**, 7596–7599 (2015). https://doi.org/10.1021/jacs.5b04057
74. Gao, X., Ren, H.Y., Zhou, J.Y., et al.: Synthesis of hierarchical graphdiyne-based architecture for efficient solar steam generation. Chem. Mater. **29**, 5777–5781 (2017). https://doi.org/10.1021/acs.chemmater.7b01838
75. Gao, X., Li, J., Du, R., et al.: Direct synthesis of graphdiyne nanowalls on arbitrary substrates and its application for photoelectrochemical water splitting cell. Adv. Mater. **29**, 1605308 (2017). https://doi.org/10.1002/adma.201605308
76. Li, J.Q., Xu, J., Xie, Z.Q., et al.: Diatomite-templated synthesis of freestanding 3D graphdiyne for energy storage and catalysis application. Adv. Mater. **30**, 1800548 (2018). https://doi.org/10.1002/adma.201800548
77. Li, J., Gao, X., Liu, B., et al.: Graphdiyne: a metal-free material as hole transfer layer to fabricate quantum dot-sensitized photocathodes for hydrogen production. J. Am. Chem. Soc. **138**, 3954–3957 (2016). https://doi.org/10.1021/jacs.5b12758
78. Li, J., Gao, X., Jiang, X., et al.: Graphdiyne: a promising catalyst-support to stabilize cobalt nanoparticles for oxygen evolution. ACS Catal. **7**, 5209–5213 (2017). https://doi.org/10.1021/acscatal.7b01781
79. Si, H.Y., Deng, Q.X., Chen, L.C., et al.: Hierarchical Graphdiyne@NiFe layered double hydroxide heterostructures as a bifunctional electrocatalyst for overall water splitting. J. Alloy. Compd. **794**, 261–267 (2019). https://doi.org/10.1016/j.jallcom.2019.04.150
80. Berry, G.C., Bockstaller, M.R., Matyjaszewski, K.: Celebrating 100 years of polymer science. Prog. Polym. Sci. **100**, 101193 (2020). https://doi.org/10.1016/j.progpolymsci.2019.101193
81. Su, Z.B., Zhang, R.M., Yan, X.Y., et al.: The role of architectural engineering in macromolecular self-assemblies via non-covalent interactions: a molecular LEGO approach. Prog. Polym. Sci. **103**, 101230 (2020). https://doi.org/10.1016/j.progpolymsci.2020.101230
82. Wang, K., Wu, H.P., Meng, Y.N., et al.: Conducting polymer nanowire arrays for high performance supercapacitors. Small **10**, 14–31 (2014). https://doi.org/10.1002/smll.201301991
83. Martin, C.R., Parthasarathy, R., Menon, V.: Template synthesis of electronically conductive polymers: preparation of thin films. Electrochim. Acta **39**, 1309–1313 (1994). https://doi.org/10.1016/0013-4686(94)E0052-2
84. Cao, Y.Y., Mallouk, T.E.: Morphology of template-grown polyaniline nanowires and its effect on the electrochemical capacitance of nanowire arrays. Chem. Mater. **20**, 5260–5265 (2008). https://doi.org/10.1021/cm801028a
85. Wei, Y., Hu, Q., Cao, Y.H., et al.: Polypyrrole nanotube arrays on carbonized cotton textile for aqueous sodium battery. Org. Electron. **46**, 211–217 (2017). https://doi.org/10.1016/j.orgel.2017.04.008
86. Pan, L. ., Pu, L., Shi, Y., et al.: Synthesis of polyaniline nanotubes with a reactive template of manganese oxide. Adv. Mater. **19**, 461–464 (2007). https://doi.org/10.1002/adma.200602073
87. Liang, L., Liu, J., Windisch Jr., C.F., et al.: Direct assembly of large arrays of oriented conducting polymer nanowires. Angew. Chem. Int. Ed. **41**, 3665–3668 (2002). https://doi.org/10.1002/1521-3773(20021004)41:193665:aid-anie3665%3e3.0.co;2-b
88. Wang, K., Huang, J.Y., Wei, Z.X.: Conducting polyaniline nanowire arrays for high performance supercapacitors. J. Phys. Chem. C **114**, 8062–8067 (2010). https://doi.org/10.1021/jp9113255
89. Li, M., Wei, Z.X., Jiang, L.: Polypyrrole nanofiber arrays synthesized by a biphasic electrochemical strategy. J. Mater. Chem. **18**, 2276–2280 (2008). https://doi.org/10.1039/b800289d
90. Huang, J.Y., Wang, K., Wei, Z.X.: Conducting polymernanowire arrays with enhanced electrochemical performance. J. Mater. Chem. **20**, 1117–1121 (2010). https://doi.org/10.1039/b919928d
91. Wang, Z.J., Jiao, L.S., You, T.Y., et al.: Electrochemical preparation of self-doped poly(o-aminobenzenesulfonic acid-co-aniline) microflowers. Electrochem. Commun. **7**, 875–878 (2005). https://doi.org/10.1016/j.elecom.2005.06.004
92. Chiou, N.R., Lu, C., Guan, J., et al.: Growth and alignment of polyaniline nanofibres with superhydrophobic, superhydrophilic and other properties. Nat. Nanotechnol. **2**, 354–357 (2007). https://doi.org/10.1038/nnano.2007.147
93. Wang, Y.G., Li, H.Q., Xia, Y.Y.: Ordered whiskerlike polyaniline grown on the surface of mesoporous carbon and its electrochemical capacitance performance. Adv. Mater. **18**, 2619–2623 (2006). https://doi.org/10.1002/adma.200600445
94. Xu, J.J., Wang, K., Zu, S.Z., et al.: Hierarchical nanocomposites of polyaniline nanowire arrays on graphene oxide sheets with synergistic effect for energy storage. ACS Nano **4**, 5019–5026 (2010). https://doi.org/10.1021/nn1006539
95. Wang, K., Zhao, P., Zhou, X.M., et al.: Flexible supercapacitors based on cloth-supported electrodes of conducting polymer nanowire array/SWCNT composites. J. Mater. Chem. **21**, 16373–16378 (2011). https://doi.org/10.1039/c1jm13722k
96. Wang, K., Zou, W.J., Quan, B.G., et al.: An all-solid-state flexible micro-supercapacitor on a chip. Adv. Energy Mater. **1**, 1068–1072 (2011). https://doi.org/10.1002/aenm.201100488
97. Zou, W.J., Quan, B.G., Wang, K., et al.: Patterned growth of polyaniline nanowire arrays on a flexible substrate for high-performance gas sensing. Small **7**, 3287–3291 (2011). https://doi.org/10.1002/smll.201100889
98. Wang, K., Wu, H.P., Meng, Y.N., et al.: Integrated energy storage and electrochromic function in one flexible device: an energy storage smart window. Energy Environ. Sci. **5**, 8384–8389 (2012). https://doi.org/10.1039/c2ee21643d
99. Meng, Y.N., Wang, K., Zhang, Y.J., et al.: Hierarchical porous graphene/polyaniline composite film with superior rate

performance for flexible supercapacitors. Adv. Mater. **25**, 6985–6990 (2013). https://doi.org/10.1002/adma.201303529
100. Wang, K., Meng, Q., Zhang, Y., et al.: High-performance two-ply yarn supercapacitors based on carbon nanotubes and polyaniline nanowire arrays. Adv. Mater. **25**, 1494–1498 (2013). https://doi.org/10.1002/adma.201204598
101. Zhou, C.Q., Han, J., Guo, R.: Controllable synthesis of polyaniline multidimensional architectures: from plate-like structures to flower-like superstructures. Macromolecules **41**, 6473–6479 (2008). https://doi.org/10.1021/ma800500u
102. Yang, X.W., Lin, Z.X., Zheng, J.X., et al.: Facile template-free synthesis of vertically aligned polypyrrole nanosheets on nickel foams for flexible all-solid-state asymmetric supercapacitors. Nanoscale **8**, 8650–8657 (2016). https://doi.org/10.1039/c6nr00468g
103. Liaw, D.J., Wang, K.L., Huang, Y.C., et al.: Advanced polyimide materials: syntheses, physical properties and applications. Prog. Polym. Sci. **37**, 907–974 (2012). https://doi.org/10.1016/j.progpolymsci.2012.02.005
104. Ding, Y.C., Hou, H.Q., Zhao, Y., et al.: Electrospun polyimide nanofibers and their applications. Prog. Polym. Sci. **61**, 67–103 (2016). https://doi.org/10.1016/j.progpolymsci.2016.06.006
105. Inagaki, M., Ohta, N., Hishiyama, Y.: Aromatic polyimides as carbon precursors. Carbon **61**, 1–21 (2013). https://doi.org/10.1016/j.carbon.2013.05.035
106. Lin, J., Peng, Z., Liu, Y., et al.: Laser-induced porous graphene films from commercial polymers. Nat. Commun. **5**, 5714 (2014). https://doi.org/10.1038/ncomms6714
107. Xu, Z.X., Zhuang, X.D., Yang, C.Q., et al.: Nitrogen-doped porous carbon superstructures derived from hierarchical assembly of polyimide nanosheets. Adv. Mater. **28**, 1981–1987 (2016). https://doi.org/10.1002/adma.201505131
108. Gu, J.N., Du, Z.G., Zhang, C., et al.: Pyridinic nitrogen-enriched carbon nanogears with thin teeth for superior lithium storage. Adv. Energy Mater. **6**, 1600917 (2016). https://doi.org/10.1002/aenm.201600917
109. Wu, Q., Liu, J.Q., Yuan, C.P., et al.: Nitrogen-doped 3D flower-like carbon materials derived from polyimide as high-performance anode materials for lithium-ion batteries. Appl. Surf. Sci. **425**, 1082–1088 (2017). https://doi.org/10.1016/j.apsusc.2017.07.118
110. Chen, C.W., Huang, H., Yu, Y.K., et al.: Template-free synthesis of hierarchical porous carbon with controlled morphology for CO_2 efficient capture. Chem. Eng. J. **353**, 584–594 (2018). https://doi.org/10.1016/j.cej.2018.07.161
111. Zhu, C.X., Yang, B., Zhang, Y.N., et al.: High-level pyrrolic/pyridinic N-doped carbon nanoflakes from π-fused polyimide for anodic lithium storage. ChemistrySelect **2**, 9007–9013 (2017). https://doi.org/10.1002/slct.201701552
112. Zhao, G.G., Zou, G.Q., Qiu, X.Q., et al.: Rose-like N-doped porous carbon for advanced sodium storage. Electrochim. Acta **240**, 24–30 (2017). https://doi.org/10.1016/j.electacta.2017.04.057
113. Li, J., Luo, M., Ba, Z.H., et al.: Hierarchical multicarbonyl polyimide architectures as promising anode active materials for high-performance lithium/sodium ion batteries. J. Mater. Chem. A **7**, 19112–19119 (2019). https://doi.org/10.1039/C9TA05552E
114. Xu, Z.X., Lu, D., Ma, L., et al.: Hierarchically ordered carbon tube-sheet superstructure via template-directed self-assembly of polyimide. Chem. Eng. J. **364**, 201–207 (2019). https://doi.org/10.1016/j.cej.2019.01.151
115. Li, X.J., Chen, L., Huang, W., et al.: Green synthesis of polyimides and their CNT based nanohybrid shish-kebabs through reaction-induced crystallization of nylon-salt-type monomers in glycerol. Chin. J. Polym. Sci. **32**, 1052–1059 (2014). https://doi.org/10.1007/s10118-014-1480-3
116. Ahmad, A., Wu, H.P., Guo, Y.F., et al.: A graphene supported polyimide nanocomposite as a high performance organic cathode material for lithium ion batteries. RSC Adv. **6**, 33287–33294 (2016). https://doi.org/10.1039/C5RA27471K
117. Wang, Y.H., Cui, X.Q., Zhang, Y.Y., et al.: Achieving high aqueous energy storage via hydrogen-generation passivation. Adv. Mater. **28**, 7626–7632 (2016). https://doi.org/10.1002/adma.201602583
118. Huang, G.X., Zhang, Y., Wang, L., et al.: Fiber-based MnO_2/carbon nanotube/polyimide asymmetric supercapacitor. Carbon **125**, 595–604 (2017). https://doi.org/10.1016/j.carbon.2017.09.103
119. Chen, G.F., Cao, X.R., Wu, S.Q., et al.: Ammonia electrosynthesis with high selectivity under ambient conditions via a Li^+ incorporation strategy. J. Am. Chem. Soc. **139**, 9771–9774 (2017). https://doi.org/10.1021/jacs.7b04393
120. Chen, L., Chen, Z.H., Li, X., et al.: Dynamic imine chemistry assisted reaction induced hetero-epitaxial crystallization: novel approach towards aromatic polymer/CNT nanohybrid shish-kebabs and related hybrid crystalline structures. Polymer **54**, 1739–1745 (2013). https://doi.org/10.1016/j.polymer.2013.01.046
121. Wu, H.P., Shevlin, S.A., Meng, Q.H., et al.: Flexible and binder-free organic cathode for high-performance lithium-ion batteries. Adv. Mater. **26**, 3338–3343 (2014). https://doi.org/10.1002/adma.201305452
122. Wang, Z.P., Ogata, H., Morimoto, S., et al.: Synthesis of carbon nanosheets from Kapton polyimide by microwave plasma treatment. Carbon **72**, 421–424 (2014). https://doi.org/10.1016/j.carbon.2014.02.021
123. Duy, L.X., Peng, Z.W., Li, Y.L., et al.: Laser-induced graphene fibers. Carbon **126**, 472–479 (2018). https://doi.org/10.1016/j.carbon.2017.10.036
124. Lee, H., Dellatore, S.M., Miller, W.M., et al.: Mussel-inspired surface chemistry for multifunctional coatings. Science **318**, 426–430 (2007). https://doi.org/10.1126/science.1147241
125. Qu, K.G., Wang, Y.H., Vasileff, A., et al.: Polydopamine-inspired nanomaterials for energy conversion and storage. J. Mater. Chem. A **6**, 21827–21846 (2018). https://doi.org/10.1039/c8ta05245j
126. Ma, F.X., Wu, H.B., Xia, B.Y., et al.: Hierarchical β-Mo_2 C nanotubes organized by ultrathin nanosheets as a highly efficient electrocatalyst for hydrogen production. Angew. Chem. Int. Ed. Engl. **54**, 15395–15399 (2015). https://doi.org/10.1002/anie.201508715
127. Sun, L., Wang, C., Sun, Q., et al.: Self-assembly of hierarchical Ni-Mo-polydopamine microflowers and their conversion to a Ni-Mo_2C/C composite for water splitting. Chem. - A Eur. J. **23**, 4644–4650 (2017). https://doi.org/10.1002/chem.201605928
128. Huang, Y., Gong, Q.F., Song, X.N., et al.: Mo2C nanoparticles dispersed on hierarchical carbon microflowers for efficient electrocatalytic hydrogen evolution. ACS Nano **10**, 11337–11343 (2016). https://doi.org/10.1021/acsnano.6b06580
129. Chen, L., Jiang, H., Jiang, H.B., et al.: Mo-based ultrasmall nanoparticles on hierarchical carbon nanosheets for superior lithium ion storage and hydrogen generation catalysis. Adv. Energy Mater. **7**, 1602782 (2017). https://doi.org/10.1002/aenm.201602782
130. Wang, C.L., Sun, L.S., Zhang, F.F., et al.: Formation of Mo-polydopamine hollow spheres and their conversions to MoO_2/C and Mo_2C/C for efficient electrochemical energy storage and catalyst. Small **13**, 1701246 (2017). https://doi.org/10.1002/smll.201701246
131. Sun, L.S., Wang, C.L., Wang, X.X., et al.: Morphology evolution and control of Mo-polydopamine coordination complex from 2D single nanopetal to hierarchical microflowers. Small **14**, 1800090 (2018). https://doi.org/10.1002/smll.201800090

132. Zhang, J., Zhou, L., Sun, Q.J., et al.: Metal-organic coordination strategy for obtaining metal-decorated Mo-based complexes: multi-dimensional structural evolution and high-rate lithium-ion battery applications. Chem. - A Eur. J. **25**, 8813–8819 (2019). https://doi.org/10.1002/chem.201900972
133. Jiao, X.J., Liu, X.J., Wang, B.B., et al.: A controllable strategy for the self-assembly of WM nanocrystals/nitrogen-doped porous carbon superstructures (M = O, C, P, S, and Se) for sodium and potassium storage. J. Mater. Chem. A **8**, 2047–2065 (2020). https://doi.org/10.1039/c9ta11312f
134. Wang, X.C., Maeda, K., Thomas, A., et al.: A metal-free polymeric photocatalyst for hydrogen production from water under visible light. Nat. Mater. **8**, 76–80 (2009). https://doi.org/10.1038/nmat2317
135. Niu, W.H., Yang, Y.: Graphitic carbon nitride for electrochemical energy conversion and storage. ACS Energy Lett. **3**, 2796–2815 (2018). https://doi.org/10.1021/acsenergylett.8b01594
136. Jun, Y.S., Lee, E.Z., Wang, X.C., et al.: From melamine-cyanuric acid supramolecular aggregates to carbon nitride hollow spheres. Adv. Funct. Mater. **23**, 3661–3667 (2013). https://doi.org/10.1002/adfm.201203732
137. Jun, Y.S., Park, J., Lee, S.U., et al.: Three-dimensional macroscopic assemblies of low-dimensional carbon nitrides for enhanced hydrogen evolution. Angew. Chem. Int. Ed. **52**, 11083–11087 (2013). https://doi.org/10.1002/anie.201304034
138. Shalom, M., Gimenez, S., Schipper, F., et al.: Controlled carbon nitride growth on surfaces for hydrogen evolution electrodes. Angew. Chem. Int. Ed. **53**, 3654–3658 (2014). https://doi.org/10.1002/anie.201309415
139. Zhang, J.S., Zhang, M.W., Yang, C., et al.: Nanospherical carbon nitride frameworks with sharp edges accelerating charge collection and separation at a soft photocatalytic interface. Adv. Mater. **26**, 4121–4126 (2014). https://doi.org/10.1002/adma.201400573
140. Zhu, Y.P., Ren, T.Z., Yuan, Z.Y.: Mesoporous phosphorus-doped g-C_3N_4 nanostructured flowers with superior photocatalytic hydrogen evolution performance. ACS Appl. Mater. Interfaces. **7**, 16850–16856 (2015). https://doi.org/10.1021/acsami.5b04947
141. Ma, T.Y., Ran, J.R., Dai, S., et al.: Phosphorus-doped graphitic carbon nitrides grown In Situ on carbon-fiber paper: flexible and reversible oxygen electrodes. Angew. Chem. Int. Ed. **54**, 4646–4650 (2015). https://doi.org/10.1002/anie.201411125
142. Bian, S.W., Ma, Z., Song, W.G.: Preparation and characterization of carbon nitride nanotubes and their applications as catalyst supporter. J. Phys. Chem. C **113**, 8668–8672 (2009). https://doi.org/10.1021/jp810630k
143. Yan, Y.Z., Chen, L., Dai, H.J., et al.: Morphosynthesis of nanostructured polyazomethines and carbon through constitutional dynamic chemistry controlled reaction induced crystallization process. Polymer **53**, 1611–1616 (2012). https://doi.org/10.1016/j.polymer.2012.02.025
144. Qiu, L.B., Jiang, Y., Sun, X.M., et al.: Surface-nanostructured cactus-like carbon microspheres for efficient photovoltaic devices. J. Mater. Chem. A **2**, 15132–15138 (2014). https://doi.org/10.1039/c4ta02979h
145. Higuchi, R., Tanoue, R., Sakaguchi, K., et al.: Vertically standing nanowalls of pristine poly(azomethine) on a graphite by chemical liquid deposition. Polymer **54**, 3452–3457 (2013). https://doi.org/10.1016/j.polymer.2013.04.065
146. Chen, S.C., Koshy, D.M., Tsao, Y., et al.: Highly tunable and facile synthesis of uniform carbon flower particles. J. Am. Chem. Soc. **140**, 10297–10304 (2018). https://doi.org/10.1021/jacs.8b05825
147. Liu, Y.J., Liu, N., Yu, L.M., et al.: Design and synthesis of mint leaf-like polyacrylonitrile and carbon nanosheets for flexible all-solid-state asymmetric supercapacitors. Chem. Eng. J. **362**, 600–608 (2019). https://doi.org/10.1016/j.cej.2019.01.058
148. Zhang, K., Geissler, A., Chen, X.L., et al.: Polymeric flower-like microparticles from self-assembled cellulose stearoyl esters. ACS Macro Lett. **4**, 214–219 (2015). https://doi.org/10.1021/mz500788e
149. Wang, Y.G., Tian, J., Deng, X., et al.: Polymeric flaky nanostructures from cellulose stearoyl esters for functional surfaces. Adv. Mater. Interfaces **3**, 1600636 (2016). https://doi.org/10.1002/admi.201600636
150. Diercks, C.S., Yaghi, O.M.: The atom, the molecule, and the covalent organic framework. Science **355**. https://doi.org/10.1126/science.aal1585. (2017). https://doi.org/10.1126/science.aal1585
151. Gao, X., Dong, Y., Li, S.W., et al.: MOFs and COFs for batteries and supercapacitors. Electrochem. Energy Rev. **3**, 81–126 (2020). https://doi.org/10.1007/s41918-019-00055-1
152. Feng, L., Wang, K.Y., Day, G.S., et al.: The chemistry of multi-component and hierarchical framework compounds. Chem. Soc. Rev. **48**, 4823–4853 (2019). https://doi.org/10.1039/c9cs00250b
153. Kim, S., Park, C., Lee, M., et al.: Rapid photochemical synthesis of sea-urchin-shaped hierarchical porous COF-5 and its lithography-free patterned growth. Adv. Funct. Mater. **27**, 1700925 (2017). https://doi.org/10.1002/adfm.201700925
154. Sun, J.H., Klechikov, A., Moise, C., et al.: A molecular pillar approach to grow vertical covalent organic framework nanosheets on graphene: hybrid materials for energy storage. Angew. Chem. Int. Ed. **57**, 1034–1038 (2018). https://doi.org/10.1002/anie.201710502
155. Hu, X.H., Jian, J.H., Fang, Z.S., et al.: Hierarchical assemblies of conjugated ultrathin COF nanosheets for high-sulfur-loading and long-lifespan lithium-sulfur batteries: fully-exposed porphyrin matters. Energy Storage Mater. **22**, 40–47 (2019). https://doi.org/10.1016/j.ensm.2018.12.021
156. Wang, S., Zhang, Z.Y., Zhang, H.M., et al.: Reversible polycondensation-termination growth of covalent-organic-framework spheres, fibers, and films. Matter **1**, 1592–1605 (2019). https://doi.org/10.1016/j.matt.2019.08.019
157. Wang, S., Yang, Y.H., Liu, P.W., et al.: Core-shell and yolk-shell covalent organic framework nanostructures with size-selective permeability. Cell Rep. Phys. Sci. **1**, 100062 (2020). https://doi.org/10.1016/j.xcrp.2020.100062
158. Zhao, R., Liang, Z.B., Zou, R.Q., et al.: Metal-organic frameworks for batteries. Joule **2**, 2235–2259 (2018). https://doi.org/10.1016/j.joule.2018.09.019
159. Liao, P.Q., Shen, J.Q., Zhang, J.P.: Metal-organic frameworks for electrocatalysis. Coord. Chem. Rev. **373**, 22–48 (2018). https://doi.org/10.1016/j.ccr.2017.09.001
160. Feng, L., Wang, K.Y., Powell, J., et al.: Controllable synthesis of metal-organic frameworks and their hierarchical assemblies. Matter **1**, 801–824 (2019). https://doi.org/10.1016/j.matt.2019.08.022
161. Carné-Sánchez, A., Imaz, I., Cano-Sarabia, M., et al.: A spray-drying strategy for synthesis of nanoscale metal–organic frameworks and their assembly into hollow superstructures. Nat. Chem. **5**, 203–211 (2013). https://doi.org/10.1038/nchem.1569
162. Zou, L., Kitta, M., Hong, J., et al.: Fabrication of a spherical superstructure of carbon nanorods. Adv. Mater. **31**, e1900440 (2019). https://doi.org/10.1002/adma.201900440
163. Yang, Y., Mao, K.T., Gao, S.Q., et al.: O-, N-atoms-coordinated Mn cofactors within a graphene framework as bioinspired oxygen reduction reaction electrocatalysts. Adv. Mater. **30**, 1801732 (2018). https://doi.org/10.1002/adma.201801732
164. Guan, B.Y., Yu, L., (David) Lou, X.W.: A dual-metal–organic-framework derived electrocatalyst for oxygen reduction. Energy

Environ. Sci. **9**, 3092–3096 (2016). https://doi.org/10.1039/c6ee02171a
165. Feng, L., Li, J.L., Day, G.S., et al.: Temperature-controlled evolution of nanoporous MOF crystallites into hierarchically porous superstructures. Chem **5**, 1265–1274 (2019). https://doi.org/10.1016/j.chempr.2019.03.003
166. Feng, L., Wang, K.Y., Yan, T.H., et al.: Porous crystalline spherulite superstructures. Chem **6**, 460–471 (2020). https://doi.org/10.1016/j.chempr.2019.12.001
167. Feng, L., Wang, K.Y., Yan, T.H., et al.: Seed-mediated evolution of hierarchical metal-organic framework quaternary superstructures. Chem Sci **11**, 1643–1648 (2020). https://doi.org/10.1039/c9sc06064b
168. Zhang, Z.C., Chen, Y.F., He, S., et al.: Hierarchical Zn/Ni-MOF-2 nanosheet-assembled hollow nanocubes for multicomponent catalytic reactions. Angew. Chem. Int. Ed. **126**, 12725–12729 (2014). https://doi.org/10.1002/ange.201406484
169. Yang, J., Zheng, C., Xiong, P.X., et al.: Zn-doped Ni-MOF material with a high supercapacitive performance. J. Mater. Chem. A **2**, 19005–19010 (2014). https://doi.org/10.1039/c4ta04346d
170. Jiao, Y., Pei, J., Chen, D.H., et al.: Mixed-metallic MOF based electrode materials for high performance hybrid supercapacitors. J. Mater. Chem. A **5**, 1094–1102 (2017). https://doi.org/10.1039/c6ta09805c
171. Xia, H.C., Zhang, J.N., Yang, Z., et al.: 2D MOF nanoflake-assembled spherical microstructures for enhanced supercapacitor and electrocatalysis performances. Nano - Micro Lett. **9**, 43 (2017). https://doi.org/10.1007/s40820-017-0144-6
172. Li, C., Hu, X.S., Lou, X.B., et al.: The organic-moiety-dominated Li + intercalation/deintercalation mechanism of a cobalt-based metal-organic framework. J. Mater. Chem. A **4**, 16245–16251 (2016). https://doi.org/10.1039/C6TA06413B
173. Yan, Y., Gu, P., Zheng, S.S., et al.: Facile synthesis of an accordion-like Ni-MOF superstructure for high-performance flexible supercapacitors. J. Mater. Chem. A **4**, 19078–19085 (2016). https://doi.org/10.1039/c6ta08331e
174. Zhu, Q.L., Xia, W., Akita, T., et al.: Metal-organic framework-derived honeycomb-like open porous nanostructures as precious-metal-free catalysts for highly efficient oxygen electroreduction. Adv. Mater. **28**, 6391–6398 (2016). https://doi.org/10.1002/adma.201600979
175. Zhu, Q.L., Xia, W., Zheng, L.R., et al.: Atomically dispersed Fe/N-doped hierarchical carbon architectures derived from a metal-organic framework composite for extremely efficient electrocatalysis. ACS Energy Lett. **2**, 504–511 (2017). https://doi.org/10.1021/acsenergylett.6b00686
176. Wang, T.S., Kim, H.K., Liu, Y.J., et al.: Bottom-up formation of carbon-based structures with multilevel hierarchy from MOF-guest polyhedra. J. Am. Chem. Soc. **140**, 6130–6136 (2018). https://doi.org/10.1021/jacs.8b02411
177. Ma, T.Y., Dai, S., Jaroniec, M., et al.: Metal–organic framework derived hybrid Co_3O_4-carbon porous nanowire arrays as reversible oxygen evolution electrodes. J. Am. Chem. Soc. **136**, 13925–13931 (2014). https://doi.org/10.1021/ja5082553
178. Zhang, C., Xiao, J., Lv, X., et al.: Hierarchically porous Co_3O_4/C nanowire arrays derived from a metal–organic framework for high performance supercapacitors and the oxygen evolution reaction. J. Mater. Chem. A **4**, 16516–16523 (2016). https://doi.org/10.1039/c6ta06314d
179. Lu, X.F., Gu, L.F., Wang, J.W., et al.: Bimetal-organic framework derived $CoFe_2O_4$/C porous hybrid nanorod arrays as high-performance electrocatalysts for oxygen evolution reaction. Adv. Mater. **29**, 1604437 (2017). https://doi.org/10.1002/adma.201604437
180. Zhou, D., Ni, J.F., Li, L.: Self-supported multicomponent CPO-27 MOF nanoarrays as high-performance anode for lithium storage. Nano Energy **57**, 711–717 (2019). https://doi.org/10.1016/j.nanoen.2019.01.010
181. Zhang, G.H., Hou, S.C., Zhang, H., et al.: High-performance and ultra-stable lithium-ion batteries based on MOF-derived ZnO@ZnO quantum dots/C core-shell nanorod arrays on a carbon cloth anode. Adv. Mater. **27**, 2400–2405 (2015). https://doi.org/10.1002/adma.201405222
182. Zhou, J., Dou, Y.B., Zhou, A., et al.: MOF template-directed fabrication of hierarchically structured electrocatalysts for efficient oxygen evolution reaction. Adv. Energy Mater. **7**, 1602643 (2017). https://doi.org/10.1002/aenm.201602643
183. Fang, G.Z., Zhou, J., Liang, C.W., et al.: MOFs nanosheets derived porous metal oxide-coated three-dimensional substrates for lithium-ion battery applications. Nano Energy **26**, 57–65 (2016). https://doi.org/10.1016/j.nanoen.2016.05.009
184. Duan, J., Chen, S., Zhao, C.: Ultrathin metal-organic framework array for efficient electrocatalytic water splitting. Nat. Commun. **8**, 15341 (2017). https://doi.org/10.1038/ncomms15341
185. Guan, C., Liu, X.M., Ren, W.N., et al.: Rational design of metal-organic framework derived hollow $NiCo_2O_4$ arrays for flexible supercapacitor and electrocatalysis. Adv. Energy Mater. **7**, 1602391 (2017). https://doi.org/10.1002/aenm.201602391
186. Ji, D.X., Fan, L., Li, L.L., et al.: Atomically transition metals on self-supported porous carbon flake arrays as binder-free air cathode for wearable Zinc-air batteries. Adv. Mater. **31**, 1808267 (2019). https://doi.org/10.1002/adma.201808267
187. Ji, D.X., Fan, L., Tao, L., et al.: The kirkendall effect for engineering oxygen vacancy of hollow Co_3O_4 nanoparticles toward high-performance portable zinc-air batteries. Angew. Chem. Int. Ed. **58**, 13840–13844 (2019). https://doi.org/10.1002/anie.201908736
188. Wang, X., Liao, Z.Q., Fu, Y.B., et al.: Confined growth of porous nitrogen-doped cobalt oxide nanoarrays as bifunctional oxygen electrocatalysts for rechargeable zinc-air batteries. Energy Storage Mater. **26**, 157–164 (2020). https://doi.org/10.1016/j.ensm.2019.12.043
189. Zhou, T., Shen, J.D., Wang, Z.S., et al.: Regulating lithium nucleation and deposition via MOF-derived Co@C-modified carbon cloth for stable Li metal anode. Adv. Funct. Mater. **30**, 1909159 (2020). https://doi.org/10.1002/adfm.201909159
190. Falcaro, P., Okada, K., Hara, T., et al.: Centimetre-scale micropore alignment in oriented polycrystalline metal-organic framework films via heteroepitaxial growth. Nat. Mater. **16**, 342–348 (2017). https://doi.org/10.1038/nmat4815
191. Cai, G.R., Zhang, W., Jiao, L., et al.: Template-directed growth of well-aligned MOF arrays and derived self-supporting electrodes for water splitting. Chem **2**, 791–802 (2017). https://doi.org/10.1016/j.chempr.2017.04.016
192. Zhao, Y.B., Kornienko, N., Liu, Z., et al.: Mesoscopic constructs of ordered and oriented metal-organic frameworks on plasmonic silver nanocrystals. J. Am. Chem. Soc. **137**, 2199–2202 (2015). https://doi.org/10.1021/ja512951e
193. Li, Z.H., Shao, M.F., Zhou, L., et al.: Directed growth of metal-organic frameworks and their derived carbon-based network for efficient electrocatalytic oxygen reduction. Adv. Mater. **28**, 2337–2344 (2016). https://doi.org/10.1002/adma.201505086
194. Li, W., Liu, J., Zhao, D.Y.: Mesoporous materials for energy conversion and storage devices. Nat. Rev. Mater. **1**, 16023 (2016). https://doi.org/10.1038/natrevmats.2016.23
195. Wang, Q., Yan, J., Wang, Y.B., et al.: Three-dimensional flower-like and hierarchical porous carbon materials as high-rate performance electrodes for supercapacitors. Carbon **67**, 119–127 (2014). https://doi.org/10.1016/j.carbon.2013.09.070
196. Zhou, L., Huang, T., Yu, A.S.: Three-dimensional flower-shaped activated porous carbon/sulfur composites as cathode materials

for lithium–sulfur batteries. ACS Sustainable Chem. Eng. **2**, 2442–2447 (2014). https://doi.org/10.1021/sc500459c
197. Shao, J.Q., Song, M.Y., Wu, G., et al.: 3D carbon nanocage networks with multiscale pores for high-rate supercapacitors by flower-like template and in situ coating. Energy Storage Mater. **13**, 57–65 (2018). https://doi.org/10.1016/j.ensm.2017.12.023
198. Guo, D.Y., Chen, X.A., Wei, H.F., et al.: Controllable synthesis of highly uniform flower-like hierarchical carbon nanospheres and their application in high performance lithium–sulfur batteries. J. Mater. Chem. A **5**, 6245–6256 (2017). https://doi.org/10.1039/c7ta00335h
199. Ding, F., Yu, Z.S., Chen, X., et al.: High-performance supercapacitors based on reduced graphene oxide -wrapped carbon nanoflower with efficient transport pathway of electrons and electrolyte ions. Electrochim. Acta **306**, 549–557 (2019). https://doi.org/10.1016/j.electacta.2019.03.155
200. Guo, X.F., Liang, J.Y., Chen, S.L., et al.: Expeditious fabrication of flower-like hierarchical mesoporous carbon superstructures as supercapacitor electrode materials. J. Mater. Chem. A **2**, 16884–16891 (2014)
201. Liang, J.Y., Wang, C.C., Lu, S.Y.: Glucose-derived nitrogen-doped hierarchical hollow nest-like carbon nanostructures from a novel template-free method as an outstanding electrode material for supercapacitors. J. Mater. Chem. A **3**, 24453–24462 (2015). https://doi.org/10.1039/c5ta08007j
202. Zheng, Z.M., Zhang, X., Pei, F., et al.: Hierarchical porous carbon microrods composed of vertically aligned graphene-like nanosheets for Li-ion batteries. J. Mater. Chem. A **3**, 19800–19806 (2015). https://doi.org/10.1039/c5ta05183e
203. Zhu, J.X., Sakaushi, K., Clavel, G., et al.: A general salt-templating method to fabricate vertically aligned graphitic carbon nanosheets and their metal carbide hybrids for superior lithium ion batteries and water splitting. J. Am. Chem. Soc. **137**, 5480–5485 (2015). https://doi.org/10.1021/jacs.5b01072
204. Xia, X.H., Zhang, Y.Q., Fan, Z.X., et al.: Novel Metal@Carbon spheres core-shell arrays by controlled self-assembly of carbon nanospheres: a stable and flexible supercapacitor electrode. Adv. Energy Mater. **5**, 1401709 (2015). https://doi.org/10.1002/aenm.201401709
205. Zhang, G.H., Song, Y.A., Zhang, H., et al.: Radially aligned porous carbon nanotube arrays on carbon fibers: a hierarchical 3D carbon nanostructure for high-performance capacitive energy storage. Adv. Funct. Mater. **26**, 3012–3020 (2016). https://doi.org/10.1002/adfm.201505226
206. Liu, H.J., Wang, X.M., Cui, W.J., et al.: Highly ordered mesoporous carbon nanofiber arrays from a crab shell biological template and its application in supercapacitors and fuel cells. J. Mater. Chem. **20**, 4223–4230 (2010). https://doi.org/10.1039/b925776d
207. Li, M., Lu, J., Chen, Z.W., et al.: 30 years of lithium-ion batteries. Adv. Mater. **30**, 1800561 (2018). https://doi.org/10.1002/adma.201800561
208. Issues and challenges facing rechargeable lithium batteries: M Tarascon, J., Armand, M. Nature **414**, 359–367 (2001). https://doi.org/10.1038/35104644
209. Dunn, B., Kamath, H., Tarascon, J.M.: Electrical energy storage for the grid: a battery of choices. Science **334**, 928–935 (2011). https://doi.org/10.1126/science.1212741
210. Goriparti, S., Miele, E., De Angelis, F., et al.: Review on recent progress of nanostructured anode materials for Li-ion batteries. J. Power Sources **257**, 421–443 (2014). https://doi.org/10.1016/j.jpowsour.2013.11.103
211. Dahn, J.R., Zheng, T., Liu, Y., et al.: Mechanisms for lithium insertion in carbonaceous materials. Science **270**, 590–593 (1995). https://doi.org/10.1126/science.270.5236.590
212. Zhao, Y., Wang, L.P., Sougrati, M.T., et al.: A review on design strategies for carbon based metal oxides and sulfides nanocomposites for high performance Li and Na ion battery anodes. Adv. Energy Mater. **7**, 1601424 (2017). https://doi.org/10.1002/aenm.201601424
213. Wang, X.L., Li, G., Seo, M.H., et al.: Carbon-coated silicon nanowires on carbon fabric as self-supported electrodes for flexible lithium-ion batteries. ACS Appl. Mater. Interfaces. **9**, 9551–9558 (2017). https://doi.org/10.1021/acsami.6b12080
214. Luo, D., Deng, Y.P., Wang, X.L., et al.: Tuning shell numbers of transition metal oxide hollow microspheres toward durable and superior lithium storage. ACS Nano **11**, 11521–11530 (2017). https://doi.org/10.1021/acsnano.7b06296
215. Wang, X.L., Li, G., Seo, M.H., et al.: Sulfur atoms bridging few-layered MoS_2 with S-doped graphene enable highly robust anode for lithium-ion batteries. Adv. Energy Mater. **5**, 1501106 (2015). https://doi.org/10.1002/aenm.201501106
216. Wang, X.L., Li, G., Hassan, F.M., et al.: Building sponge-like robust architectures of CNT–graphene–Si composites with enhanced rate and cycling performance for lithium-ion batteries. J. Mater. Chem. A **3**, 3962–3967 (2015). https://doi.org/10.1039/c4ta06249c
217. Feng, K., Ahn, W., Lui, G., et al.: Implementing an in situ carbon network in Si/reduced graphene oxide for high performance lithium-ion battery anodes. Nano Energy **19**, 187–197 (2016). https://doi.org/10.1016/j.nanoen.2015.10.025
218. Lui, G., Li, G., Wang, X.L., et al.: Flexible, three-dimensional ordered macroporous TiO_2 electrode with enhanced electrode-electrolyte interaction in high-power Li-ion batteries. Nano Energy **24**, 72–77 (2016). https://doi.org/10.1016/j.nanoen.2016.03.019
219. Hassan, F.M., Batmaz, R., Li, J., et al.: Evidence of covalent synergy in silicon-sulfur-graphene yielding highly efficient and long-life lithium-ion batteries. Nat. Commun. **6**, 8597 (2015). https://doi.org/10.1038/ncomms9597
220. Tjandra, R., Li, G., Wang, X.L., et al.: Flexible high performance lithium ion battery electrode based on a free-standing TiO_2 nanocrystals/carbon cloth composite. RSC Adv. **6**, 35479–35485 (2016). https://doi.org/10.1039/c6ra03262a
221. Hu, C.G., Lv, L., Xue, J.L., et al.: Branched graphene nanocapsules for anode material of lithium-ion batteries. Chem. Mater. **27**, 5253–5260 (2015). https://doi.org/10.1021/acs.chemmater.5b01398
222. Xiao, X.C., Liu, P., Wang, J.S., et al.: Vertically aligned graphene electrode for lithium ion battery with high rate capability. Electrochem. Commun. **13**, 209–212 (2011). https://doi.org/10.1016/j.elecom.2010.12.016
223. Xu, Z.M., Lv, X., Li, J., et al.: A promising anode material for sodium-ion battery with high capacity and high diffusion ability: graphyne and graphdiyne. RSC Adv. **6**, 25594–25600 (2016). https://doi.org/10.1039/c6ra01870j
224. Wang, K., Wang, N., He, J.J., et al.: Graphdiyne nanowalls as anode for lithium-ion batteries and capacitors exhibit superior cyclic stability. Electrochim. Acta **253**, 506–516 (2017). https://doi.org/10.1016/j.electacta.2017.09.101
225. Yuan, Y., Chen, Z.W., Yu, H.X., et al.: Heteroatom-doped carbon-based materials for lithium and sodium ion batteries. Energy Storage Mater. **32**, 65–90 (2020). https://doi.org/10.1016/j.ensm.2020.07.027
226. Ma, C.C., Shao, X.H., Cao, D.P.: Nitrogen-doped graphene nanosheets as anode materials for lithium ion batteries: a first-principles study. J. Mater. Chem. **22**, 8911–8915 (2012). https://doi.org/10.1039/c2jm00166g
227. Chen, Z., Du, Y., Zhang, Z., et al.: A facile strategy to prepare (N, Ni, P) tri-doped echinus-like porous carbon spheres as advanced

anode for lithium ion batteries. Nanotechnology **30**, 495403 (2019). https://doi.org/10.1088/1361-6528/ab3f07
228. Ashuri, M., He, Q., Shaw, L.L.: Silicon as a potential anode material for Li-ion batteries: where size, geometry and structure matter. Nanoscale **8**, 74–103 (2016). https://doi.org/10.1039/c5nr05116a
229. Magasinski, A., Dixon, P., Hertzberg, B., et al.: Erratum: high-performance lithium-ion anodes using a hierarchical bottom-up approach. Nat. Mater. **9**, 353–358 (2010). https://doi.org/10.1038/nmat2749
230. Jia, H.P., Li, X.L., Song, J.H., et al.: Hierarchical porous silicon structures with extraordinary mechanical strength as high-performance lithium-ion battery anodes. Nat. Commun. **11**, 1474 (2020). https://doi.org/10.1038/s41467-020-15217-9
231. Wang, W., Epur, R., Kumta, P.N.: Vertically aligned silicon/carbon nanotube (VASCNT) arrays: hierarchical anodes for lithium-ion battery. Electrochem. Commun. **13**, 429–432 (2011). https://doi.org/10.1016/j.elecom.2011.02.012
232. Guo, Y.Y., Zeng, X.Q., Zhang, Y., et al.: Sn nanoparticles encapsulated in 3D nanoporous carbon derived from a metal-organic framework for anode material in lithium-ion batteries. ACS Appl. Mater. Interfaces. **9**, 17172–17177 (2017). https://doi.org/10.1021/acsami.7b04561
233. Wang, H., Wu, X., Qi, X.J., et al.: Sb nanoparticles encapsulated in 3D porous carbon as anode material for lithium-ion and potassium-ion batteries. Mater. Res. Bull. **103**, 32–37 (2018). https://doi.org/10.1016/j.materresbull.2018.03.018
234. Yang, C.L., Jiang, Y., Liu, X.W., et al.: Germanium encapsulated in sulfur and nitrogen co-doped 3D porous carbon as an ultra-long-cycle life anode for lithium ion batteries. J. Mater. Chem. A **4**, 18711–18716 (2016). https://doi.org/10.1039/c6ta08681k
235. Cai, H.Y., Han, K., Jiang, H., et al.: Self-standing silicon-carbon nanotube/graphene by a scalable in situ approach from low-cost Al-Si alloy powder for lithium ion batteries. J. Phys. Chem. Solids **109**, 9–17 (2017). https://doi.org/10.1016/j.jpcs.2017.05.009
236. Li, N., Song, H.W., Cui, H., et al.: Sn@graphene grown on vertically aligned graphene for high-capacity, high-rate, and long-life lithium storage. Nano Energy **3**, 102–112 (2014). https://doi.org/10.1016/j.nanoen.2013.10.014
237. Ren, G.F., Hoque, M.N.F., Liu, J.W., et al.: Perpendicular edge oriented graphene foam supporting orthogonal TiO_2(B) nanosheets as freestanding electrode for lithium ion battery. Nano Energy **21**, 162–171 (2016). https://doi.org/10.1016/j.nanoen.2016.01.010
238. Chen, Y.M., Yu, L., Lou, X.W.D.: Hierarchical tubular structures composed of Co_3O_4 hollow nanoparticles and carbon nanotubes for lithium storage. Angew. Chem. Int. Ed. **55**, 5990–5993 (2016). https://doi.org/10.1002/anie.201600133
239. Li, N., Sonsg, H., Cui, H., et al.: SnO_2 nanoparticles anchored on vertically aligned graphene with a high rate, high capacity, and long life for lithium storage. Electrochim. Acta **130**, 670–678 (2014). https://doi.org/10.1016/j.electacta.2014.03.081
240. Hu, L.R., Ren, Y.M., Yang, H.X., et al.: Fabrication of 3D hierarchical MoS_2/polyaniline and MoS_2/C architectures for lithium-ion battery applications. ACS Appl. Mater. Interfaces. **6**, 14644–14652 (2014). https://doi.org/10.1021/am503995s
241. Wang, Y., Chen, B., Seo, D.H., et al.: MoS_2-coated vertical graphene nanosheet for high-performance rechargeable lithium-ion batteries and hydrogen production. NPG Asia Mater. **8**, e268 (2016). https://doi.org/10.1038/am.2016.44
242. Chen, L., Yang, W.J., Wang, J.B., et al.: Hierarchical cobalt-based metal-organic framework for high-performance lithium-ion batteries. Chem. Eur. J. **24**, 13362–13367 (2018). https://doi.org/10.1002/chem.201802629
243. Gan, Q.M., He, H.N., Zhao, K.M., et al.: Morphology-dependent electrochemical performance of Ni-1, 3, 5-benzenetricarboxylate metal-organic frameworks as an anode material for Li-ion batteries. J. Colloid Interface Sci. **530**, 127–136 (2018). https://doi.org/10.1016/j.jcis.2018.06.057
244. Wu, Z.Z., Xie, J., Xu, Z.J., et al.: Recent progress in metal–organic polymers as promising electrodes for lithium/sodium rechargeable batteries. J. Mater. Chem. A **7**, 4259–4290 (2019). https://doi.org/10.1039/c8ta11994e
245. Ning, Y.Q., Lou, X.B., Shen, M., et al.: Mesoporous cobalt 2, 5-thiophenedicarboxylic coordination polymer for high performance Na-ion batteries. Mater. Lett. **197**, 245–248 (2017). https://doi.org/10.1016/j.matlet.2017.01.126
246. Lou, X.B., Hu, X.S., Li, C., et al.: Room-temperature synthesis of a cobalt 2, 3, 5, 6-tetrafluoroterephthalic coordination polymer with enhanced capacity and cycling stability for lithium batteries. New J. Chem. **41**, 1813–1819 (2017). https://doi.org/10.1039/C6NJ03165J
247. Liang, Y., Jing, Y., Gheytani, S., et al.: Universal quinone electrodes for long cycle life aqueous rechargeable batteries. Nat. Mater. **16**, 841–848 (2017). https://doi.org/10.1038/nmat4919
248. Larcher, D., Tarascon, J.M.: Towards greener and more sustainable batteries for electrical energy storage. Nat Chem **7**, 19–29 (2015). https://doi.org/10.1038/nchem.2085
249. Peng, H.L., Yu, Q.C., Wang, S.P., et al.: Molecular design strategies for electrochemical behavior of aromatic carbonyl compounds in organic and aqueous electrolytes. Adv. Sci. **6**, 1900431 (2019). https://doi.org/10.1002/advs.201900431
250. Muench, S., Wild, A., Friebe, C., et al.: Polymer-based organic batteries. Chem. Rev. **116**, 9438–9484 (2016). https://doi.org/10.1021/acs.chemrev.6b00070
251. Lu, Y., Chen, J.: Prospects of organic electrode materials for practical lithium batteries. Nat. Rev. Chem. **4**, 127–142 (2020). https://doi.org/10.1038/s41570-020-0160-9
252. Häupler, B., Wild, A., Schubert, U.S.: Carbonyls: powerful organic materials for secondary batteries. Adv. Energy Mater. **5**, 1402034 (2015). https://doi.org/10.1002/aenm.201402034
253. Song, Z.P., Zhan, H., Zhou, Y.H.: Polyimides: promising energy-storage materials. Angew. Chem. **122**, 8622–8626 (2010). https://doi.org/10.1002/ange.201002439
254. Song, Z.P., Xu, T., Gordin, M.L., et al.: Polymer-graphene nanocomposites as ultrafast-charge and -discharge cathodes for rechargeable lithium batteries. Nano Lett. **12**, 2205–2211 (2012). https://doi.org/10.1021/nl2039666
255. Meng, Y.N., Wu, H.P., Zhang, Y.J., et al.: A flexible electrode based on a three-dimensional graphene network-supported polyimide for lithium-ion batteries. J. Mater. Chem. A **2**, 10842–10846 (2014). https://doi.org/10.1039/c4ta00364k
256. Ba, Z.H., Wang, Z.X., Luo, M., et al.: Benzoquinone-based polyimide derivatives as high-capacity and stable organic cathodes for lithium-ion batteries. ACS Appl. Mater. Interfaces. **12**, 807–817 (2020). https://doi.org/10.1021/acsami.9b18422
257. Peng, H.L., Wang, S.P., Kim, M., et al.: Highly reversible electrochemical reaction of insoluble 3D nanoporous polyquinoneimines with stable cycle and rate performance. Energy Storage Mater. **25**, 313–323 (2020). https://doi.org/10.1016/j.ensm.2019.10.007
258. Wang, F., Fan, X.L., Gao, T., et al.: High-voltage aqueous magnesium ion batteries. ACS Central Sci. **3**, 1121–1128 (2017). https://doi.org/10.1021/acscentsci.7b00361
259. Chen, L., Bao, J.L., Dong, X., et al.: Aqueous Mg-ion battery based on polyimide anode and Prussian blue cathode. ACS Energy Lett. **2**, 1115–1121 (2017). https://doi.org/10.1021/acsenergylett.7b00040
260. Zhang, G.F., Xu, Z.X., Liu, P., et al.: A facile in situ polymerization strategy towards polyimide/carbon black composites as

high performance lithium ion battery cathodes. Electrochim. Acta **260**, 598–605 (2018). https://doi.org/10.1016/j.electacta.2017.12.075
261. Wu, D.Q., Zhang, G.F., Lu, D., et al.: Perylene diimide-diamine/carbon black composites as high performance lithium/sodium ion battery cathodes. J. Mater. Chem. A **6**, 13613–13618 (2018). https://doi.org/10.1039/C8TA03186J
262. Gheytani, S., Liang, Y.L., Wu, F.L., et al.: An aqueous Ca-ion battery. Adv. Sci. **4**, 1700465 (2017). https://doi.org/10.1002/advs.201700465
263. Lu, D., Liu, H.Q., Huang, T., et al.: Magnesium ion based organic secondary batteries. J. Mater. Chem. A **6**, 17297–17302 (2018). https://doi.org/10.1039/c8ta05230a
264. Bruce, P.G., Freunberger, S.A., Hardwick, L.J., et al.: Li-O_2 and Li-S batteries with high energy storage. Nat. Mater. **11**, 19–29 (2012). https://doi.org/10.1038/nmat3191
265. Ji, X., Lee, K.T., Nazar, L.F.: A highly ordered nanostructured carbon-sulphur cathode for lithium-sulphur batteries. Nat. Mater. **8**, 500–506 (2009). https://doi.org/10.1038/nmat2460
266. Zhang, L.L., Wang, Y.J., Niu, Z.Q., et al.: Advanced nanostructured carbon-based materials for rechargeable lithium-sulfur batteries. Carbon **141**, 400–416 (2019). https://doi.org/10.1016/j.carbon.2018.09.067
267. Li, M., Zhang, Y.N., Wang, X.L., et al.: Gas Pickering emulsion templated hollow carbon for high rate performance lithium sulfur batteries. Adv. Funct. Mater. **26**, 8408–8417 (2016). https://doi.org/10.1002/adfm.201603241
268. Peng, H.J., Liang, J.Y., Zhu, L., et al.: Catalytic self-limited assembly at hard templates: a mesoscale approach to graphene nanoshells for lithium-sulfur batteries. ACS Nano **8**, 11280–11289 (2014). https://doi.org/10.1021/nn503985s
269. Moreno, N., Caballero, A., Morales, J., et al.: Lithium battery using sulfur infiltrated in three-dimensional flower-like hierarchical porous carbon electrode. Mater. Chem. Phys. **180**, 82–88 (2016). https://doi.org/10.1016/j.matchemphys.2016.05.044
270. Zheng, Z.M., Guo, H.C., Pei, F., et al.: High sulfur loading in hierarchical porous carbon rods constructed by vertically oriented porous graphene-like nanosheets for Li-S batteries. Adv. Funct. Mater. **26**, 8952–8959 (2016). https://doi.org/10.1002/adfm.201601897
271. Li, B., Li, S.M., Liu, J.H., et al.: Vertically aligned sulfur-graphene nanowalls on substrates for ultrafast lithium-sulfur batteries. Nano Lett. **15**, 3073–3079 (2015). https://doi.org/10.1021/acs.nanolett.5b00064
272. Li, G., Wang, X.L., Seo, M.H., et al.: Chemisorption of polysulfides through redox reactions with organic molecules for lithium–sulfur batteries. Nat. Commun. **9**, 705 (2018). https://doi.org/10.1038/s41467-018-03116-z
273. Wang, X.L., Li, G., Li, J.D., et al.: Structural and chemical synergistic encapsulation of polysulfides enables ultralong-life lithium–sulfur batteries. Energy Environ. Sci. **9**, 2533–2538 (2016). https://doi.org/10.1039/c6ee00194g
274. Zhang, Z., Luo, D., Li, G.R., et al.: Tantalum-based electrocatalyst for polysulfide catalysis and retention for high-performance lithium-sulfur batteries. Matter **3**, 920–934 (2020). https://doi.org/10.1016/j.matt.2020.06.002
275. Zhou, J., Liu, X., Zhou, J., et al.: Fully integrated hierarchical double-shelled Co_9S_8@CNT nanostructures with unprecedented performance for Li-S batteries. Nanoscale Horiz **4**, 182–189 (2019). https://doi.org/10.1039/c8nh00289d
276. Luo, D., Zhang, Z., Li, G.R., et al.: Revealing the rapid electrocatalytic behavior of ultrafine amorphous defective Nb_2O_{5-x} nanocluster toward superior Li-S performance. ACS Nano **14**, 4849–4860 (2020). https://doi.org/10.1021/acsnano.0c00799
277. Lin, D.C., Liu, Y.Y., Cui, Y.: Reviving the lithium metal anode for high-energy batteries. Nat. Nanotechnol. **12**, 194–206 (2017). https://doi.org/10.1038/nnano.2017.16
278. Cheng, X.B., Zhang, R., Zhao, C.Z., et al.: Toward safe lithium metal anode in rechargeable batteries: a review. Chem. Rev. **117**, 10403–10473 (2017). https://doi.org/10.1021/acs.chemrev.7b00115
279. Liu, S., Wang, A.X., Li, Q.Q., et al.: Crumpled graphene balls stabilized dendrite-free lithium metal anodes. Joule **2**, 184–193 (2018). https://doi.org/10.1016/j.joule.2017.11.004
280. Hu, Z.L., Li, Z.Z., Xia, Z., et al.: PECVD-derived graphene nanowall/lithium composite anodes towards highly stable lithium metal batteries. Energy Storage Mater. **22**, 29–39 (2019). https://doi.org/10.1016/j.ensm.2018.12.020
281. Liu, F.F., Xu, R., Hu, Z.X., et al.: Regulating lithium nucleation via CNTs modifying carbon cloth film for stable Li metal anode. Small **15**, 1803734 (2019). https://doi.org/10.1002/smll.201803734
282. An, Y.L., Tian, Y., Li, Y., et al.: Heteroatom-doped 3D porous carbon architectures for highly stable aqueous zinc metal batteries and non-aqueous lithium metal batteries. Chem. Eng. J. **400**, 125843 (2020). https://doi.org/10.1016/j.cej.2020.125843
283. Yabuuchi, N., Kubota, K., Dahbi, M., et al.: Research development on sodium-ion batteries. Chem. Rev. **114**, 11636–11682 (2014). https://doi.org/10.1021/cr500192f
284. Zhang, W., Liu, Y., Guo, Z.: Approaching high-performance potassium-ion batteries via advanced design strategies and engineering. Sci Adv **5**, eaav7412 (2019). https://doi.org/10.1126/sciadv.aav7412
285. Wang, X.L., Li, G., Hassan, F.M., et al.: Sulfur covalently bonded graphene with large capacity and high rate for high-performance sodium-ion batteries anodes. Nano Energy **15**, 746–754 (2015). https://doi.org/10.1016/j.nanoen.2015.05.038
286. Wang, K., Wang, N., He, J.J., et al.: Preparation of 3D architecture graphdiyne nanosheets for high-performance sodium-ion batteries and capacitors. ACS Appl. Mater. Interfaces. **9**, 40604–40613 (2017). https://doi.org/10.1021/acsami.7b11420
287. Qiu, W.D., Xiao, H.B., Li, Y., et al.: Nitrogen and phosphorus codoped vertical graphene/carbon cloth as a binder-free anode for flexible advanced potassium ion full batteries. Small **15**, 1901285 (2019). https://doi.org/10.1002/smll.201901285
288. Huang, H., Xu, R., Feng, Y., et al.: Sodium/potassium-ion batteries: boosting the rate capability and cycle life by combining morphology, defect and structure engineering. Adv. Mater. **32**, 1904320 (2020). https://doi.org/10.1002/adma.201904320
289. Xiong, P.X., Bai, P.X., Tu, S.B., et al.: Red phosphorus Nanoparticle@3D interconnected carbon nanosheet framework composite for potassium-ion battery anodes. Small **14**, 1802140 (2018). https://doi.org/10.1002/smll.201802140
290. Li, G., Luo, D., Wang, X.L., et al.: Enhanced reversible sodium-ion intercalation by synergistic coupling of few-layered MoS_2 and S-doped graphene. Adv. Funct. Mater. **27**, 1702562 (2017). https://doi.org/10.1002/adfm.201702562
291. Wu, X., Chen, Y.L., Xing, Z., et al.: Advanced carbon-based anodes for potassium-ion batteries. Adv. Energy Mater. **9**, 1900343 (2019). https://doi.org/10.1002/aenm.201900343
292. Zhao, Q.L., Gaddam, R.R., Dongfang, Y., et al.: Pyromellitic dianhydride-based polyimide anodes for sodium-ion batteries. Electrochim. Acta **265**, 702–708 (2018). https://doi.org/10.1016/j.electacta.2018.01.208
293. Blanc, L.E., Kundu, D.P., Nazar, L.F.: Scientific challenges for the implementation of Zn-ion batteries. Joule **4**, 771–799 (2020). https://doi.org/10.1016/j.joule.2020.03.002
294. Chao, D., Zhou, W., Xie, F., et al.: Roadmap for advanced aqueous batteries: From design of materials to applications. Sci Adv **6**, eaba4098 (2020). https://doi.org/10.1126/sciadv.aba4098

295. Fang, G.Z., Zhou, J., Pan, A.Q., et al.: Recent advances in aqueous zinc-ion batteries. ACS Energy Lett. **3**, 2480–2501 (2018). https://doi.org/10.1021/acsenergylett.8b01426
296. Cui, J., Guo, Z.W., Yi, J., et al.: Organic cathode materials for rechargeable zinc batteries: mechanisms, challenges, and perspectives. Chemsuschem **13**, 2160–2185 (2020). https://doi.org/10.1002/cssc.201903265
297. Poizot, P., Gaubicher, J., Renault, S., et al.: Opportunities and challenges for organic electrodes in electrochemical energy storage. Chem. Rev. **120**, 6490–6557 (2020). https://doi.org/10.1021/acs.chemrev.9b00482
298. Shi, H.Y., Ye, Y.J., Liu, K., et al.: A long-cycle-life self-doped polyaniline cathode for rechargeable aqueous zinc batteries. Angew. Chem. Int. Ed. **57**, 16359–16363 (2018). https://doi.org/10.1002/anie.201808886
299. Shin, J., Lee, J., Park, Y., et al.: Aqueous zinc ion batteries: focus on zinc metal anodes. Chem Sci **11**, 2028–2044 (2020). https://doi.org/10.1039/d0sc00022a
300. Wu, T.H., Zhang, Y., Althouse, Z.D., et al.: Nanoscale design of zinc anodes for high-energy aqueous rechargeable batteries. Mater. Today Nano **6**, 100032 (2019). https://doi.org/10.1016/j.mtnano.2019.100032
301. Simon, P., Gogotsi, Y.: Perspectives for electrochemical capacitors and related devices. Nat. Mater. **19**, 1151–1163 (2020). https://doi.org/10.1038/s41563-020-0747-z
302. Jiang, H., Lee, P.S., Li, C.Z.: 3D carbon based nanostructures for advanced supercapacitors. Energy Environ. Sci. **6**, 41–53 (2013). https://doi.org/10.1039/C2EE23284G
303. Zhang, J.N., Zhang, X.L., Zhou, Y.C., et al.: Nitrogen-doped hierarchical porous carbon nanowhisker ensembles on carbon nanofiber for high-performance supercapacitors. ACS Sustain. Chem. Eng. **2**, 1525–1533 (2014). https://doi.org/10.1021/sc500221s
304. Wang, S.P., Han, C.L., Wang, J., et al.: Controlled synthesis of ordered mesoporous carbohydrate-derived carbons with flower-like structure and N-doping by self-transformation. Chem. Mater. **26**, 6872–6877 (2014). https://doi.org/10.1021/cm503669v
305. Li, C.X., Li, Z.L., Cheng, Z.H., et al.: Functional carbon nanomesh clusters. Adv. Funct. Mater. **27**, 1701514 (2017). https://doi.org/10.1002/adfm.201701514
306. Liu, X.F., Mei, P., Lei, S., et al.: Scalable polymerization approach to tailoring morphologies of polyimide-derived N-doped carbons for high-performance supercapacitors. Energy Technol. **8**, 1901013 (2020). https://doi.org/10.1002/ente.201901013
307. Seo, D.H., Han, Z.J., Kumar, S., et al.: Structure-controlled, vertical graphene-based, binder-free electrodes from plasma-reformed butter enhance supercapacitor performance. Adv. Energy Mater. **3**, 1316–1323 (2013). https://doi.org/10.1002/aenm.201300431
308. Bo, Z., Zhu, W.G., Ma, W., et al.: Vertically oriented graphene bridging active-layer/current-collector interface for ultrahigh rate supercapacitors. Adv. Mater. **25**, 5799–5806 (2013). https://doi.org/10.1002/adma.201301794
309. Miller, J.R., Outlaw, R.A., Holloway, B.C.: Graphene double-layer capacitor with ac line-filtering performance. Science **329**, 1637–1639 (2010). https://doi.org/10.1126/science.1194372
310. Bo, Z., Xu, C.X., Yang, H.C., et al.: Hierarchical, vertically-oriented carbon nanowall foam supercapacitor using room temperature ionic liquid mixture for AC line filtering with ultrahigh energy density. ChemElectroChem **6**, 2167–2173 (2019). https://doi.org/10.1002/celc.201801825
311. Li, W.Y., Azam, S., Dai, G.Z., et al.: Prussian blue based vertical graphene 3D structures for high frequency electrochemical capacitors. Energy Storage Mater. **32**, 30–36 (2020). https://doi.org/10.1016/j.ensm.2020.07.016
312. Ren, G.F., Li, S.Q., Fan, Z.X., et al.: Ultrahigh-rate supercapacitors with large capacitance based on edge oriented graphene coated carbonized cellulous paper as flexible freestanding electrodes. J. Power Sources **325**, 152–160 (2016). https://doi.org/10.1016/j.jpowsour.2016.06.021
313. Xiong, G., He, P., Lyu, Z., et al.: Bioinspired leaves-on-branchlet hybrid carbon nanostructure for supercapacitors. Nat. Commun. **9**, 790 (2018). https://doi.org/10.1038/s41467-018-03112-3
314. Simon, P., Gogotsi, Y.: Materials for electrochemical capacitors. Nat. Mater. **7**, 845–854 (2008). https://doi.org/10.1038/nmat2297
315. Li, C., Bai, H., Shi, G.: Conducting polymer nanomaterials: electrosynthesis and applications. Chem. Soc. Rev. **38**, 2397–2409 (2009). https://doi.org/10.1039/b816681c
316. Han, Y.Q., Dai, L.M.: Conducting polymers for flexible supercapacitors. Macromol. Chem. Phys. **220**, 1800355 (2019). https://doi.org/10.1002/macp.201800355
317. Wang, Z.L., Guo, R., Li, G.R., et al.: Polyaniline nanotube arrays as high-performance flexible electrodes for electrochemical energy storage devices. J. Mater. Chem. **22**, 2401–2404 (2012). https://doi.org/10.1039/C2JM15070K
318. Xiong, S.X., Yang, F., Jiang, H., et al.: Covalently bonded polyaniline/fullerene hybrids with coral-like morphology for high-performance supercapacitor. Electrochim. Acta **85**, 235–242 (2012). https://doi.org/10.1016/j.electacta.2012.08.056
319. Malik, R., Zhang, L., McConnell, C., et al.: Three-dimensional, free-standing polyaniline/carbon nanotube composite-based electrode for high-performance supercapacitors. Carbon **116**, 579–590 (2017). https://doi.org/10.1016/j.carbon.2017.02.036
320. Liu, J.H., Xu, X.Y., Lu, W.B., et al.: A high performance all-solid-state flexible supercapacitor based on carbon nanotube fiber/carbon nanotubes/polyaniline with a double core-sheathed structure. Electrochim. Acta **283**, 366–373 (2018). https://doi.org/10.1016/j.electacta.2018.06.158
321. Wang, X.N., Wei, H.L., Liu, X.Z., et al.: Novel three-dimensional polyaniline nanothorns vertically grown on buckypaper as high-performance supercapacitor electrode. Nanotechnology **30**, 325401 (2019). https://doi.org/10.1088/1361-6528/ab156d
322. Xiong, G.P., Meng, C.Z., Reifenberger, R.G., et al.: Graphitic petal electrodes for all-solid-state flexible supercapacitors. Adv. Energy Mater. **4**, 1300515 (2014). https://doi.org/10.1002/aenm.201300515
323. Qu, Y., Lu, C.B., Su, Y.Z., et al.: Hierarchical-graphene-coupled polyaniline aerogels for electrochemical energy storage. Carbon **127**, 77–84 (2018). https://doi.org/10.1016/j.carbon.2017.10.088
324. Wang, Z.L., Guo, R., Ding, L.X., et al.: Controllable template-assisted electrodeposition of single-and multi-walled nanotube arrays for electrochemical energy storage. Sci Rep **3**, 1204 (2013). https://doi.org/10.1038/srep01204
325. Zhang, H., Cao, G.P., Wang, Z.Y., et al.: Growth of manganese oxide nanoflowers on vertically-aligned carbon nanotube arrays for high-rate electrochemical capacitive energy storage. Nano Lett. **8**, 2664–2668 (2008). https://doi.org/10.1021/nl800925j
326. Zhang, L., Holt, C.M.B., Luber, E.J., et al.: High rate electrochemical capacitors from three-dimensional arrays of vanadium nitride functionalized carbon nanotubes. J. Phys. Chem. C **115**, 24381–24393 (2011). https://doi.org/10.1021/jp205052f
327. Zhu, C.R., Yang, P.H., Chao, D.L., et al.: All metal nitrides solid-state asymmetric supercapacitors. Adv. Mater. **27**, 4566–4571 (2015). https://doi.org/10.1002/adma.201501838
328. Xiong, G.P., Hembram, K.P.S.S., Reifenberger, R.G., et al.: MnO_2-coated graphitic petals for supercapacitor electrodes. J. Power Sources **227**, 254–259 (2013). https://doi.org/10.1016/j.jpowsour.2012.11.040

329. Zhang, Y.Z., Cheng, T., Wang, Y., et al.: A simple approach to boost capacitance: flexible supercapacitors based on manganese Oxides@MOFs via chemically induced in situ self-transformation. Adv. Mater. **28**, 5242–5248 (2016). https://doi.org/10.1002/adma.201600319
330. Huang, J., Peng, Z.Y., Xiao, Y.B., et al.: Hierarchical nanosheets/walls structured carbon-coated porous vanadium nitride anodes enable wide-voltage-window aqueous asymmetric supercapacitors with high energy density. Adv. Sci. **6**, 1900550 (2019). https://doi.org/10.1002/advs.201900550
331. Wang, H.W., Zhu, C.R., Chao, D.L., et al.: Nonaqueous hybrid lithium-ion and sodium-ion capacitors. Adv. Mater. **29**, 1702093 (2017). https://doi.org/10.1002/adma.201702093
332. Han, X.Q., Han, P.X., Yao, J.H., et al.: Nitrogen-doped carbonized polyimide microsphere as a novel anode material for high performance lithium ion capacitors. Electrochim. Acta **196**, 603–610 (2016). https://doi.org/10.1016/j.electacta.2016.02.185
333. Jiang, J.M., Nie, P., Ding, B., et al.: Highly stable lithium ion capacitor enabled by hierarchical polyimide derived carbon microspheres combined with 3D current collectors. J. Mater. Chem. A **5**, 23283–23291 (2017). https://doi.org/10.1039/C7TA05972H
334. Jiang, J.M., Zhang, Y.D., An, Y.F., et al.: Engineering ultrathin MoS_2 nanosheets anchored on N-doped carbon microspheres with pseudocapacitive properties for high-performance lithium-ion capacitors. Small Methods **3**, 1900081 (2019). https://doi.org/10.1002/smtd.201900081
335. Zhang, Y.D., Nie, P., Xu, C.Y., et al.: High energy aqueous sodium-ion capacitor enabled by polyimide electrode and high-concentrated electrolyte. Electrochim. Acta **268**, 512–519 (2018). https://doi.org/10.1016/j.electacta.2018.02.125
336. Zhao, Q.L., Dongfang, Y., Whittaker, A.K., et al.: A hybrid sodium-ion capacitor with polyimide as anode and polyimide-derived carbon as cathode. J. Power Sources **396**, 12–18 (2018). https://doi.org/10.1016/j.jpowsour.2018.06.010
337. Zhao, Q.L., Dongfang, Y., Zhang, C., et al.: Tailored polyimide-graphene nanocomposite as negative electrode and reduced graphene oxide as positive electrode for flexible hybrid sodium-ion capacitors. ACS Appl. Mater. Interfaces. **10**, 43730–43739 (2018). https://doi.org/10.1021/acsami.8b17171
338. Liu, M.Q., Chang, L.M., Wang, J., et al.: Hierarchical N-doped carbon nanosheets submicrospheres enable superior electrochemical properties for potassium ion capacitors. J. Power Sources **469**, 228415 (2020). https://doi.org/10.1016/j.jpowsour.2020.228415
339. Xu, D.M., Chao, D.L., Wang, H.W., et al.: Flexible quasi-solid-state sodium-ion capacitors developed using 2D metal-organic-framework array as reactor. Adv. Energy Mater. **8**, 1702769 (2018). https://doi.org/10.1002/aenm.201702769
340. Beidaghi, M., Gogotsi, Y.: Capacitive energy storage in micro-scale devices: recent advances in design and fabrication of micro-supercapacitors. Energy Environ. Sci. **7**, 867–884 (2014). https://doi.org/10.1039/C3EE43526A
341. Zhang, P., Wang, F., Yu, M., et al.: Two-dimensional materials for miniaturized energy storage devices: from individual devices to smart integrated systems. Chem. Soc. Rev. **47**, 7426–7451 (2018). https://doi.org/10.1039/c8cs00561c
342. Wang, X.F., Jiang, K., Shen, G.Z.: Flexible fiber energy storage and integrated devices: recent progress and perspectives. Mater. Today **18**, 265–272 (2015). https://doi.org/10.1016/j.mattod.2015.01.002
343. Xiong, G.P., He, P.G., Huang, B.Y., et al.: Graphene nanopetal wire supercapacitors with high energy density and thermal durability. Nano Energy **38**, 127–136 (2017). https://doi.org/10.1016/j.nanoen.2017.05.050
344. He, Y.H., Tan, Q., Lu, L.L., et al.: Metal-nitrogen-carbon catalysts for oxygen reduction in PEM fuel cells: self-template synthesis approach to enhancing catalytic activity and stability. Electrochem. Energy Rev. **2**, 231–251 (2019). https://doi.org/10.1007/s41918-019-00031-9
345. Li, Y.H., Li, Q.Y., Wang, H.Q., et al.: Recent progresses in oxygen reduction reaction electrocatalysts for electrochemical energy applications. Electrochem. Energy Rev. **2**, 518–538 (2019). https://doi.org/10.1007/s41918-019-00052-4
346. Paul, R., Dai, Q.B., Hu, C.G., et al.: Ten years of carbon-based metal-free electrocatalysts. Carbon Energy **1**, 19–31 (2019). https://doi.org/10.1002/cey2.5
347. Guo, Q.H., Zhao, D., Liu, S.W., et al.: Free-standing nitrogen-doped carbon nanotubes at electrospun carbon nanofibers composite as an efficient electrocatalyst for oxygen reduction. Electrochim. Acta **138**, 318–324 (2014). https://doi.org/10.1016/j.electacta.2014.06.120
348. She, X., Yang, D., Jing, D., et al.: Nitrogen-doped one-dimensional (1D) macroporous carbonaceous nanotube arrays and their application in electrocatalytic oxygen reduction reactions. Nanoscale **6**, 11057–11061 (2014). https://doi.org/10.1039/c4nr03340j
349. Yu, D.S., Xue, Y.H., Dai, L.M.: Vertically aligned carbon nanotube arrays Co-doped with phosphorus and nitrogen as efficient metal-free electrocatalysts for oxygen reduction. J. Phys. Chem. Lett. **3**, 2863–2870 (2012). https://doi.org/10.1021/jz3011833
350. Zhu, J.L., Jiang, S.P., Wang, R.H., et al.: One-pot synthesis of a nitrogen and phosphorus-dual-doped carbon nanotube array as a highly effective electrocatalyst for the oxygen reduction reaction. J. Mater. Chem. A **2**, 15448–15453 (2014). https://doi.org/10.1039/c4ta02427c
351. Li, H.B., Kang, W.J., Wang, L., et al.: Synthesis of three-dimensional flowerlike nitrogen-doped carbons by a copyrolysis route and the effect of nitrogen species on the electrocatalytic activity in oxygen reduction reaction. Carbon **54**, 249–257 (2013). https://doi.org/10.1016/j.carbon.2012.11.036
352. Guo, D., Wei, H., Chen, X., et al.: 3D hierarchical nitrogen-doped carbon nanoflower derived from chitosan for efficient electrocatalytic oxygen reduction and high performance lithium-sulfur batteries. J. Mater. Chem. A **5**, 18193–18206 (2017). https://doi.org/10.1039/C7TA04728B
353. Zhang, S.H., Xia, W., Yang, Q., et al.: Core-shell motif construction: highly graphitic nitrogen-doped porous carbon electrocatalysts using MOF-derived carbon@COF heterostructures as sacrificial templates. Chem. Eng. J. **396**, 125154 (2020). https://doi.org/10.1016/j.cej.2020.125154
354. Chen, L., Xu, Z.X., Han, W.J., et al.: Bimetallic CoNi alloy nanoparticles embedded in pomegranate-like nitrogen-doped carbon spheres for electrocatalytic oxygen reduction and evolution. ACS Appl. Nano Mater. **3**, 1354–1362 (2020). https://doi.org/10.1021/acsanm.9b02201
355. Li, G., Wang, X.L., Fu, J., et al.: Pomegranate-inspired design of highly active and durable bifunctional electrocatalysts for rechargeable metal-air batteries. Angew. Chem. Int. Ed. **55**, 4977–4982 (2016). https://doi.org/10.1002/anie.201600750
356. Wang, X.Q., Li, Z.J., Qu, Y.T., et al.: Review of metal catalysts for oxygen reduction reaction: from nanoscale engineering to atomic design. Chem **5**, 1486–1511 (2019). https://doi.org/10.1016/j.chempr.2019.03.002
357. Wang, Y.J., Fang, B.Z., Zhang, D., et al.: A review of carbon-composited materials as air-electrode bifunctional electrocatalysts for metal-air batteries. Electrochem. Energy Rev. **1**, 1–34 (2018). https://doi.org/10.1007/s41918-018-0002-3
358. Seo, M.H., Park, M.G., Lee, D.U., et al.: Bifunctionally active and durable hierarchically porous transition metal-based hybrid

electrocatalyst for rechargeable metal-air batteries. Appl. Catal. B: Environ. **239**, 677–687 (2018). https://doi.org/10.1016/j.apcatb.2018.06.006
359. Liu, G.H., Li, J.D., Fu, J., et al.: An oxygen-vacancy-rich semiconductor-supported bifunctional catalyst for efficient and stable zinc-air batteries. Adv. Mater. **31**, 1806761 (2019). https://doi.org/10.1002/adma.201806761
360. Hou, C.C., Zou, L.L., Xu, Q.: A hydrangea-like superstructure of open carbon cages with hierarchical porosity and highly active metal sites. Adv. Mater. **31**, 1904689 (2019). https://doi.org/10.1002/adma.201904689
361. Zhou, J., Dou, Y.B., Zhou, A., et al.: Layered metal-organic framework-derived metal oxide/carbon nanosheet arrays for catalyzing the oxygen evolution reaction. ACS Energy Lett. **3**, 1655–1661 (2018). https://doi.org/10.1021/acsenergylett.8b00809
362. Yang, Y., Zhang, H.L., Lin, Z.H., et al.: A hybrid energy cell for self-powered water splitting. Energy Environ. Sci. **6**, 2429–2434 (2013). https://doi.org/10.1039/c3ee41485j
363. Jia, J., Seitz, L.C., Benck, J.D., et al.: Solar water splitting by photovoltaic-electrolysis with a solar-to-hydrogen efficiency over 30. Nat. Commun. **7**, 13237 (2016). https://doi.org/10.1038/ncomms13237
364. Li, G., Wang, X.L., Seo, M.H., et al.: Design of ultralong single-crystal nanowire-based bifunctional electrodes for efficient oxygen and hydrogen evolution in a mild alkaline electrolyte. J. Mater. Chem. A **5**, 10895–10901 (2017). https://doi.org/10.1039/c7ta02745a
365. Sun, H.M., Yan, Z.H., Liu, F.M., et al.: Self-supported transition-metal-based electrocatalysts for hydrogen and oxygen evolution. Adv. Mater. **32**, 1806326 (2020). https://doi.org/10.1002/adma.201806326
366. Lu, J.J., Yin, S.B., Shen, P.K.: Carbon-encapsulated electrocatalysts for the hydrogen evolution reaction. Electrochem. Energy Rev. **2**, 105–127 (2019). https://doi.org/10.1007/s41918-018-0025-9
367. Zhuang, Z.C., Huang, J.Z., Li, Y., et al.: The holy grail in platinum-free electrocatalytic hydrogen evolution: molybdenum-based catalysts and recent advances. ChemElectroChem **6**, 3570–3589 (2019). https://doi.org/10.1002/celc.201900143
368. Smith, A.J., Chang, Y.H., Raidongia, K., et al.: Molybdenum sulfide supported on crumpled graphene balls for electrocatalytic hydrogen production. Adv. Energy Mater. **4**, 1400398 (2014). https://doi.org/10.1002/aenm.201400398
369. Xu, Z.X., Zhang, G.F., Lu, C.B., et al.: Molybdenum carbide nanoparticle decorated hierarchical tubular carbon superstructures with vertical nanosheet arrays for efficient hydrogen evolution. J. Mater. Chem. A **6**, 18833–18838 (2018). https://doi.org/10.1039/C8TA06278A
370. Fan, X.J., Zhou, H.Q., Guo, X.: WC nanocrystals grown on vertically aligned carbon nanotubes: an efficient and stable electrocatalyst for hydrogen evolution reaction. ACS Nano **9**, 5125–5134 (2015). https://doi.org/10.1021/acsnano.5b00425
371. Fan, X.J., Peng, Z.W., Ye, R.Q., et al.: M_3C (M: fe, co, Ni) nanocrystals encased in graphene nanoribbons: An active and stable bifunctional electrocatalyst for oxygen reduction and hydrogen evolution reactions. ACS Nano **9**, 7407–7418 (2015). https://doi.org/10.1021/acsnano.5b02420
372. Yan, H.J., Xie, Y., Wu, A.P., et al.: Anion-modulated HER and OER activities of 3D Ni-V-based interstitial compound heterojunctions for high-efficiency and stable overall water splitting. Adv. Mater. **31**, 1901174 (2019). https://doi.org/10.1002/adma.201901174
373. Manjunatha, R., Karajić, A., Liu, M.M., et al.: A review of composite/hybrid electrocatalysts and photocatalysts for nitrogen reduction reactions: advanced materials, mechanisms, challenges and perspectives. Electrochem. Energy Rev. **3**, 506–540 (2020). https://doi.org/10.1007/s41918-020-00069-0
374. Guo, C.X., Ran, J.R., Vasileff, A., et al.: Rational design of electrocatalysts and photo(electro)catalysts for nitrogen reduction to ammonia (NH_3) under ambient conditions. Energy Environ. Sci. **11**, 45–56 (2018). https://doi.org/10.1039/C7EE02220D
375. Lin, Y.X., Zhang, S.N., Xue, Z.H., et al.: Boosting selective nitrogen reduction to ammonia on electron-deficient copper nanoparticles. Nat. Commun. **10**, 4380 (2019). https://doi.org/10.1038/s41467-019-12312-4
376. Hisatomi, T., Kubota, J., Domen, K.: Recent advances in semiconductors for photocatalytic and photoelectrochemical water splitting. Chem. Soc. Rev. **43**, 7520–7535 (2014). https://doi.org/10.1039/c3cs60378d
377. Moon, J., Sim, U., Kim, D.J., et al.: Hierarchical carbon-silicon nanowire heterostructures for the hydrogen evolution reaction. Nanoscale **10**, 13936–13941 (2018). https://doi.org/10.1039/c8nr02262c
378. Carraro, F., Calvillo, L., Cattelan, M., et al.: Fast one-pot synthesis of MoS_2/crumpled graphene p-n nanonjunctions for enhanced photoelectrochemical hydrogen production. ACS Appl. Mater. Interfaces. **7**, 25685–25692 (2015). https://doi.org/10.1021/acsami.5b06668
379. Han, Y.Y., Lu, X.L., Tang, S.F., et al.: Metal-free 2D/2D heterojunction of graphitic carbon nitride/graphdiyne for improving the hole mobility of graphitic carbon nitride. Adv. Energy Mater. **8**, 1702992 (2018). https://doi.org/10.1002/aenm.201702992
380. Gao, H.H., Cao, R.Y., Zhang, S.W., et al.: Three-dimensional hierarchical g-C3N4 architectures assembled by ultrathin self-doped nanosheets: extremely facile hexamethylenetetramine activation and superior photocatalytic hydrogen evolution. ACS Appl. Mater. Interfaces. **11**, 2050–2059 (2019). https://doi.org/10.1021/acsami.8b17757

Zhixiao Xu is currently a Ph.D. student at the University of Alberta under the supervision of Dr. Xiaolei Wang. He received his B.S. from Beijing University of Chemical Technology (2013) and M.Sc. from Shanghai Jiao Tong University (2016). His current research mainly involves the design of new energy materials and development of novel battery technologies beyond lithium-ion batteries.

Wenjing Deng is pursuing her Ph.D. at the University of Alberta under the supervision of Dr. Xiaolei Wang. She obtained her B.S. (2017) and M.Sc. (2019) from Beijing University of Chemical Technology and Case Western Reserve University through a 3 + 2 undergraduate-graduate joint program. She is now working on the development of high-performance lithium-sulfur batteries.

Dr. Xiaolei Wang is a tenure-track assistant professor at the University of Alberta (UofA) and runs his *Nano For Advanced Clean Energy* (NanoFACE) laboratory in the Department of Chemical and Materials Engineering. Before joining UofA, he worked as tenure-track assistant professor at Concordia University from 2017 to 2019, and postdoctoral fellow researcher at the University of Waterloo from 2014 to 2017. Dr. Wang received his Ph.D. in Chemical and Biomolecular Engineering at the University of California, Los Angeles (UCLA, 2013), M.Sc. in Chemical Engineering at Tianjin University (TJU, 2007), and B.Sc. in Polymer Chemical Engineering at Dalian University of Technology (DUT, 2004). His research mainly focuses on the rational design, development and application of novel nanostructured materials for energy-related technologies including lithium-ion batteries, sodium-ion batteries, lithium–sulfur (Li–S) batteries, metal-air batteries, supercapacitors, and electrocatalytic systems.